APPROVAL SHEET

Title of Dissertation: Stability and accessibility of Turing rolls, soliton crystals, and single solitons in microresonators

Name of Candidate: Zhen Qi
Doctor of Philosophy, 2022

Dissertation and Abstract Approved: 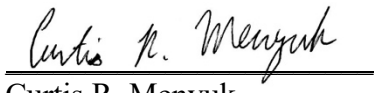

Curtis R. Menyuk
Professor
Department of Computer Science and Electrical Engineering

Date Approved: 10/24/2022

ZHEN QI

EDUCATION

PhD University of Maryland Baltimore County, Electrical Engineering December 2022

PhD Nanjing University, Condensed Matter Physics November 2011

BS Sichuan University, Microelectronics June 2004

HONORS AND AWARDS

Title of Award

Nanjing University Outstanding Graduate Student 2009

Title of Grant

UMBC GSA Travel Grant 2022
2022 SIAM International Conference on Data Mining (SDM'22) Travel Award 2022
IEEE Big Data Conference Student Travel Award 2022
UMBC GSA Travel Grant 2019
APS-DLS Student Travel Grant for CLEO 2018
UMBC GSA Travel Grant 2018
UMBC GSA Travel Grant 2017
UMBC GSA Travel Grant 2016

RESEARCH BACKGROUND

Physics:

Nonlinear Optics, Lasers, Solitons, Waveguides, Nonlinear Photonic Crystals, Quasiperiodic Structures, Frequency Combs in Optics and Acoustics, Phonon Polaritons, Thermodynamics, Liquid Crystal Display, Quantum Optics, Metamaterials, Photodetectors, Noise

Mathematics:

Nonlinear Dynamics, Stability Analysis, Perturbation Theory, Nonlinear Partial Differential Equations, Stochastic Differential Equations, Boundary Value Problems, Computational Algorithms (including Beam Propagation Method, Newton's Method, Spectral Method, Transfer Matrix Method, Multiply Scale Analysis, Finite Element Method, Finite Difference Time Domain Method), Parallel Computing, Machine Learning,

RESEARCH EXPERIENCE

Stability and Accessibility of Turing Rolls, Soliton Crystals and Single Solitons in Microresonators

University of Maryland Baltimore County 2013-
Advisor: Curtis Menyuk

- Theoretically and numerically studied cnoidal waves and their corresponding frequency combs in microring resonators with anomalous group velocity dispersion [J. Opt. Soc. Am. B, vol. 34, no. 4, pp. 785-794, (2017)]
- Theoretically and numerically studied cnoidal waves and their corresponding frequency combs in microring resonators with normal group velocity dispersion [Frontiers in Optics (FiO), Sep. 18-21, 2017, JTu3A.14]
- Theoretically and numerically studied the stability of solitons and soliton crystals in microring resonators, and obtained the stability chart in the parameter space [**Optica, vol. 6, no. 9, pp. 1220-1232, (2019)**, Optics Letters, vol. 44, no. 12, pp. 3078-3081, (2019)]
- Theoretically and numerically studied the stability and accessibility of solitons and soliton crystals in microring resonators with thermal effects [Opt. Express, vol. 28, no. 24, pp. 36304-36315, (2020), Phys. Rev. A, vol. 103, no. 1, pp. 013512, (2021)]
- Theoretically and numerically studied solitons and solitons crystals in coupled microring resonators [Frontiers in Optics (FiO), Sep. 15-19, 2019, JTu4A.118]
- Theoretically and numerically studied phononic frequency combs in resonators [Appl. Phys. Lett., vol. 117, no. 18, pp. 183503, (2020)]
- Theoretically and numerically studied two-color solitons and solitons crystals in microring resonators in second order generation
- Theoretically and numerically studied solitons and solitons crystals in microring resonators with avoided crossings [Conference on Lasers and Electro-Optics (CLEO), May. 15-20, 2022]

Quadratic Nonlinear and Electromagnetic Coupling Effects in Dielectric Microstructure

Nanjing University 2004-2011

Advisor: Shi-Ning Zhu

- Theoretically interpreted the phenomenon observed in the experiment of Cherenkov phase-matched second order generation and sum-frequency generation in two-dimensional nonlinear photonic crystal waveguides [Appl. Phys. Lett., vol. 89, no. 17, pp. 171113, (2006), **Phys. Rev. Lett., vol. 100, no. 16, pp. 163904, (2008)**]
- Numerically studied the high-confined second harmonic generation in nano-scale slot waveguides [J. Phys. D, vol. 41, no. 2, pp. 025109, (2008)]
- Theoretically studied phonon polaritons in nonaxial aligned piezoelectric superlattices [J. Appl. Phys., vol. 105, no. 7, pp. 074102, (2009)]
- Theoretically designed two-dimensional quasi-periodic nonlinear photonic crystals and observed the cascaded χ^2 third order generation in the experiment [J. Opt. Soc. Am. B, vol. 28, no. 4, pp. 608-612, (2011)]
- Theoretically and numerically studied the three-color solitons in cascaded χ^2 third order generation in one-dimensional quasi-periodic nonlinear photonic crystals [arXiv:1803.08543]

Achromatic Waveplates for Liquid Crystal Displays

University of California at Santa Barbara 2008-2010

- Theoretically designed achromatic waveplates for liquid crystal displays [J. Display Technol., vol. 9, no. 7, pp. 586-591, (2013)]

TEACHING EXPERIENCE

Nanjing University Sep 2004 to June 2005
Teaching Assistant, Physics Department

University of Maryland Baltimore County Sep 2013 to May 2015
Teaching Assistant, Department of Computer Science and Electrical Engineering

PUBLICATIONS

Journal Publications

Amir Leshem, Zhen Qi, Thomas F. Carruthers, Curtis R. Menyuk, and Omri Gat, "Thermal instabilities, frequency-comb formation, and temporal oscillations in Kerr microresonators," Physical Review A, vol. 103, no. 1, pp. 013512, (2021).

Zhen Qi, Amir Leshem, Jose A. Jaramillo-Villegas, Giuseppe D'Aguanno, Thomas F. Carruthers, Omri Gat, Andrew M. Weiner, and Curtis R. Menyuk, "Deterministic access of broadband frequency combs in microresonators using cnoidal waves in the soliton crystal limit," Optics Express, vol. 28, no. 24, pp. 36304-36315, (2020).

Zhen Qi, Curtis R. Menyuk, Jason J. Gorman, and Adarsh Ganesan, "Existence conditions for phononic frequency combs," Applied Physics Letters, vol. 117, no. 18, pp. 183503, (2020).

Zhen Qi, Shaokang Wang, José Jaramillo-Villegas, Minghao Qi, Andrew M. Weiner, Giuseppe D'Aguanno, Thomas F. Carruthers, and Curtis R. Menyuk, "Dissipative cnoidal waves (Turing rolls) and the soliton limit in microring resonators," Optica, vol. 6, no. 9, pp. 1220-1232, (2019).

Aurélien Coillet, Zhen Qi, Irina V. Balakireva, Guoping Lin, Curtis R. Menyuk, and Yanne K. Chembo, "On the transition to secondary Kerr combs in whispering-gallery mode resonators," Optics Letters, vol. 44, no. 12, pp. 3078-3081, (2019).

Zhen Qi, Giuseppe D'Aguanno, and Curtis R. Menyuk, "Nonlinear frequency combs generated by cnoidal waves in microring resonators," Journal of the Optical Society of America B, vol. 34, no. 4, pp. 785-794, (2017).

Zhen Qi, Pochi Yeh, Shi-Ning Zhu, and Yong-Yuan Zhu, "Achromatic waveplates for liquid crystal displays," Journal of Display Technology, vol. 9, no. 7, pp. 586-591, (2013).

Lina Zhao, Zhen Qi, Ye Yuan, Jun Lu, Yanhua Liu, Changdong Chen, Xinjie Lv, Zhenda Xie, Xiaopeng Hu, Gang Zhao, Ping Xu, and Shining Zhu, "Integrated noncollinear red–green–blue laser light source using a two-dimensional nonlinear

photonic quasicrystal," Journal of the Optical Society of America B, vol. 28, no. 4, pp. 608-612, (2011).

Zhen Qi, Zhi-Qiang Shen, Cheng-Ping Huang, Shi-Ning Zhu, and Yong-Yuan Zhu, "Phonon polaritons in a nonaxial aligned piezoelectric superlattice," Journal of Applied Physics, vol. 105, no. 7, pp. 074102, (2009).

Yong Zhang, Zhi-Da Gao, Zhen Qi, Shi-Ning Zhu, and Nai-Ben Ming, "Nonlinear Čerenkov radiation in nonlinear photonic crystal waveguides," Physical Review Letters, vol. 100, no. 16, pp. 163904, (2008).

Zhen Qi, Tao Li, and Shi-Ning Zhu, "High-confined second harmonic generation in nano-scale slot waveguides," Journal of Physics D, vol. 41, no. 2, pp. 025109, (2008).

Yong Zhang, Zhen Qi, Wen Wang, and Shi-Ning Zhu, "Quasi-phase-matched Čerenkov second-harmonic generation in a hexagonally poled $LiTaO_3$ waveguide," Applied Physics Letters, vol. 89, no. 17, pp. 171113, (2006).

Conference Papers

Zhen Qi, Giuseppe D'Aguanno, Thomas F. Carruthers, Omri Gat, and Curtis R. Menyuk, "Stability and deterministic generation of single solitons and soliton crystals in microresonators with avoided crossings," Conference on Lasers and Electro-Optics (CLEO), May. 15-20, 2022, JW3A.47.

Curtis R. Menyuk, Logan Courtright, Zhen Qi, Shaokang Wang, and Thomas Carruthers "Dynamical methods for studying stability and noise in frequency comb sources," The 43th Progress in Electromagnetics Research Symposium (PIERS) in Hangzhou, Apr. 25-29, 2022, Session SC3, 09:30 Wed.

Curtis R. Menyuk, Brandon Wilson, Logan Courtright, Zhen Qi, Shaokang Wang, and Thomas Carruthers, "Dynamical methods for studying stability and noise in frequency comb sources," SIAM Conference on Applications of Dynamical Systems (DS21), May 23-27, 2021, MS15, 09:55 Wed.

Logan Courtright, Zhen Qi, Thomas F. Carruthers, and Curtis R. Menyuk, "Automatically mapping the stable regions of frequency combs in microresonators," Conference on Lasers and Electro-Optics (CLEO), May 9-14, 2021, JTu3A.95.

Logan Courtright, Zhen Qi, and Curtis R. Menyuk, "Plotting the stability boundary of Cnoidal waves in microresonators," Frontiers in Optics (FiO), Sep. 14-17, 2020, JM6B.31.

Zhen Qi, José Jaramillo-Villegas, Giuseppe D'Aguanno, Thomas F. Carruthers, Omri Gat, Andrew M. Weiner, and Curtis R. Menyuk, "A deterministic method for

obtaining large-bandwidth frequency combs in microresonators with thermal effects," Conference on Lasers and Electro-Optics (CLEO), May 10-15, 2020, SW4J.5.

Zhen Qi, and Curtis R. Menyuk, "Soliton frequency combs in dual microresonators," Frontiers in Optics (FiO), Sep. 15-19, 2019, JTu4A.118.

Zhen Qi, Shaokang Wang, Jose A. Jaramillo-Villegas, Minghao Qi, Andrew M. Weiner, Giuseppe D'Aguanno, and Curtis R. Menyuk, "Stability of cnoidal wave frequency combs in microresonators," Conference on Lasers and Electro-Optics (CLEO), May 13-18, 2018, SF2A.6.

Curtis R. Menyuk, Zhen Qi, and Shaokang Wang, "Instability and noise in nonlinear optical waveguides," The 39th Progress in Electromagnetics Research Symposium (PIERS) in Singapore, Nov. 19-22, 2017, Session 2P5a, 14:50 Tue.

Zhen Qi, Giuseppe D'Aguanno, and Curtis R. Menyuk, "Dark solitons and cnoidal waves in microresonators with normal dispersion," Frontiers in Optics (FiO), Sep. 18-21, 2017, JTu3A.14.

Zhen Qi, and Curtis R. Menyuk, "Cnoidal wave solutions to the Lugiato-Lefever equations with applications to microresonators," The 10th IMACS International Conference on Nonlinear Evolution Equations and Wave Phenomena, Mar. 29-Apr. 1, 2017, Session 18, 14:30 Thu.

Zhen Qi, Giuseppe D'Aguanno, and Curtis R. Menyuk, "The Lugiato-Lefever equation and cnoidal waves in microresonators," SIAM Conference on Nonlinear Waves and Coherent Structures, Aug. 8-11, 2016, MS38, 16:30 Wed.

Zhen Qi, Giuseppe D'Aguanno, and Curtis R. Menyuk, "Cnoidal waves in microresonators," Conference on Lasers and Electro-Optics (CLEO), Jun. 5-10, 2016, FM2A.7.

Shi-Ning Zhu, Yong Zhang, Zhong Yan, Zhen Qi, and Gang Zhao, "Nonlinear Čerenkov radiation in a two-dimensional nonlinear photonic crystal waveguide," 2008 APS March Meeting, Mar. 10-14, 2008, Session H35, 10:36 Tue.

Shi-Ning Zhu, Yong Zhang, Zhen Qi, Gang Zhao, Wen Wang, "Quasi-phase-matched Čerenkov radiation generation in a two-dimensional nonlinear photonic crystal waveguide," 2007 APS March Meeting, Mar. 5-9, 2007, Session S43, 14:42 Wed.

PATENTS

Zhen Qi, Giuseppe D'Aguanno, Thomas Carruthers, Omri Gat, Curtis R. Menyuk, "Deterministic access of broadband frequency combs in microresonators using cnoidal waves," (submitted to USPTO 2019).

PRESENTATIONS

Conference Oral Presentation

"A deterministic method for obtaining large-bandwidth frequency combs in microresonators with thermal effects," Conference on Lasers and Electro-Optics (CLEO), May 13, 2020.

"Stability of cnoidal wave frequency combs in microresonators," Conference on Lasers and Electro-Optics (CLEO), May 18, 2018.

"Cnoidal wave solutions to the Lugiato-Lefever equations with applications to microresonators," The 10th IMACS International Conference on Nonlinear Evolution Equations and Wave Phenomena, Mar. 30, 2017.

"The Lugiato-Lefever equation and cnoidal waves in microresonators," SIAM Conference on Nonlinear Waves and Coherent Structures, Aug. 10, 2016.

"Cnoidal waves in microresonators," Conference on Lasers and Electro-Optics (CLEO), Jun. 8, 2016.

PROFESSIONAL SERVICE

Peer-Reviewed Articles for:

- Photonics Research
- Optics Letters
- Optics Express
- Physical Review A
- Journal of the Optical Society of America B
- Optics Communications
- Microsystem Technologies
- International Conference on Computational Science (ICCS) 2022

COMPUTER SKILLS

MATLAB, Mathematica, COMSOL, FORTRAN, LaTeX, Office, basic knowledge of C and Python

ABSTRACT

Title of Document:	STABILITY AND ACCESSIBILITY OF TURING ROLLS, SOLITON CRYSTALS, AND SINGLE SOLITONS IN MICRORESONATORS
	Zhen Qi, Doctor of Philosophy, 2022
Directed By:	Professor Curtis R. Menyuk Department of Computer Science and Electrical Engineering

Broadband optical frequency combs generated in externally pumped, high-quality (Q) microresonators with the Kerr nonlinearity have important applications to metrology, high-resolution spectroscopy, and microwave photonics. In the time domain these frequency combs correspond to cnoidal waves, which are spatially and temporally stable periodic structures azimuthally propagating in the microresonator. Turing rolls, perfect solitons crystals, and single solitons in microresonators are all special cases of cnoidal waves. The types of cnoidal waves depend on experimental parameters, and each type has its own properties and applications. Determining the stability and accessibility of different types of cnoidal waves is the object of our dissertation research.

In Chapter 1, we briefly introduce frequency combs and cnoidal waves. We mathematically represent the system using the Lugiato-Lefever equation (LLE) with two different normalizations. In Chapter 2, we analytically and numerically study the family of cnoidal wave solutions to the LLE normalized with respect to the frequency detuning. In the lossless case, we analytically obtain cnoidal wave solutions, and we then extend the

solutions numerically to the case with loss. In Chapter 3, we investigate the stability and accessibility of cnoidal waves that correspond to Turing rolls or soliton crystals in microresonators. We apply highly-efficient dynamical methods to comprehensively explore the three-dimensional parameter space consisting of detuning, pump amplitude, and mode circumference to determine where stable solutions exist. In Chapter 4, we extend our previous study to consider thermal effects, which are present in real devices. Finally, in Chapter 5, we study the stability and accessibility of cnoidal waves in microresonators with avoided crossings. We find that deterministic generation of solitons is correlated with an enhanced region of stability for the single soliton. Varying both the offset and strength of an avoided crossing, we did not find simple rules that characterize when a single soliton can be deterministically accessed. However, we anticipate that our results are an important first step towards finding them.

STABILITY AND ACCESSIBILITY OF TURING ROLLS, SOLITON CRYSTALS, AND SINGLE SOLITONS IN MICRORESONATORS

By

Zhen Qi

Dissertation submitted to the Faculty of the Graduate School of the
University of Maryland, Baltimore County, in partial fulfillment
of the requirements for the degree of
Doctor of Philosophy
2022

Acknowledgments

I would like to sincerely thank my advisor Professor Curtis Menyuk for giving me this amazing opportunity to work in a variety of interesting projects during this PhD research. Professor Menyuk has always been supportive, inspiring, and encouraging during my studies.

I would also like to sincerely thank Dr. Giuseppe D'Aguanno for helping me during my PhD studies—both while a post-doctoral Research Associate at UMBC and later. I would also like to thank Dr. Thomas Carruthers for reviewing and modifying my papers and this dissertation.

Additionally, I wish to sincerely thank Dr. Matthias Gobbert and the UMBC high performance computing facility (HPCF) team for providing the high performance computing facility, which made possible my computational studies.

I would like to sincerely thank all the other members of my PhD defense committee, Dr. Li Yan, Dr. Gary Carter, and Dr. Yanhua Shih.

I would like to sincerely thank the UMBC Department of Computer Science and Electrical Engineering staff for all the help that they provided.

I would also like to thank my colleagues for helpful discussions and suggestions during my studies. Finally, I would like to thank all my friends for their support during my time at UMBC.

Finally, I would like to express my deep appreciation for my parents, my wife, and my family. I am grateful for the life that we have had together in the past and that we will have together in the future.

Contents

1 Introduction

1.1 Optical frequency combs in Microresonators

Octave-spanning (broadband) frequency combs that are generated in externally pumped, high-quality (high-Q) microresonators with a Kerr nonlinearity have important potential applications to metrology, high-resolution spectroscopy, and microwave photonics [1–7]. In Fig. 1, we show a schematic picture of a microresonator for generating frequency combs. The high-Q microresonator is pumped by a continuous-wave laser with a single frequency. Due to the effect of four-wave mixing (FWM), sideband frequency lines are generated on both side of the pump frequency. The newly-generated sideband lines will then generate additional sideband lines. Cascading of these processes will ultimately lead to a series of equally-spaced frequency lines

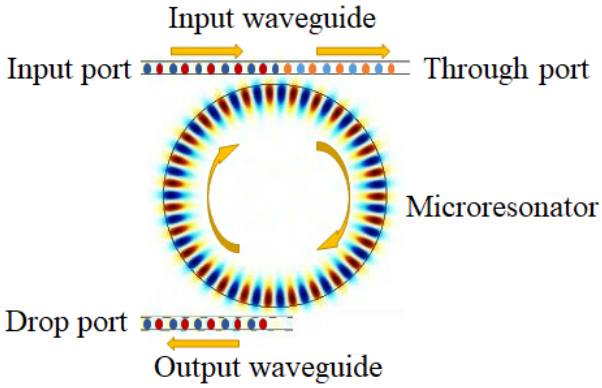

Figure 1: Schematic illustration of a microresonator configuration for generating frequency combs. The amplitude oscillations of the light in the input waveguide, microresonator, and output waveguide are indicated schematically with alternating red and blue colors. When the period of the light in the input waveguide closely matches the period of a microresonator mode, part of the energy couples into the microresonator and generates a frequency comb, while another part of the energy continues to propagate to the through port. Some of the microresonator energy couples to a drop port if it is present. The frequency comb can be observed in both the through port and the drop port if a drop port is present.

inside the microresonator. This set of frequency lines is what is referred to as an optical frequency comb. Inside the microresonator, the frequency comb corresponds to a spatially-periodic waveform that moves azimuthally at the waveform's central group velocity. The spatially periodic waveform inside the microresonator generates a temporally-periodic waveform in the output port of the optical waveguide and in the drop port if it exists. This periodic waveform in the time domain corresponds to an output frequency comb. In practice, frequency comb generation is not simple and is usually a complex process. That is especially the case for frequency combs that are generated by single solitons in the microresonator. Hence, it is important to study the stability and accessibility of periodic waveforms in microresonators.

1.2 Cnoidal waves

The family of waveforms that includes Turing rolls, perfect soliton crystals, and single solitons are special cases of cnoidal waves. In their original mathematical formulation, cnoidal waves are periodic solutions of integrable equations like the nonlinear Schrödinger equations that can be solved using the inverse scattering transformation [8], just like solitons in their original formulation are pulsed solutions of integrable equations [8]. The soliton concept has been extended to any pulsed solution of the nonlinear equations that describe pulsed solutions in modelocked lasers or resonators, in which case the pulsed solutions are often referred to as "dissipative solitons" [9].

The nonlinear Schrödinger equation is the lowest-order equation that describes optical pulse propagation in microresonators. We can usefully write it as

$$T_R \frac{\partial \Psi}{\partial \tau} = -\frac{i\beta_2}{2} \frac{\partial^2 \Psi}{\partial \theta^2} + i\gamma |\Psi|^2 \Psi, \tag{1}$$

where τ is time, θ is the azimuthal coordinate, $\Psi(\theta, \tau)$ is the field envelope of a single

transverse optical mode, T_R is the round-trip propagation time and is the inverse of the free-spectral range (FSR), β_2 is the dispersion coefficient, γ is the Kerr coefficient. It is standard to normalize Ψ, so that it has units of power. The Kerr coefficient γ has units of inverse power, and is related to the physical Kerr coefficient γ_{ph} (in units of area/power) by the relation $\gamma = \gamma_{\text{ph}}/A_{\text{eff}}$, where A_{eff} is the mode effective area. The dispersion coefficient β_2 is unitless and corresponds to the usual physical dispersion coefficient β_{ph} (in units of time^2/distance) by the relation $\beta_2 = (8\pi^3 R/T_R^2)\,\beta_{\text{ph}}$, where $R = v_g T_R/(2\pi)$ is the mode radius and v_g is the group velocity.

The cnoidal wave solutions to the nonlinear Schrödinger equation can be written analytically using Jacobi elliptic functions [10]. The solutions that appear depend on whether the dispersion is anomalous ($\beta_2 < 0$) or normal ($\beta_2 > 0$). Cnoidal wave solutions in the anomalous dispersion regime come in two generic forms that can be expressed in terms of two different types of Jacobi elliptic functions [$\text{dn}(x|k^2)$, $\text{cn}(x|k^2)$]. In the normal dispersion regime cnoidal-wave solutions can be written analytically using the Jacobi elliptic function $\text{sn}(x|k^2)$. The parameter k is the modulus of these functions and determines how rapidly the Fourier spectrum of these functions falls off. For Jacobi elliptic functions, we have the following relations: When $k \to 0$, $\text{dn}(x|k^2) \to 1$, $\text{cn}(x|k^2) \to \cos(x)$, and $\text{sn}(x|k^2) \to \sin(x)$; When $k \to 1$, $\text{dn}(x|k^2) \to \text{sech}(x)$, $\text{cn}(x|k^2) \to \text{sech}(x)$, and $\text{sn}(x|k^2) \to \tanh(x)$. The period of the cnoidal waves is given by $4K(k)$, where $K(k)$ is a complete elliptic integral of the first kind [10]. We have $K(k) \to \pi/2$ as $k \to 0$ and $K(k) \to \ln[4/(1-k^2)^{1/2}]$ as $k \to 1$.

Just like solitons, cnoidal wave solutions to non-integrable equations, including the equations that describe microresonators, usually do not have an exact analytical expression. However, in the lossless case, the cnoidal wave solutions to the equation that we use to model microresonators (the Lugiato-Lefever equation) can be expressed in terms of the Jacobi elliptic functions, and when $k \to 1$, cnoidal wave solutions reduce to soliton solutions expressed in terms of the hyperbolic secant function [10].

1.3 The Lugiato-Lefever equation

The nonlinear Schrödinger equation does not include the effects of mode attenuation or an external pump. Both effects play a crucial role in microresonators. The lowest-order equation that include theese effects is the Lugiato-Lefever equation (LLE) [4, 11, 12], which may be written

$$T_R \frac{\partial \Psi}{\partial \tau} = -\frac{i\beta_2}{2}\frac{\partial^2 \Psi}{\partial \theta^2} + i\gamma|\Psi|^2\Psi + \left(-i\sigma - \frac{l}{2}\right)\Psi + i\sqrt{P_{\text{in}}}, \tag{2}$$

where σ is the detuning of the pump frequency from the mode resonance, l is the damping coefficient, and P_{in} is the input pump power that is in the cavity mode that pumps the comb.

Equation (2) can be written in terms of three normalized parameters. One standard way to normalize Eq. (2) is to let $t = l\tau/2T_R$, $\psi = (2\gamma/l)^{1/2}\Psi$, $\beta = 2\beta_2/l$. The normalized detuning is expressed as

$$\alpha = \frac{2\sigma}{l}, \tag{3}$$

and the normalized pump amplitude is expressed as

$$F = i\sqrt{\frac{8\gamma P_{\text{in}}}{l^3}}. \tag{4}$$

Equation (2) now becomes

$$\frac{\partial \psi}{\partial t} = -\frac{i\beta}{2}\frac{\partial^2 \psi}{\partial \theta^2} + i|\psi|^2\psi - (i\alpha + 1)\,\psi + F. \tag{5}$$

We will be focusing in this chapter on the anomalous dispersion regime where $\beta < 0$.

In this case, it is useful to let $x = (2/|\beta|)^{1/2}\theta$, in which case Eq. (5) becomes

$$\frac{\partial \psi}{\partial t} = i\frac{\partial^2 \psi}{\partial x^2} + i|\psi|^2\psi - (i\alpha + 1)\,\psi + F. \tag{6}$$

Only the parameters α and F appear explicitly in Eq. (6). The third parameter appears implicitly in the boundary conditions. The domain of the azimuthal coordinate, $\theta = [-\pi, \pi]$, is replaced by the domain $x = [-L/2, L/2]$, where $L = (8\pi^2/|\beta|)^{1/2}$ is the mode circumference $2\pi R$ normalized to the dispersive scale length. The solution obeys periodic boundary conditions, i.e., $\psi(-L/2, t) = \psi(L/2, t)$. This normalization is useful because $|\beta| \ll 1$ for realistic experimental parameters, and it allows us to conveniently explore the limit $L \to \infty$.

An alternative is to normalize Eq. (2) with respect to the detuning, assumed positive, so that $t = \sigma\tau/T_R$, $x = (2\sigma/|\beta_2|)^{1/2}\theta$, $\psi = (\gamma/2\sigma)^{1/2}A$, $\delta = l/2\sigma$, and $h = (\gamma/2\sigma^3)^{1/2}\sqrt{P_{\text{in}}}$. In this case, Eq. (2) becomes

$$\frac{\partial \psi}{\partial t} = i\frac{\partial^2 \psi}{\partial x^2} + 2i|\psi|^2\psi - (i + \delta)\,\psi + ih. \tag{7}$$

The periodic domain is now given by $x = [-L_\delta/2, L_\delta/2]$, where $L_\delta = (8\pi^2\sigma/|\beta_2|)^{1/2}$. This normalization is theoretically useful since it can be used to conveniently connect the computational solutions of the LLE to the analytical solutions in the limit $\delta \to 0$ [13]. However, it is not useful for describing experiments, in which the detuning and the pump power are varied, and the detuning can have any sign. As discussed in Sec. 1.2, we will refer to any waveform that repeats periodically with periodically-spaced amplitude peaks within the entire mode circumference $\theta = [-\pi, \pi]$ or $x = [-L/2, L/2]$ as a cnoidal wave.

In experimental work, typical values of F range from 0 to 4, while typical values of α range from -5 to 10. The corresponding device parameters vary greatly, depending on the material from which the device is made and its size. Table 1 shows the

Table 1: Physical device parameters for different experimental devices. The first column gives the paper reference. The second column gives the Kerr coefficient (γ). The third column gives the pump wavelength (λ_p). The fourth column gives the quality factor (Q). The fifth column gives the chromatic dispersion in physical units (β_{ph}). The sixth column gives the detuning corresponding to $\alpha = 1$. The seventh column gives the input power corresponding to $F = 1.5$. The eighth column gives the normalized mode circumference (L).

Ref.	γ [$\text{W}^{-1}\text{km}^{-1}$]	λ_p [nm]	Q	β_{ph} [$\text{ps}^2\text{km}^{-1}$]	$\Delta\lambda$ [fm]	P_{in} [mW]	L
[14]	633	1551	$3 \cdot 10^6$	-61	334	9.0	31.3
[15]	800	1562	$3 \cdot 10^5$	-47	2913	1060	106
[5]	0.405	1553	$4 \cdot 10^8$	-9.4	1.97	21.6	35.1
[16]	0.228	1552	$1.7 \cdot 10^9$	-3	0.46	16.2	171
[17]	9.49	1562	$2.5 \cdot 10^8$	-6.3	3.34	2.03	120

experimental parameters that correspond to $\alpha = 1$ and $F = 1.5$ for several different experimental devices. The normalized mode circumference L ranges between 30 and 200.

2 Nonlinear frequency combs generated by cnoidal waves in microring resonators

2.1 Introduction

The generation of frequency combs in a nonlinear microresonator is governed by the Lugiato-Levefer equation (LLE) [4,11,12,18–22]. Periodic patterns that are called Turing rolls have been experimentally observed [3] and computationally studied [18] in microresonators. However, the relationship of these solutions to solitons has been unclear. This chapter aims at filling this gap.

The LLE has analytical soliton solutions when loss is neglected. While analytical solutions no longer exist when loss is included, the lossless solutions still have great value since the soliton solutions in the presence of loss sometimes referred to as dissipative solitons closely resemble their lossless counterparts. Moreover, the analytical relationships among the soliton amplitude, duration, and pedestal size have been a useful guide to experiments and a useful starting point for computational and perturbative studies. It appeared reasonable at the outset of our study to suppose that the solutions of the lossless LLE would be similarly useful. We will show however that except in the single soliton or soliton crystal limit, these periodic solutions become unstable when only a small amount of loss is introduced. Turing rolls, which are cnoidal waves with a large periodicity and a large pedestal, only become stable when the loss exceeds a threshold; nonetheless, the waveforms of the lossless solutions with a given periodicity resemble the stable solutions with loss that have the same periodicity, as we will also show.

In this chapter, we study the cnoidal wave solutions of the LLE in the anomalous dispersion regime of a microresonator, which are periodic generalizations of the soliton solutions. We show that the family of solutions that includes solitons and Turing rolls can all be represented analytically as Jacobi elliptic functions [10] when loss is

neglected. In Sec. 1.2, we have shown the properties of cnoidal waves. For the LLE, when $k \to 1$, the cnoidal wave solutions reduce to the soliton solutions that Matsko *et al.* [11] found. We will extend this study to a more general case where cnoidal wave solutions dominate.

The outline of this chapter is as follows: Section 2.2 presents the general Hamiltonian description of the lossless LLE equation for stationary (time-independent) solutions. Section 2.3 focuses on the derivation of the stationary cnoidal wave solutions in terms of Jacobi elliptic functions and elucidates the conditions under which the general family of solutions reduces to the single soliton solution that has been described in [11]. Moreover, we discuss their periodicity, stability, and spectral properties. From an experimental perspective, it is also important to assess the spectral properties of the frequency combs generated by these cnoidal waves, as well as their accessibility from a broad range of initial conditions in the case of non-zero damping, when analytical solutions are no longer available. Hence, in Sec. 2.4 we computationally study the periodic solutions in the presence of loss. We characterize their spectral properties, and we discuss their accessibility from impulsive initial conditions as a function of the external pump strength h and the damping or loss coefficient δ. We also discuss how these solutions apply to microresonators. Finally, in Sec. 2.5 we present our conclusions.

The work that is presented in this chapter has been published in Ref. [13].

2.2 Hamiltonian Approach and Qualitative Analysis

In this section, we qualitatively study the stationary solutions admitted by the LLE using a Hamiltonian approach. We categorize the different kinds of solutions and determine the parameter regime in which they are found. Following the derivations in Sec. 1.3, we normalize Eq. (2) with respect to the detuning and obtain the LLE in

the form, as previously defined in Eq. (7)

$$i\frac{\partial\psi}{\partial t}+\frac{\partial^2\psi}{\partial x^2}-\psi+2|\psi|^2\psi=-i\delta\psi-h, \tag{8}$$

To obtain the stationary solutions of Eq. (8), we set the temporal derivative equal to zero, and obtain the equation

$$\frac{\mathrm{d}^2\psi}{\mathrm{d}x^2}+h+(i\delta-1)\,\psi+2|\psi|^2\psi=0. \tag{9}$$

This equation does not have analytical solutions that are expressible as Jacobi elliptic functions for $\delta\neq 0$. Thus, our analytical discussion of solutions is focused on the lossless case. Without loss of generality, for $\delta=0$, the field ψ can be considered real, and Eq. (9) becomes

$$\frac{\mathrm{d}^2\psi}{\mathrm{d}x^2}+h-\psi+2\psi^3=0, \tag{10}$$

Equation (10) has the Hamiltonian

$$H=\frac{1}{2}\left(\frac{\mathrm{d}\psi}{\mathrm{d}x}\right)^2+V\left(\psi\right), \tag{11}$$

where V is the potential

$$V=h\psi-\frac{\psi^2}{2}+\frac{\psi^4}{2}. \tag{12}$$

The Hamiltonian is constant at all x. Equation (11) can be integrated to yield the first order differential equation

$$\frac{\mathrm{d}\psi}{\mathrm{d}x}=\sqrt{2H-2h\psi+\psi^2-\psi^4}, \tag{13}$$

which can be solved by quadrature in terms of elliptic integrals [10]

$$\int dx = \int \frac{d\psi}{\sqrt{2H - 2h\psi + \psi^2 - \psi^4}}. \tag{14}$$

The period of the solution is a function of h and H. In a microresonator, this period will be quantized, and we consider this issue explicitly in Sec. 2.4.

We observe that the potential in Eq. (12) is asymmetric with respect to ψ when the pump $h \neq 0$. As consequence, the cnoidal wave solutions will have a non-zero pedestal. This pedestal was already noted in the special case of single solitons [11]. From Eq. (14), we obtain the equation

$$-\psi^4 + \psi^2 - 2h\psi + 2H = 0. \tag{15}$$

In the next section we will study the analytical solutions of Eq. (14); here, we provide a qualitative analysis that elucidates the different regimes. The radicand of Eq. (14) is a quartic polynomial that has three extrema when $h < \sqrt{2/27}$, while it has only one extremum when $h > \sqrt{2/27}$. The discriminant of Eq. (15) is

$$\Delta = -2048H^3 - 512H^2 + 1152h^2H - 32H - 432h^4 + 16h^2. \tag{16}$$

We can rewrite Eq. (15) as

$$-(\psi - \psi_1)(\psi - \psi_2)(\psi - \psi_3)(\psi - \psi_4) = 0, \tag{17}$$

where the four roots ψ_1, ψ_2, ψ_3, ψ_4 of the quartic polynomial are respectively

$$\begin{aligned}
\psi_1 &= \frac{1}{2}\sqrt{t_3} + \frac{1}{2}\left(2 - t_3 - \frac{4h}{\sqrt{t_3}}\right)^{1/2}, \\
\psi_2 &= \frac{1}{2}\sqrt{t_3} - \frac{1}{2}\left(2 - t_3 - \frac{4h}{\sqrt{t_3}}\right)^{1/2}, \\
\psi_3 &= -\frac{1}{2}\sqrt{t_3} + \frac{1}{2}\left(2 - t_3 + \frac{4h}{\sqrt{t_3}}\right)^{1/2}, \\
\psi_4 &= -\frac{1}{2}\sqrt{t_3} - \frac{1}{2}\left(2 - t_3 + \frac{4h}{\sqrt{t_3}}\right)^{1/2},
\end{aligned} \tag{18}$$

with

$$\begin{aligned}
t_1 &= -4\left(1 - 24H\right)^3 + \left(2 - 108h^2 + 144H\right)^2, \\
t_2 &= -2 + 108h^2 - 144H - \sqrt{t_1}, \\
t_3 &= \frac{2}{3} + \frac{\sqrt[3]{2}\left(1 - 24H\right)}{3\sqrt[3]{t_2}} + \frac{\sqrt[3]{t_2}}{3\sqrt[3]{2}}.
\end{aligned} \tag{19}$$

Figures 2(a) and 2(b) show the potential V as a function of ψ for $h = 0.1$, so that $h < \sqrt{2/27}$, and for $h = 0.5$, so that $h > \sqrt{2/27}$. Their corresponding phase portraits are shown in Figs. 2(c) and 2(d), respectively. As shown in Fig. 2(a), for $h = 0.1$, the potential has three extrema, two of them are minima and one is a local maximum. The Hamiltonian at the local maximum corresponds to the soliton solutions of Eq. (8), which are represented by the separatrix of the phase space that is shown as line b in Fig. 2(c). The separatrix consists of two homoclinic orbits, which correspond to two different types of single soliton solutions: The separatrix on the right corresponds to a positive soliton solution, and the separatrix on the left corresponds to a negative soliton solution with a positive pedestal. It was previously shown that only the negative solution is stable [23]. The positive and negative solitons are solutions of an externally-driven-damped nonlinear Schrödinger equation on an infinite line [23]. The periodic orbits, which are also called cycles, are related to

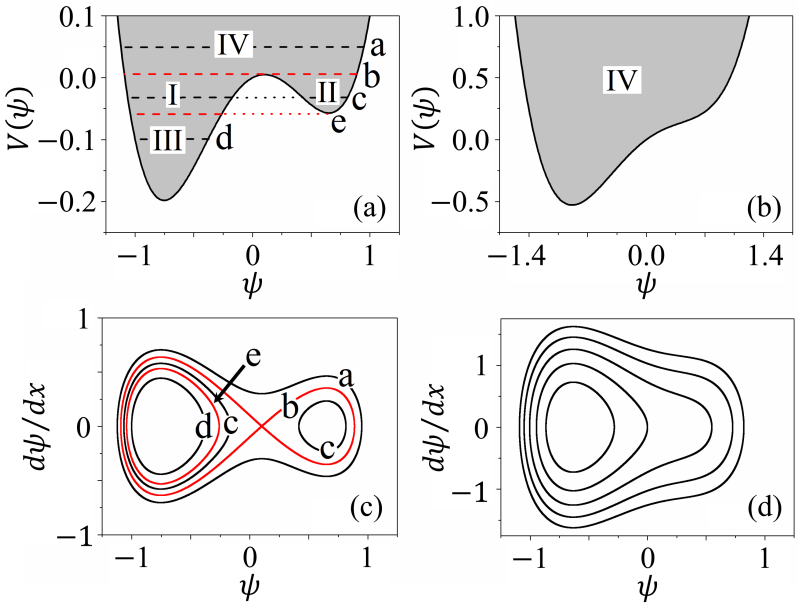

Figure 2: Potential V and phase portraits of Eq. (10) for different magnitudes of the external pump h. The potential V is shown as a function of ψ respectively in (a) for $h = 0.1$ (3 extrema) and in (b) for $h = 0.5$ (one extremum). The shaded areas are the regions where the solutions exist. Referring to (a), regions I and II are bounded by lines b and e, region III is below line e, and region IV is above line b. The lines a, b, c, and d correspond respectively to values of the Hamiltonian $H = 0.05$, $H = 0.00505$, $H = -0.03$, and $H = -0.1$. The radicand of Eq. (14) has four real solutions in regions I and II, while it has two real and two complex conjugate solutions in regions III and IV. The corresponding phase portraits are shown in the $(\psi, d\psi/dx)$-plane respectively in (c) for $h = 0.1$ and in (d) for $h = 0.5$.

the cnoidal-wave solutions. Specifically, as we will discuss in Sec. 2.3, cycles outside the separatrix correspond to solutions that can be expressed in terms of the Jacobi elliptic cn functions, which we call cn-wave solutions. Cycles inside the separatrix can be expressed in terms of either cn functions or dn functions, which we call dn-wave solutions. It is important to note that the soliton solutions are accessible when $h \leq \sqrt{2/27}$, as shown in Fig. 2(c), while they are not accessible when $h > \sqrt{2/27}$, as shown Fig. 2(d).

We may separate the solutions of Eq. (10) into 3 cases:

1. When $\Delta > 0$ and $\mathrm{Re}\big(2 - t_3 - 4h/\sqrt{t_3}\big) > 0$, the radicand of Eq. (14) has four real solutions, which corresponds to regions I and II in Fig. 2.

2. When $\Delta < 0$, $\mathrm{Re}\big(2 - t_3 - 4h/\sqrt{t_3}\big) < 0$ and $\mathrm{Re}\big(2 - t_3 + 4h/\sqrt{t_3}\big) > 0$, the radicand of Eq. (14) has two real solutions and two complex conjugate solutions, which corresponds to region III in Fig. 2.

3. When $\Delta < 0$ and $\mathrm{Re}\big(2 - t_3 - 4h/\sqrt{t_3}\big) > 0$, the radicand of Eq. (14) also has two real solutions and two complex conjugate solutions, which corresponds to region IV in Fig. 2.

In Sec. 2.3, we discuss the analytical solutions for these cases.

2.3 Cnoidal Wave Solutions with zero damping ($\delta = 0$)

In this section, we separately analyze the three cases that we have just identified, and we then show how the cnoidal wave solutions that are expressible in terms of Jacobi elliptic functions reduce to the soliton solutions that are expressible in terms of hyperbolic functions when the parameter k of the elliptic functions becomes equal to one, and, finally, we analyze the periodicity, stability and spectral properties of the cnoidal waves.

For each of the three cases, the solutions can be grouped into two sets: For $k = 1$, Set I reduces to the positive soliton solutions already found in [11], while Set II reduces to the negative soliton solutions of [11]. Figures 3 and 4 show respectively several examples of cnoidal wave solutions for Set I and Set II.

2.3.1 The cnoidal wave solutions of Set I

2.3.1.1 $\Delta > 0$ and $\mathrm{Re}\big(2 - t_3 - 4h/\sqrt{t_3}\big) > 0$ When $\Delta > 0$ and $\mathrm{Re}\big(2 - t_3 - 4h/\sqrt{t_3}\big) > 0$, the radicand of Eq. (14) has four real roots.

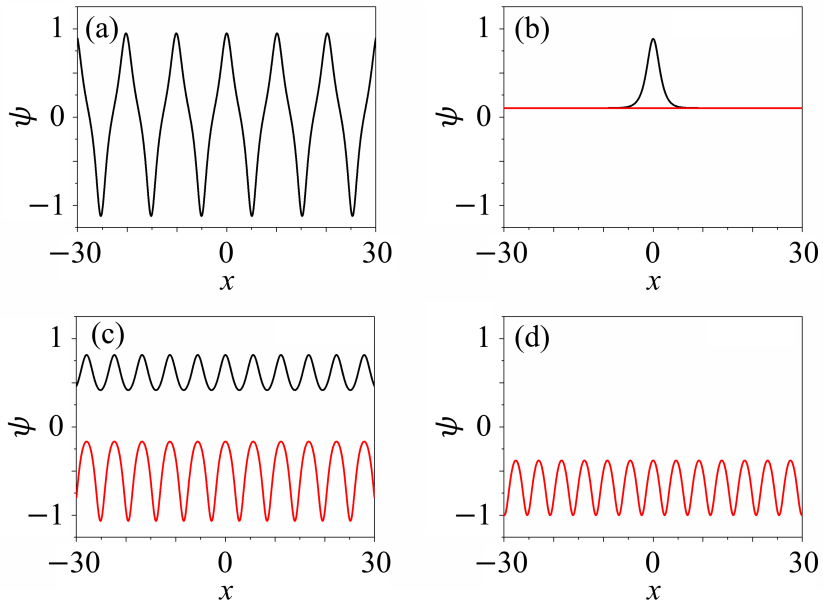

Figure 3: Profiles of the cnoidal-wave solutions ψ of Set I as a function of x with different values of Hamiltonian H for $h = 0.1$. The solutions in (a), (b), (c), and (d) correspond to the lines a, b, c, and d in Figs. 2(a) and (c), respectively. Line b is the separatrix where soliton solutions are found. (a) We show the cnoidal-wave solution at $H = 0.05$. (b) We show the two possible solutions at $H = 0.00505$, the positive soliton solution (black curve) and the continuous-wave solution (red curve). (c) We show the cnoidal-wave solutions with $H = -0.03$. The upper curve (positive cnoidal wave) is the solution corresponding to the closed orbit c located at $\psi > 0$ in Fig. 2(c). The lower curve (negative cnoidal wave) is the solution corresponding to the closed orbit c located at $\psi < 0$ in Fig. 2(c). (d) We show the cnoidal-wave solution with $H = -0.1$ corresponding to to the closed orbit d.

For $\psi_4 \leqslant \psi < \psi_3$, we have

$$\psi = \psi_{+\mathrm{dn1}} = \frac{F\psi_3 - C\psi_2}{F - C} \times \left[1 + \frac{\dfrac{2FC\,(\psi_2 - \psi_3)}{(F\psi_3 - C\psi_2)\,(F + C)}}{1 + \dfrac{F - C}{F + C}\mathrm{nd}\left(\dfrac{x}{g_{\mathrm{nd}}}|k_{\mathrm{nd}}^2\right)} \right], \tag{20}$$

and for $\psi_2 \leqslant \psi < \psi_1$, we have

$$\psi = \psi_{+\mathrm{dn2}} = \frac{F\psi_1 + B\psi_4}{F+B} \times \left[1 + \frac{2FB\,(\psi_1 - \psi_4)}{(F\psi_1 + B\psi_4)\,(F-B)}\right], \qquad (21)$$

$$1 + \frac{F+B}{F-B}\mathrm{nd}\left(\frac{x}{g_{\mathrm{nd}}}|k_{\mathrm{nd}}^2\right)$$

where $\mathrm{nd}(x|k^2) = 1/\mathrm{dn}(x|k^2)$ is the inverse of $\mathrm{dn}(x|k^2)$ [10],

$$\begin{aligned} B &= \psi_1 - \psi_2 = \left(2 - t_3 - 4h/\sqrt{t_3}\right)^{1/2}, \\ C &= \psi_3 - \psi_4 = \left(2 - t_3 + 4h/\sqrt{t_3}\right)^{1/2}, \\ F &= (\psi_2 - \psi_4)\,k_d, \\ g_{\mathrm{nd}} &= g_d/\,(1+k_d)\,, \\ k_{\mathrm{nd}} &= 2\sqrt{k_d/\,(1+k_d)}, \end{aligned} \qquad (22)$$

with

$$g_d = \ 2/\sqrt{(\psi_1 - \psi_3)\,(\psi_2 - \psi_4)}, \qquad (23)$$

and

$$k_d = \ \left[\frac{(\psi_1 - \psi_2)\,(\psi_3 - \psi_4)}{(\psi_1 - \psi_3)\,(\psi_2 - \psi_4)}\right]^{1/2}. \qquad (24)$$

The profiles of the cnoidal wave solutions for $H = 0$ and $h = 0.1$ are shown in Fig. 3(c).

2.3.1.2 $\Delta < 0$**,** $\mathbf{Re}\left(2 - t_3 - 4h/\sqrt{t_3}\right) < 0$**, and** $\mathbf{Re}\left(2 - t_3 + 4h/\sqrt{t_3}\right) > 0$ When $\Delta < 0$, $\mathrm{Re}\left(2 - t_3 - 4h/\sqrt{t_3}\right) < 0$, and $\mathrm{Re}\left(2 - t_3 + 4h/\sqrt{t_3}\right) > 0$, the radicand of Eq. (14) has two real roots and a pair of complex conjugate roots. Here, the real roots are ψ_3 and ψ_4, while the complex conjugate roots are ψ_1 and ψ_2. We let $\psi_1 = \rho_{c1} + i\eta_{c1}$ and $\psi_2 = \rho_{c1} - i\eta_{c1}$.

For $\psi_4 \leqslant \psi < \psi_3$, we have

$$\psi = \psi_{+\mathrm{cn}3} = \frac{B_{c1}\psi_3 + A_{c1}\psi_4}{B_{c1} + A_{c1}} \times \left[1 + \frac{\dfrac{2A_{c1}B_{c1}\left(\psi_3 - \psi_4\right)}{\left(B_{c1}\psi_3 + A_{c1}\psi_4\right)\left(B_{c1} - A_{c1}\right)}}{1 + \dfrac{B_{c1} + A_{c1}}{B_{c1} - A_{c1}} \mathrm{nc}\left(\sqrt{A_{c1}B_{c1}}x|{k_3}^2\right)} \right], \tag{25}$$

where $\mathrm{nc}(x|k^2) = 1/\mathrm{cn}(x|k^2)$ is the inverse of the Jacobian elliptic cosine function $\mathrm{cn}(x|k^2)$ [10],

$$\begin{aligned} A_{c1} &= \left[\left(\rho_{c1} - \psi_3\right)^2 + \eta_{c1}^2\right]^{1/2}, \\ B_{c1} &= \left[\left(\rho_{c1} - \psi_4\right)^2 + \eta_{c1}^2\right]^{1/2}, \\ k_3 &= \left[\frac{\left(\psi_3 - \psi_4\right)^2 - \left(A_{c1} - B_{c1}\right)^2}{4A_{c1}B_{c1}}\right]^{1/2}. \end{aligned} \tag{26}$$

The profile of the cnoidal wave solution for $H = -0.1$ and $h = 0.1$ is shown in Fig. 3(d).

2.3.1.3 $\Delta < 0$ **and** $\mathbf{Re}\left(2 - t_3 - 4h/\sqrt{t_3}\right) > 0$ When $\Delta < 0$ and $\mathrm{Re}\left(2 - t_3 - 4h/\sqrt{t_3}\right) > 0$, the radicand of Eq. (14) also has two real roots and a pair of complex conjugate roots. Here, the real roots are ψ_1 and ψ_4, while the complex conjugate roots are ψ_2 and ψ_3. We let $\psi_2 = \rho_{c2} + i\eta_{c2}$ and $\psi_3 = \rho_{c2} - i\eta_{c2}$.

For $\psi_4 \leqslant \psi < \psi_1$, we have

$$\psi = \psi_{+\mathrm{cn}4} = \frac{B_{c2}\psi_1 + A_{c2}\psi_4}{B_{c2} + A_{c2}} \times \left[1 + \frac{\dfrac{2A_{c2}B_{c2}\left(\psi_1 - \psi_4\right)}{\left(B_{c2}\psi_1 + A_{c2}\psi_4\right)\left(B_{c2} - A_{c2}\right)}}{1 + \dfrac{B_{c2} + A_{c2}}{B_{c2} - A_{c2}} \mathrm{nc}\left(\sqrt{A_{c2}B_{c2}}x|{k_4}^2\right)} \right], \tag{27}$$

where

$$
\begin{aligned}
A_{c2} &= \left[(\rho_{c2}-\psi_1)^2+\eta_{c2}^2\right]^{1/2}, \\
B_{c2} &= \left[(\rho_{c2}-\psi_4)^2+\eta_{c2}^2\right]^{1/2}, \\
k_4 &= \left[\frac{(\psi_1-\psi_4)^2-(A_{c2}-B_{c2})^2}{4A_{c2}B_{c2}}\right]^{1/2}.
\end{aligned}
\tag{28}
$$

We show the profile of the cnoidal wave solution for $H = 0.01$ and $h = 0.1$ in Fig. 3(a).

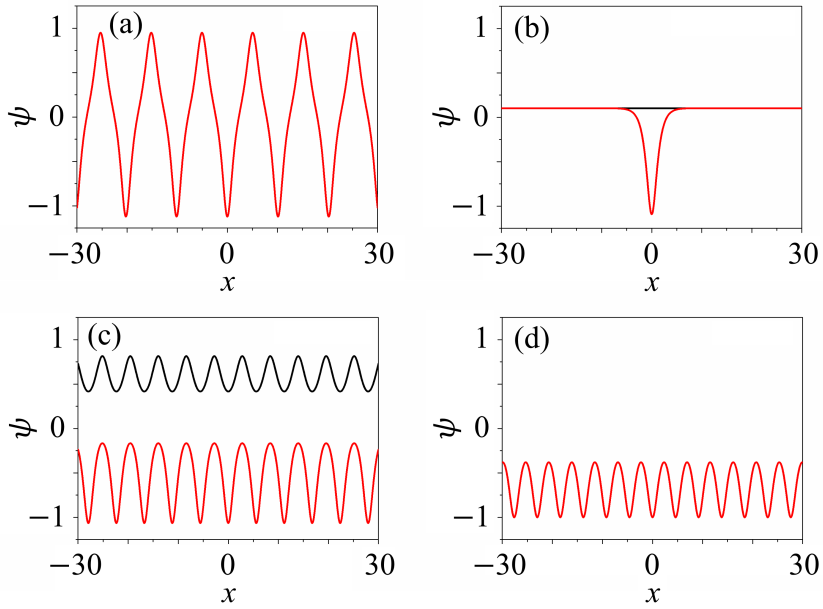

Figure 4: The solutions ψ of Set II as a function of x at different values of the Hamiltonian H for $h = 0.1$. The solutions in (a), (b), (c), and (d) correspond to the lines a, b, c, and d in Figs. 2(a) and (c), respectively. We show (a) the cnoidal-wave solution at $H = 0.05$, (b) the negative soliton solution and the continuous-wave solution at $H = 0.00505$, (c) the positive and negative cnoidal-wave solutions at $H = -0.03$, and (d) the cnoidal-wave solution at $H = -0.1$.

2.3.2 The cnoidal wave solutions of Set II

2.3.2.1 $\Delta > 0$ **and** $\mathbf{Re}\big(2 - t_3 - 4h/\sqrt{t_3}\big) > 0$ When $\Delta > 0$ and $\mathrm{Re}\big(2 - t_3 - 4h/\sqrt{t_3}\big) > 0$, the radicand of Eq. (14) has four real roots.

For $\psi_4 < \psi \leqslant \psi_3$, we have

$$\psi = \psi_{-\mathrm{dn1}} = \frac{C\psi_1 + E\psi_4}{C + E} \times \left[1 + \frac{2CE(\psi_1 - \psi_4)}{(C\psi_1 + E\psi_4)\,(C - E)} \right] \Bigg/ \left[1 - \frac{C + E}{C - E} \mathrm{nd}\left(\frac{x}{g_{\mathrm{nd}}} | k_{\mathrm{nd}}^2 \right) \right], \tag{29}$$

and for $\psi_2 < \psi \leqslant \psi_1$, we have

$$\psi = \psi_{-\mathrm{dn2}} = \frac{B\psi_3 - E\psi_2}{B - E} \times \left[1 + \frac{2BE(\psi_2 - \psi_3)}{(B\psi_3 - E\psi_2)\,(B + E)} \right] \Bigg/ \left[1 - \frac{B - E}{B + E} \mathrm{nd}\left(\frac{x}{g_{\mathrm{nd}}} | k_{\mathrm{nd}}^2 \right) \right], \tag{30}$$

where $E = (\psi_1 - \psi_3)\, k_d$, B, C, g_{nd}, k_{nd} are defined in Eq. (20). The profile of the cnoidal wave solutions for $H = 0$ and $h = 0.1$ is shown in Fig. 4(c).

2.3.2.2 $\Delta < 0$**,** $\mathbf{Re}\big(2 - t_3 - 4h/\sqrt{t_3}\big) < 0$**, and** $\mathbf{Re}\big(2 - t_3 + 4h/\sqrt{t_3}\big) > 0$ When $\Delta < 0$, $\mathrm{Re}\big(2 - t_3 - 4h/\sqrt{t_3}\big) < 0$, and $\mathrm{Re}\big(2 - t_3 + 4h/\sqrt{t_3}\big) > 0$, the radicand of Eq. (14) has two real roots and a pair of complex conjugate roots. Here, the real roots are ψ_3 and ψ_4, while the complex conjugate roots are ψ_1 and ψ_2. We let $\psi_1 = \rho_{c1} + i\eta_{c1}$ and $\psi_2 = \rho_{c1} - i\eta_{c1}$.

For $\psi_4 < \psi \leqslant \psi_3$, we have

$$\psi = \psi_{-\mathrm{cn3}} = \frac{B_{c1}\psi_3 + A_{c1}\psi_4}{B_{c1} + A_{c1}} \times \left[1 + \frac{2A_{c1}B_{c1}\,(\psi_3 - \psi_4)}{(B_{c1}\psi_3 + A_{c1}\psi_4)\,(B_{c1} - A_{c1})} \right] \Bigg/ \left[1 - \frac{B_{c1} + A_{c1}}{B_{c1} - A_{c1}} \mathrm{nc}\left(\sqrt{A_{c1}B_{c1}}\, x | {k_3}^2 \right) \right], \tag{31}$$

where A_{c1}, B_{c1}, and k_3 are defined in Eq. (25). The profile of the cnoidal wave solution for $H = -0.1$ and $h = 0.1$ is shown in Fig. 4(d).

2.3.2.3 $\Delta < 0$ **and** $\mathbf{Re}\left(2 - t_3 - 4h/\sqrt{t_3}\right) > 0$ When $\Delta < 0$ and $\mathrm{Re}\left(2 - t_3 - 4h/\sqrt{t_3}\right) > 0$, the radicand of Eq. (14) also has two real roots and a pair of complex conjugate roots. Here the real roots are ψ_1 and ψ_4, while the complex conjugate roots are ψ_2 and ψ_3. We let $\psi_2 = \rho_{c2} + i\eta_{c2}$ and $\psi_3 = \rho_{c2} - i\eta_{c2}$.

For $\psi_4 < \psi \leqslant \psi_1$, we have

$$\psi = \psi_{-\mathrm{cn}4} = \frac{B_{c2}\psi_1 + A_{c2}\psi_4}{B_{c2} + A_{c2}} \times \left[1 + \frac{\dfrac{2A_{c2}B_{c2}\left(\psi_1 - \psi_4\right)}{\left(A_{c2}\psi_4 + B_{c2}\psi_1\right)\left(B_{c2} - A_{c2}\right)}}{1 - \dfrac{B_{c2} + A_{c2}}{B_{c2} - A_{c2}}\mathrm{nc}\left(\sqrt{A_{c2}B_{c2}}x|{k_4}^2\right)}\right], \tag{32}$$

where A_{c2}, B_{c2}, and k_4 are defined in Eq. (27). The profile of the cnoidal wave solution for $H = 0.01$ and $h = 0.1$ is shown in Fig. 4(a).

2.3.3 The limiting case of the lossless soliton solutions

The cnoidal waves that are expressible in terms of Jacobi elliptic functions reduce to soliton solutions that are expressible in terms of hyperbolic functions when the parameter k of the elliptic functions $\mathrm{cn}(x|k^2)$ and $\mathrm{dn}(x|k^2)$ becomes equal to 1.

We first write the positive and negative soliton solutions of the LLE as [11]

$$\psi_{\pm} = \psi_0\left[1 + \frac{M_1}{1 \pm M_2\cosh\left(M_3 x\right)}\right], \tag{33}$$

where

$$\begin{aligned} M_1 &= 2\left(X - 1\right), \\ M_2 &= \sqrt{X}, \\ M_3 &= \sqrt{2\left(X - 1\right)/\left(2X + 1\right)}, \\ \psi_0 &= 1/\sqrt{2\left(1 + 2X\right)}, \end{aligned} \tag{34}$$

and X is the solution of the equation

$$\sqrt{2}X/\left(1+2X\right)^{3/2}=h. \tag{35}$$

We find that our Eqs. (21) and (27) reduce to the positive soliton solution of Eq. (33), as shown in Fig. 3(b), while Eqs. (29) and (32) reduce to the negative soliton solution of Eq. (33) as shown in Fig. 4(b).

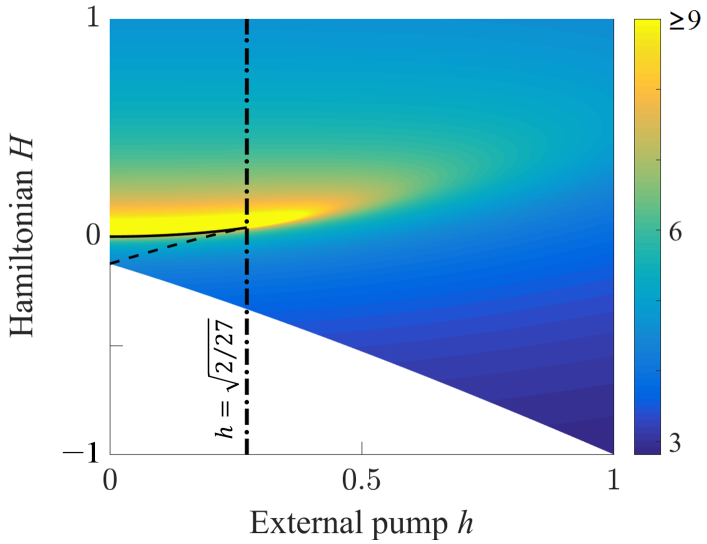

Figure 5: Period of the cnoidal waves in the (h,H) plane. The solid line indicates the loci of points in the parameter space where soliton solutions exist for which $P \to +\infty$. The region bounded by the solid line and by the dashed line is where positive and negative cnoidal-wave/soliton solutions coexist. The vertical dash-dotted line indicates the value of the pump at $h=\sqrt{2/27}$.

2.3.4 Periodicity, stability and spectral properties of the lossless cnoidal wave solutions

Figure 5 shows the period P in the (h,H) plane. For a fixed value of h, the period P of different cnoidal waves will be different. As a consequence, the spacing of the comb lines in their Fourier spectrum is different. In particular, as k approaches 1 and

the solutions approach soliton solutions, the period P tends to infinity, and the comb lines become more closely spaced. Moreover, only stable cnoidal waves can generate

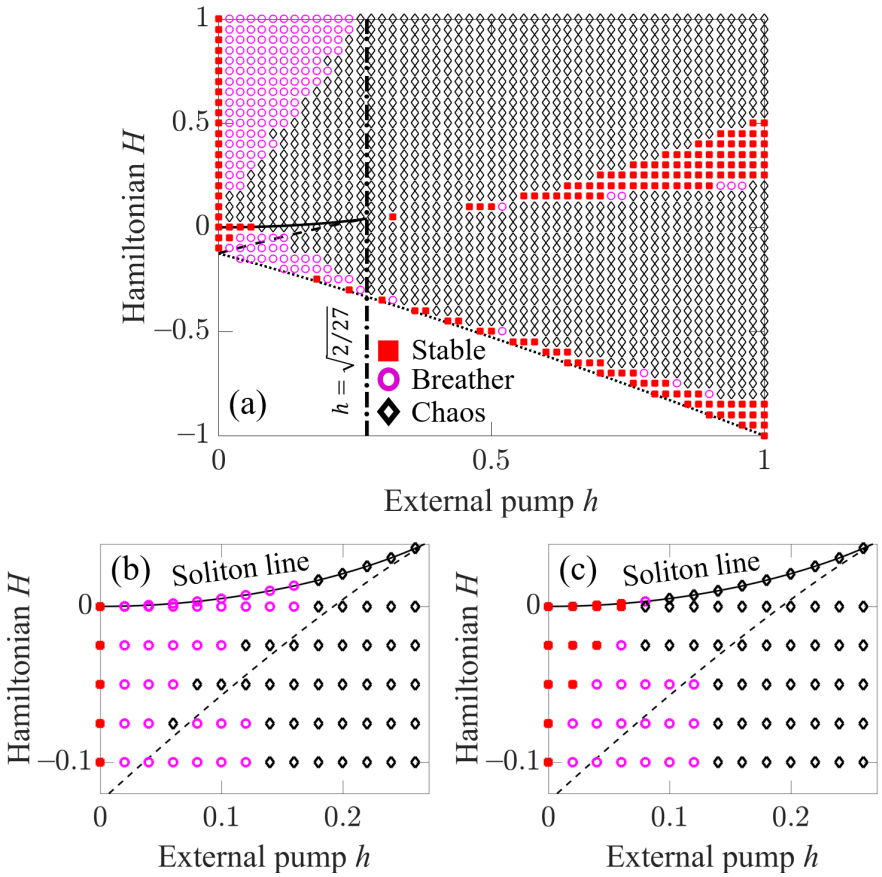

Figure 6: (a) Results of a computational study to assess the stability of the cnoidal waves in the (h,H) plane. The solid line indicates the loci of points in the parameter space where soliton solutions exist. The region bounded by the solid line and by the dashed line is where positive and negative cnoidal-wave/soliton solutions coexist. Here we report the results of the stability study for the negative solutions. The dotted line indicates the boundary of the existence region of cnoidal-wave solutions, and the vertical dash-dotted line indicates the value of the pump at $h = \sqrt{2/27}$. (b) Results of the stability study for positive solutions in a magnification of the region where positive and negative solution coexist. The solutions are always unstable for $h \neq 0$. (c) Results in the same region for negative solutions. In this case, stable negative soliton solutions and stable cnoidal waves exist.

reliable frequency combs. Thus, it is important to study both the periodicity and the

stability of the cnoidal wave solutions. The computational study of the stability of

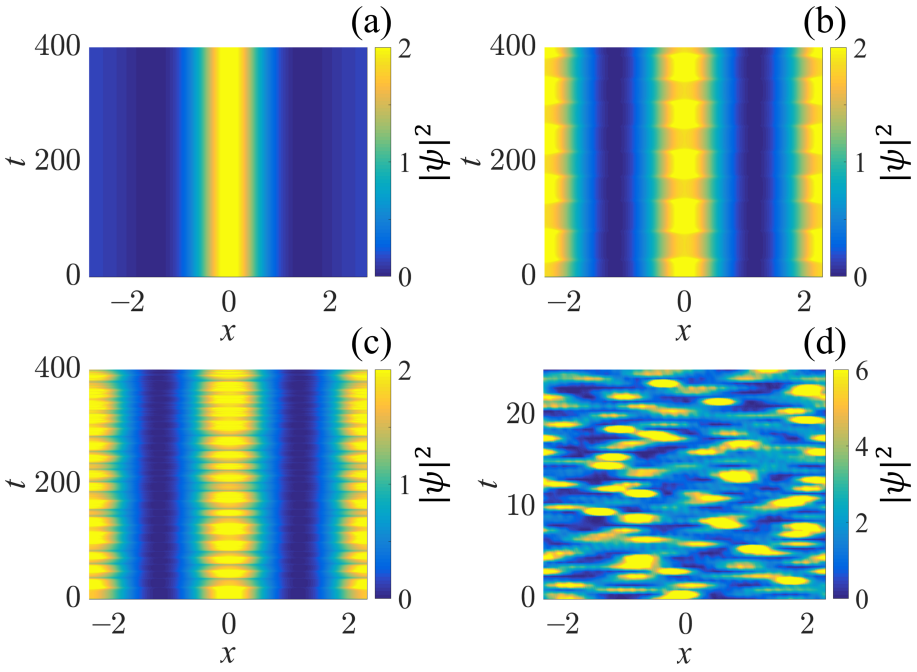

Figure 7: Spatio-temporal evolution of the intensity of the cnoidal wave for different values of H and h. The x-coordinate runs over one period of the cnoidal wave. The figure exemplifies four typical cases. (a) The cnoidal wave remains stable for $h = 0.7$ and $H = 0.2$. (b) The cnoidal wave evolves to a breather for $h = 0.16$ and $H = 1$. (c) The cnoidal wave generates temporal chaos for $h = 0.26$ and $H = 1$. (d) The cnoidal wave generates spatio-temporal chaos for $h = 0.45$ and $H = 1$.

cnoidal waves has been performed by the numerical integration of Eq. (8) in the time domain with $\delta = 0$ using a split-step algorithm [24] in which the initial conditions are the stationary cnoidal wave solutions of Eq. (10) that we have just derived. We show the results in Fig. 6. The small numerical noise intrinsic to the numerical method that we used to calculate the temporal evolution acts as a perturbation on the analytical solution. Hence, we expect that the profile of the analytical solution remains nearly unchanged during its temporal evolution if the solution is stable; otherwise, we expect that the solution either undergoes periodic oscillations in time, which corresponds to a breather, or becomes chaotic. This approach produces ambiguous results near the

stability boundary, as is apparent in Fig. 6. Linearization of the evolution equations, combined with a spectral analysis of the linearized equations, has to be used to unambiguously determine the boundary. However, the ambiguous region is narrow in this case and does not affect our conclusions. Three regions of stability for the cnoidal waves in the (h,H) plane are present. The first one lies at the border of the domain of the allowed solutions, close to where the Hamiltonian H intersects the potential V at its absolute minimum. These solutions might not be interesting from an experimental perspective because of their small amplitude. A second region of stability is visible in Fig. 6(c). The stable solutions lie in the region bounded by the soliton line, the dash-dotted line and the $h = 0$ axis. These cnoidal wave solutions are akin to the stable negative soliton solutions studied in the past for the ac-driven, nonlinear Schrödinger equation on an infinite line [23]. However, we note that the stability region is confined to small values of the external pump h with $h \lesssim 0.05$. Hence, small fluctuations of the average power of the external pump can destabilize the system, turning the stable solutions into breathers or chaotic states.

Yet a third region of stability is visible in Fig. 6(a). In this case, the stable solutions are obtained for $h \gtrsim 0.5$, $H \gtrsim 0$ and periodicity $4 \lesssim P \lesssim 6$. These solutions should be visible in experiments, especially in practical situations where loss in the microresonator are important and, thus, higher pump power would be needed to generate a comb. A study of the accessibility of these stable solutions in the practical case where losses are considered will be presented in the next section. An example of the evolution of the cnoidal waves for different values of H and h is provided in Fig. 7.

It may seem surprising at first that it is possible to obtain stable solutions when $\delta = 0$ since the pump is non-zero. However, an analysis of Eq. 8 shows that the pump adds no energy to the solution when $\int_{-P/2}^{P/2} h(\psi - \psi^*)dx = 0$, which is the case for all the analytical solutions. Physically, this condition implies that the pump is out

of phase with the cnoidal waves. We have found that even when the solutions are unstable, they are chaotic or oscillatory and do not blow up.

In Fig. 8, we show the Fourier spectra of the cnoidal waves and of the positive and negative solitons for the solutions reported in Figs. 3 and 4. It is seen that the Fourier spectra all have a triangular shape on a logarithmic scale, indicating an exponential fall-off. This triangular shape is a typical signature of the spectrum of parametrically-driven systems where the energy is transfered from the dominant spectral component to the side-band spectral components due to the modulational instability induced by four-wave mixing [25]. We see that all the spectra look similar, except for the spacing of the spectral lines. As the period grows, the spacing of the spectral lines diminishes. In principle, for the soliton solution at $k = 1$ for which $P \to \infty$, the spacing becomes zero and there are no longer individual spectral lines.

In a microresonator, the spacing between the comb lines is determined by the device, and the spacing of the spectral lines must be a multiple M of the device's FSR. The soliton solutions in microresonators correspond to k-values that are slightly less than 1. By appropriately choosing the device parameters and pump strength when the cnoidal waves exist stably and are accessible, it is possible to choose a desirable k-value and multiple M of the FSR and thereby tailor a comb with a desired spectral spacing and exponential falloff. In particular, we note that cnoidal waves in regions II, III, and IV that are near the bottom of the potential well will have nearly sinusoidal oscillations and a rapid spectral falloff. Generating cnoidal waves with M periods in the microresonator will lead to a spectral spacing that is M times the FSR. Widely spaced comb lines with a rapid exponential falloff are useful, for example, in the search for earth-like planets [26].

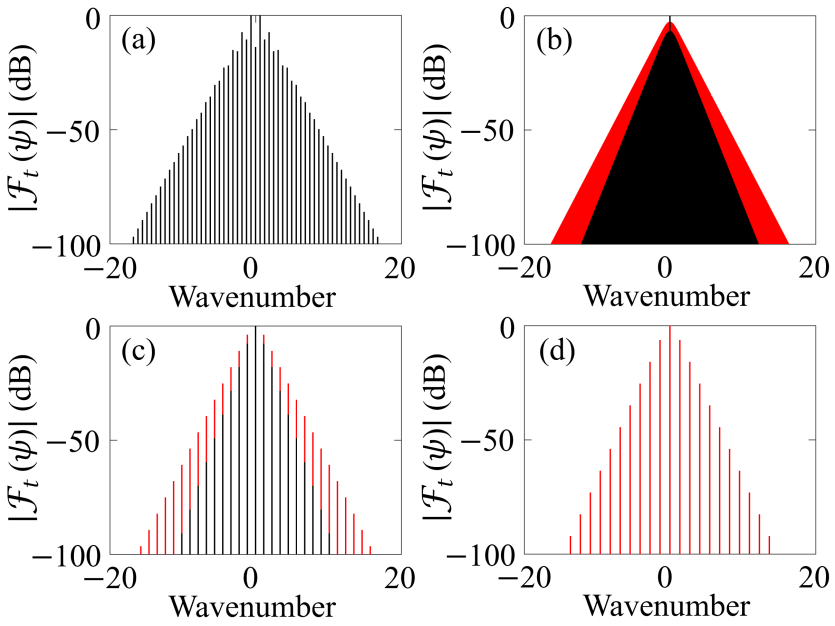

Figure 8: Absolute value of the Fourier transform ($\mathcal{F}_t$) of the cnoidal wave solutions that are plotted in Figs. 3 and 4 respectively. The wavenumber equals $(m - m_d)2\pi/P$, where m_d is the mode number of the dominant mode. (a) Fourier spectra of the cnoidal waves that are plotted in Figs. 3(a) and 4(a) with $H = 0.05$. The Fourier spectra are the same because the solutions in Figs. 3(a) and 4(a) are the same except for a constant shift. (b) Fourier spectra of the positive soliton solution (black, narrower spectrum) that are plotted in Fig. 3(b) and of the negative soliton solution (red, wider spectrum) that are plotted in Fig. 4(b) with $H = -0.00505$. (c) Fourier spectra of the positive (black) and negative (red) cnoidal waves that are plotted in Figs. 3(c) and 4(c) with $H = -0.03$. The Fourier spectra of the positive and negative solutions of Figs. 3(c) and 4(c) are the same. (d) Fourier spectra of the cnoidal waves that are plotted in Figs. 3(d) and 4(d) with $H = -0.1$.

2.4 Cnoidal waves in the case of non-zero damping ($\delta \neq 0$)

When $\delta \neq 0$, we can no longer find stationary solutions analytically. Instead, we find them, when they are stable, by numerically integrating Eq. (8) with a split-step algorithm [24] using the analytical solutions of Eq. (10) as the initial conditions. We find that the stationary solutions are no longer real functions, as was the case with zero damping. They are complex functions $\psi(x) = |\psi(x)| \exp[i\Phi(x)]$ with a periodic

phase modulation $\Phi(x)$. Figures 9 and 10 show a comparison between the stationary analytical solutions calculated for $\delta = 0$ and the numerical solutions calculated by integration of Eq. (8) for $\delta = 0.3$, 0.5, and 0.7 and for the initial conditions that are given by the analytical solutions of Eq. (10) with the following parameters: $h = 0.8$ and $H = 0.72$ ($P = 5$) for Fig. 9, and $h = 0.8$ and $H = 0.3$ ($P = 5.4$) for Fig. 10. In both figures, it is apparent that the stationary analytical solution used as the initial condition rapidly evolves into a stable stationary solution. While it is not a solution that can be expressed analytically in terms of Jacobi elliptic functions, the period, shape, and spectral properties remain close to those of the analytical solutions that are used as the initial conditions. We also note that the stationary analytical solution used in Fig. 9 is unstable, as shown in Fig. 6, while the numerical calculation shows that the final state that is reached with loss is stable. The introduction of loss enlarges the parameter range in which the cnoidal waves are stable. This behavior is expected because the loss acts as a filter that damps the high wavevector components of the field, thereby improving the solution's stability. The damping of the high wavenumber components can be seen in Figs. 9 and 10 by comparing the narrower Fourier spectra of the computational solutions with the slightly broader Fourier spectra of the analytical solutions.

To demonstrate that these cnoidal wave solutions are accessible from a broader set of initial conditions than the analytical cnoidal wave solutions at $\delta = 0$, we have solved Eq. (8) numerically using two impulsive functions as the initial conditions. The first impulsive function is 10^5 at $x = 0$ and 0 everywhere else. The second impulsive function is 10^{-5} at $x = 0$ and 0 everywhere else. In Fig. 11 we show an accessibility chart in the (h,δ) plane for $P = 5$. If both initial conditions lead to unstable chaotic behavior, we plot a diamond. If both initial conditions lead to breathers that are periodic in t as well as in x, we plot a dot. If both solutions are plane waves, we plot a triangle. If the larger impulsive function leads to a breather and the smaller

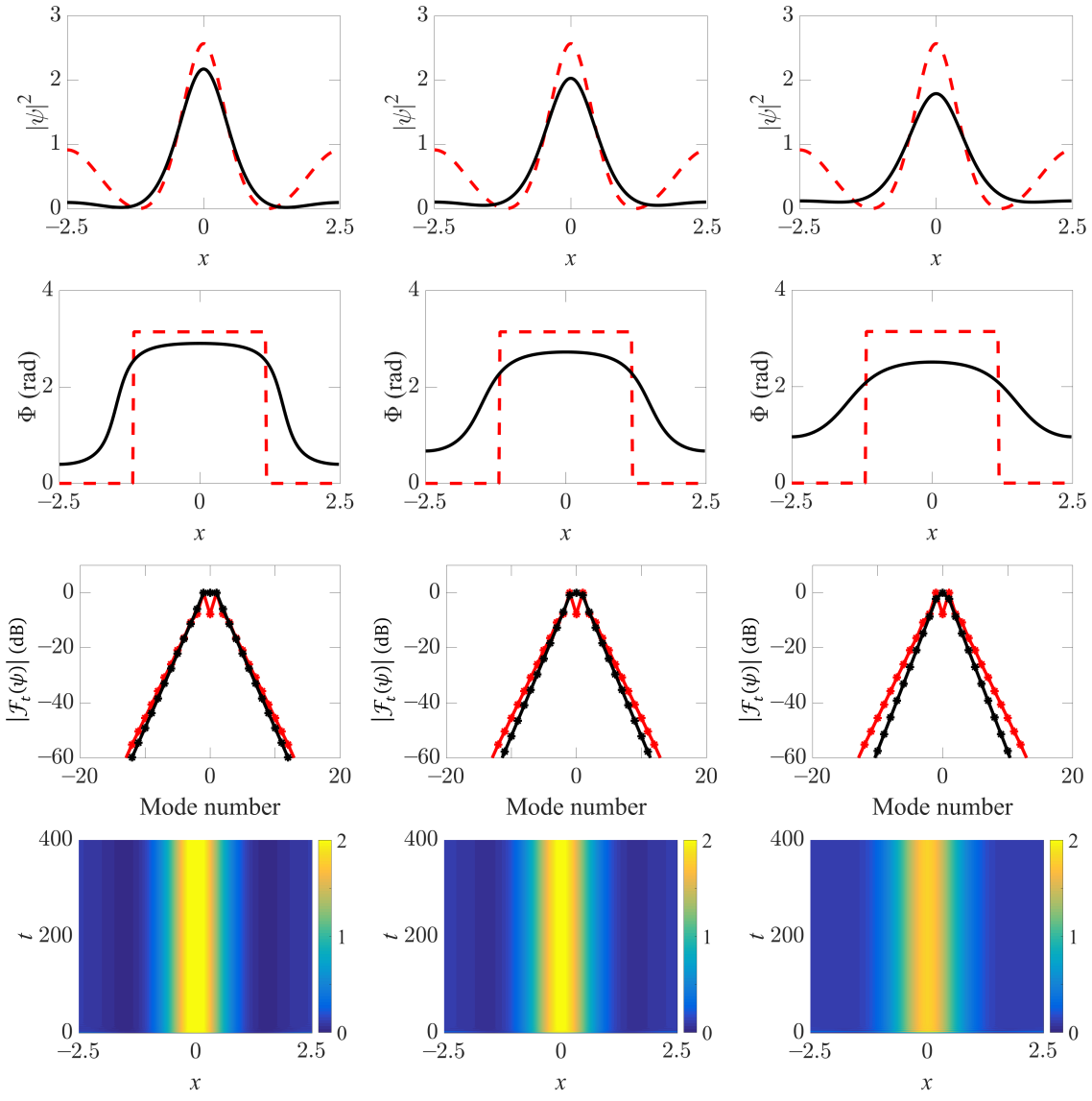

Figure 9: First row: The stationary analytical solutions (red dashed line) calculated for $H = 0.72$ and $h = 0.8$ ($P = 5$) and used as initial conditions for the numerical integration are compared to the computational solutions (black solid line) at $t = 400$ for $\delta = 0.3$, 0.5, and 0.7 respectively. At this time, the solution has converged to its stationary value. Second row: The phases of the analytical (red dashed line) and computational (black solid line) solutions are compared. Third row: Fourier spectra of the analytical (red) and computational (black) solutions. Fourth row: Spatio-temporal evolution of the numerical solutions.

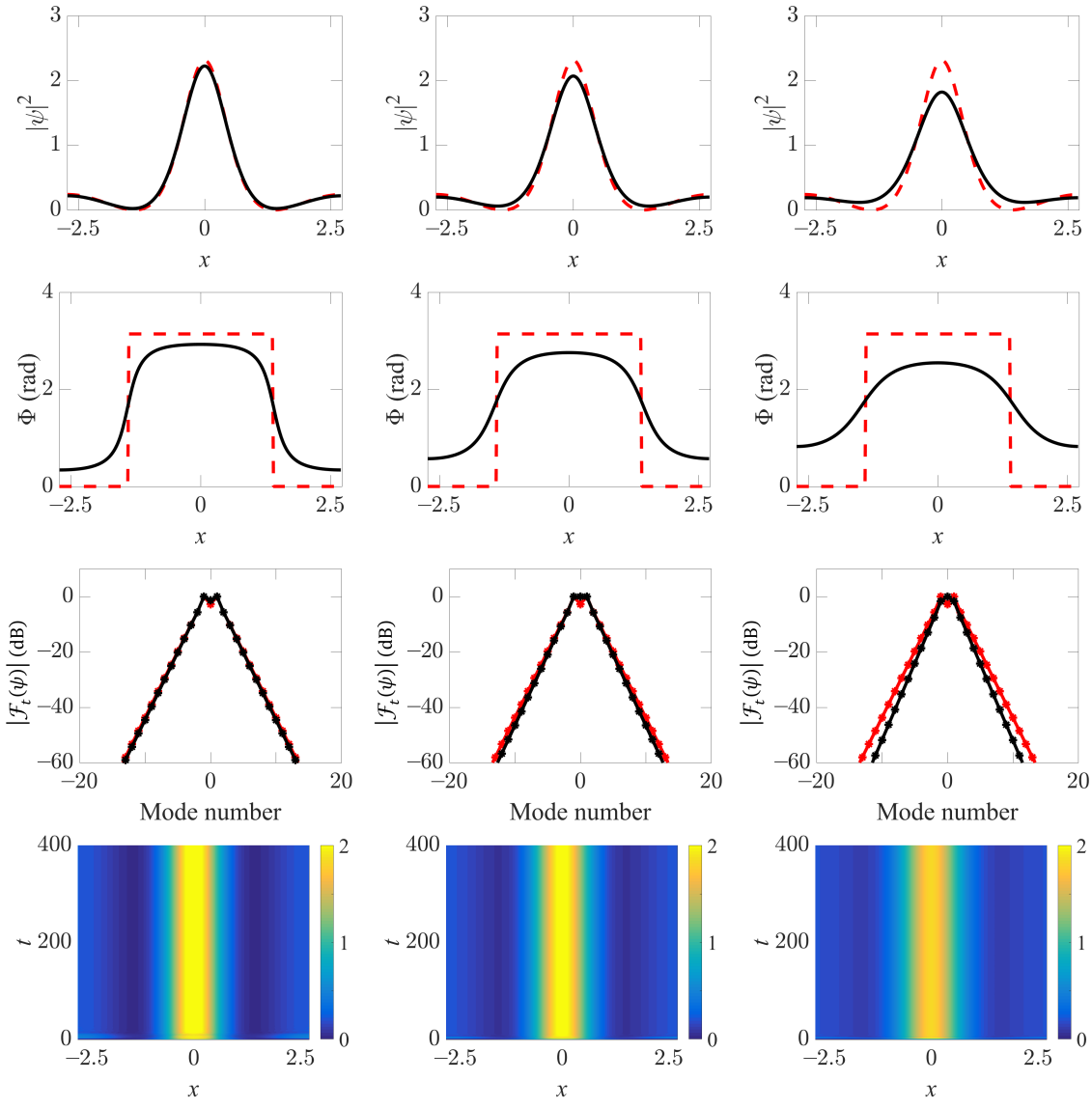

Figure 10: Same as in Fig. 9 except that here $h = 0.8$ and $H = 0.3$ ($P = 5.4$).

impulsive function leads to a plane wave, we plot an inverted triangle. Finally, if both initial conditions lead to a cnoidal wave, we plot a square. We see that there is a broad range of parameters from which the cnoidal waves are accessible from impulsive initial conditions. We also note that the parameter range in which stable cnoidal waves exist is significantly larger, but, as δ decreases, the stable solutions no longer can be accessed from impulsive initial conditions. In Fig. 12, we show four typical examples of the spatio-temporal evolution of the field intensity with the low amplitude impulsive function as the initial condition.

We now present an example to show how the non-dimensional parameters are related to the physical parameters of a microresonator. We consider a microresonator made of magnesium fluoride (MgF_2) with radius $R = 0.1$ cm, and with linear and nonlinear refractive indices $n_0 = 1.38$ and $n_2 = 0.9 \times 10^{-16}$ cm^2/W at the wavelength $\lambda_0 = 1.5$ μm [11]. The group velocity dispersion parameter is $\beta_{2\Sigma} = -2.8 \times$

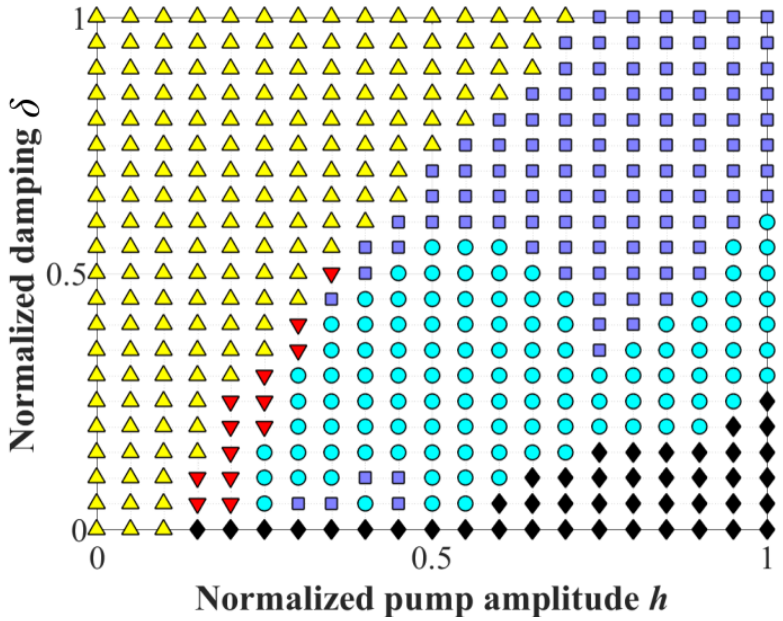

Figure 11: Accessibility chart for period $P = 5$ in the (h,δ) plane. Purple squares are stable cnoidal waves; Yellow upward triangles are cw waves; Red downward triangles are bistable solutions; Cyan circles are breathers; Black diamonds are chaotic solutions.

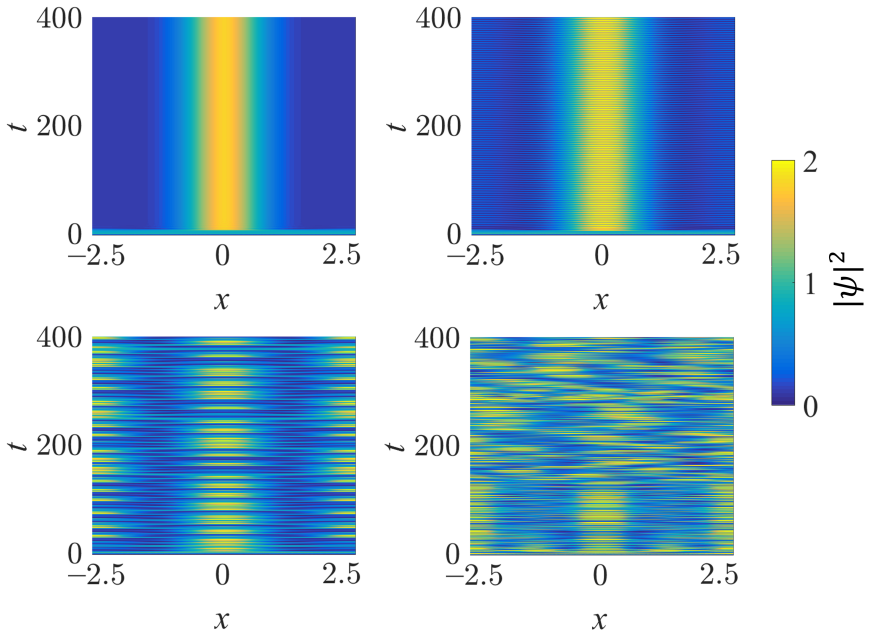

Figure 12: Spatio-temporal evolution of the field intensity for different values of δ and h corresponding to the points contained in the accessibility chart of Fig. 11. In this case, the initial condition is the small amplitude (10^{-5}) impulsive function. We show four typical cases. (a) The impulsive function evolves to a stable cnoidal wave for $\delta = 0.7$ and $h = 0.8$. (b) The impulsive function evolves to a breather for $\delta = 0.4$ and $h = 0.6$. (c) The impulsive function generates temporal chaos for $\delta = 0.25$ and $h = 0.45$. (d) The impulsive function generates spatio-temporal chaos for $\delta = 0.05$ and $h = 0.75$.

10^{-5} ps^2. For a mode volume $V = 2 \times 10^{-7}$ cm^3 , we obtain the Kerr nonlinearity strength $\gamma_\Sigma = (2\pi R)^2 n_2 \omega_0/(cV) = 7.9 \times 10^{-6}$ W^{-1}. The round trip time τ_0 can be approximately calculated as $\tau_0 \simeq 2\pi R n_0/c$, which implies for the current choice of parameters $\tau_0 \simeq 29$ ps. For a detuning $(\omega_{\bar{m}} - \omega_\mathrm{p}) \simeq 2$ MHz, the normalized detuning is $\delta_0 = \tau_0(\omega_{\bar{m}} - \omega_\mathrm{p}) \simeq 5.8 \times 10^{-5}$. For a coupling parameter $T_c \simeq 4 \times 10^{-5}$ and an amplitude loss per round trip $a_\Sigma \simeq 2 \times 10^{-5}$, the normalized loss parameter is $\delta = (\delta_\Sigma + T_c/2)/\delta_0 \simeq 0.7$. For these values, we find that the fast time ξ in ps is related to the normalized fast time x as $\xi(\mathrm{ps}) \simeq 0.5x$, the slow time τ in μs is related to the normalized slow time t as $\tau(\mu\mathrm{s}) \simeq 0.5t$, and the external pump power P_0 in mW is related to the normalized field amplitude h as $P_0(\mathrm{mW}) \simeq 100h^2$. The cnoidal

wave described in the third column of Fig. 10 ($P = 5.4$, $h = 0.8$, $\delta = 0.7$) will have a period of 2.7 ps and, hence, we expect 10 or 11 periods will appear in the resonator round trip time of 29 ps for a pump level of approximately 60 mW. With 10 periods in the resonator, the comb lines are spaced 340 GHz apart. The amplitudes of the lines at $m = m_d \pm 1$ are down from the peakline at $m = m_d$ by 2 dB, and the amplitudes of the lines at $m = m_d \pm 2$ are down from the peak by 10 dB.

2.5 Conclusions

In conclusion, we have studied both analytically and computationally the family of cnoidal wave solutions to the LLE. We have shown computationally that these cnoidal waves can be stable and are accessible from a wide range of values of the external pump and of the damping. Hence, these cnoidal waves can be used for nonlinear frequency comb generation in cases in which solitons are difficult to generate and/or the microresonator losses are substantial and, hence, higher external power is necessary to sustain the comb generation. Moreover, their inherently coarse-tooth characteristic will be useful when limiting the number of comb lines and precisely controlling their amplitudes is required, as for example in the precise generation of new frequencies [27], quantum networking [28], or astrocombs [26]. In the work to be presented in the next sections, we used dynamical methods to investigate in greater detail the accessibility and stability of cnoidal wave solutions when loss is included.

3 Dissipative cnoidal waves and the soliton limit in microring resonators

3.1 Introduction

It has long been known that single solitons are a special limit of a more general family of stationary nonlinear waves that are almost universally referred to as cnoidal waves in the plasma and fluid physics communities [29–34]. When loss and gain can be neglected, many fluid, plasma, and optical systems can be described at lowest order by the nonlinear Schrödinger equation (NLSE). Examples in optics include light propagation in optical fibers [35], passively modelocked lasers [36], and microresonators [4,11,12]. In the NLSE approximation, solitons can be analytically expressed in terms of hyperbolic-secant functions [$\mathrm{sech}\,(x)$], while more generally cnoidal waves can be expressed in terms of Jacobi elliptic functions [$\mathrm{cn}\,(x)$, $\mathrm{sn}\,(x)$, $\mathrm{dn}\,(x)$] [10, 37]. When loss and gain are present—as is the case in all experimental fluid and optical systems—then exact analytical solutions to the equations that describe these systems almost never exist. Nonetheless, it is common to refer to pulse and periodic solutions as "solitons" and "cnoidal waves" respectively. In the past 15 years, it has become increasingly common to refer to real-world solitons as "dissipative solitons" [38], and by analogy it seems reasonable to refer to real-world stationary periodic solutions as "dissipative cnoidal waves."

The literature on cnoidal waves in fluids is extensive, but that is not the case in optics, except in the soliton limit. (See, however, [39–41] for theoretical discussions.) Solitons or cnoidal waves that are described at lowest order by the NLSE are created by a balance between nonlinearity and dispersion. The pulses in optical fiber propagation experiments are typically separated by many times their duration in order to avoid instabilities [42]. Even in experiments in optical fiber ring resonators [43] or passively modelocked lasers [44] with many pulses in the cavity, it is useful to model

the pulses as a periodic train of weakly interacting solitons, rather than as a special limit of cnoidal waves. However, the small dimensions of microresonators make it easier to observe more general cnoidal waves than is possible in other optical systems, and they have frequently been observed [5, 14, 16, 17, 45–48], although often remarked upon only as a stepping stone on the path to single solitons [5, 14, 45, 46].

In recent years, a large experimental effort has focused on obtaining broadband microresonator combs using single solitons, and this effort has achieved remarkable experimental successes, including the demonstration of octave-spanning combs [49, 50], a $2f$-$3f$ self-referenced comb [51], and an optical frequency synthesizer [52]. However, these combs cannot be obtained in a straightforward way. In contrast to many modelocked lasers, the microresonators do not "self-start," i.e., when the microresonator is turned on, single solitons do not simply appear. Approaches to generate single solitons include pump tuning, thermal control, and engineered spatial mode interactions [53–56]. However, there is often a random element in the generation of single solitons [55, 56], and the search for robust, deterministic paths to obtain broadband combs continues. Recent work indicates that is possible to generate single solitons deterministically by using trigger pulses [57], by using two pumps [22, 58–60], or by adding an additional continuous wave component [61], or by adding avoided crossings. either naturally [56] or through a second resonator [62]. However, these approaches make the system significantly more complex. Another drawback to the use of single bright solitons to generate combs is that they make inefficient use of the pump. Typically, less than 1% of the pump power is transferred to the comb [14].

In this chapter, we will show that more general cnoidal waves can potentially solve these problems. Cnoidal waves can be broadband, while at the same time they can be straightforwardly accessed and use the pump more efficiently. They are sufficiently easy to obtain that they have frequently been observed, although, as previously noted, they have often been passed over. Their robustness has, however,

been previously noted [16, 47], and narrowband combs have potential applications to optical communication systems [47].

An essential difficulty in studying the potential of cnoidal waves is that there is a large parameter space to explore. As previously noted, single solitons correspond to period-1 cnoidal waves in which the azimuthal repetition period of the light in the microresonator cavity is equal to the entire azimuthal period, so that there is only a single pulse in the cavity. By contrast, cnoidal waves can have any periodicity, and a period-N_{per} cnoidal wave has an optical amplitude that repeats N_{per} times in one azimuthal period. Moreover, the cnoidal waves with a given periodicity N_{per} can vary greatly from structures in which the light intensity is never close to zero to structures that are effectively a periodic train of solitons or a soliton crystal. Indeed, this variability is their great advantage. We will show that it is possible to continuously tune the microresonator parameters to effectively obtain a train of solitons without ever passing through a chaotic regime, as is required to obtain single solitons.

Given the size of the parameter space to be explored, more theoretical guidance is needed, and direct solution of the evolution equations is inadequate for reasons that we will discuss shortly.

To address this issue, we have adapted a unique set of computational tools that were previously developed to study lasers [63] and that allow us to rapidly determine where in the parameter space cnoidal wave solutions exist and to find their frequency spectra. These tools are based on dynamical systems theory [64, 65] and complement widely available theoretical tools that are based on direct solution of the evolution equations. The basic idea is that once a cnoidal wave solution of a given periodicity has been found, one varies parameters, finding the cnoidal wave solutions as parameters vary by solving a nonlinear root-finding problem, instead of solving the evolution equations. In parallel, one determines the stability of the solution by finding the eigenvalues of the linearized equations. Once a stability boundary is encountered, where

the cnoidal waves become unstable or cease to exist, we track the boundary [63]. This approach is computationally rapid. Moreover, it allows us to identify all the stable cnoidal wave solutions that exist for a given set of parameters, in contrast to standard evolutionary simulations that will typically only identify a single solution, depending randomly on the initial conditions that are used. This approach also allows us to find unstable as well as stable cnoidal waves. That is important because unstable cnoidal waves can persist for a long time, and this approach allows us to calculate that time scale. When the lifetime of an unstable cnoidal wave is long, standard evolutionary simulations can incorrectly conclude that it will be stable.

The basic ideas that we are using are old, dating back at least to Maxwell's study of the stability of Saturn's rings [64]. Soliton perturbation theory is based on these ideas, and they have been adapted by Haus [65] and others [66] to study passively modelocked lasers. They have been used by Matsko and Maleki [67] to study soliton timing jitter and by Godey et al. [18] to study the stability of continuous waves in microresonators. Barashenkov et al. [23, 68] have applied these ideas to the study of multiple soliton solutions of the driven-damped NLSE [69], which in the microresonator community is typically referred to as the Lugiato-Lefever equation (LLE) [70]. However, almost all this work is based on analytical approximations of the stationary solutions. (The work in [23, 68] is an exception.) In our approach, we calculate computationally-exact stationary solutions, which allows us to accurately study the solutions in any parameter regime. That is particularly important when studying cnoidal waves in the anomalous dispersion regime, which is the focus of this chapter. While analytical solutions exist for the cnoidal wave solutions of the LLE when damping is neglected [13], these solutions are disconnected from the stable cnoidal wave solutions in the anomalous dispersion regime except when the periodicity is small, as discussed in Sec. 3.4. As a consequence, the utility of a perturbation theory based on these analytical solutions appears likely to have limited value.

The microresonator community has developed a nomenclature that differs in some respects from the nomenclature in common use in the nonlinear wave community. The use of "Lugiato-Lefever equation" instead of "driven-damped nonlinear Schrödinger equation" is one example. The periodic solutions of the LLE have been referred to as "Turing rolls," "primary combs," and "soliton crystals," as well as "cnoidal waves" or "dissipative cnoidal waves." The choice "Turing roll" connects the cnoidal wave solutions with earlier work on pattern formation [71]; the choice "soliton crystal" emphasizes the particle-like nature of solitons and connects the periodic solutions to single soliton solutions. As noted previously, our choice of "cnoidal waves" connects these solutions to the large body of work on periodic solutions in fluids, plasmas, and nonlinear waves. At present, we use the term "cnoidal waves" for periodic waveforms in the microresonator that do not change shape as they propagate and whose periodicity matches the number of amplitude maxima. We use "single soliton" for the $N_{\rm per} = 1$ cnoidal wave that consists of a single pulse. We use "soliton crystal" or "perfect soliton crystal" for a cnoidal wave with $N_{\rm per} > 1$ that effectively consist of well-separated pulses with a low amplitude pedestal. These waveforms appear when $\alpha \gtrsim 41/30$. We use "Turing rolls" to denote waveforms with a large pedestal that appear when when $\alpha \lesssim 41/30$. We note that Turing rolls typically appear with periodicity $N_{\rm per} \gtrsim L/(2\pi)$, while soliton crystals typically appear with periodicity $N_{\rm per} \lesssim L/(2\pi)$. It should be emphasized that cnoidal waves do not include all stable waveforms. For example, soliton molecules and imperfect soliton crystals can be stable and are not cnoidal waves.

The remainder of this chapter is organized as follows: In Sec. 3.2, we discuss our dynamical approach. In Sec. 3.3, we present our results on the stability of the cnoidal wave solutions—showing where in the parameter space stable solutions exist. We discuss their accessibility and how to optimize their parameters, including their bandwidth. In Sec. 3.4, we discuss the single soliton solutions. Our approach sheds

new light on the difficulties in accessing them. Finally, Section 3.5 contains the conclusions.

The work that is presented in this chapter has been published in Ref. [72].

3.2 Dynamical Methods

The standard evolutionary methods for solving the LLE are typically based on the split-step method and its variants [35]. We use a variant that we recently demonstrated is significantly faster computationally than most other variants when large loss and gain are present. In a standard evolutionary simulation, one starts from an initial condition, and one steps the LLE forward in time, sometimes allowing the equation's parameters to also change as a function of time. When a stationary solution is observed at the end of the simulation, one has learned where in the parameter space that particular stationary solution can be accessed, starting from the initial conditions and along the path in the parameter space that were used in the simulation. By contrast, dynamical methods for solving the LLE reveal where in the parameter space the stable solutions exist, but do not reveal how to access them. The dynamical methods function much like an x-ray machine that tells a surgeon where a bone is broken, but not how best to repair it. Hence, the evolutionary and dynamical methods are complementary.

While evolutionary methods are widely used in the microresonator community, dynamical methods are not. Our implementation is an adaptation of computational methods that were developed to study passively modelocked lasers [63]. Our starting point is a cnoidal wave solution that we find using evolutionary methods with equation parameters for which the solution is highly stable. This solution is stationary and satisfies Eq. (6) with its time derivative set equal to zero,

$$0 = i\frac{\partial^2 \psi}{\partial x^2} + i|\psi|^2\psi - (i\alpha + 1)\,\psi + F. \tag{36}$$

We now solve Eq. (36), while allowing F or α to vary, which becomes a nonlinear root-finding problem. We use the Levenberg-Marquart algorithm [73], which is a variant of the well-known Newton's method.

In parallel with solving Eq. (36) to find the cnoidal wave solutions, we determine their stability. We write

$$\psi\left(x,t\right)=\psi_0\left(x\right)+\Delta\psi\left(x,t\right),\qquad\bar{\psi}(x,t)=\psi_0^*(x)+\Delta\bar{\psi}(x,t),\tag{37}$$

where $\Delta\psi$ and $\Delta\bar{\psi}$ are small perturbations of the cnoidal wave solution $\psi_0(x)$ and its complex conjugate $\psi_0^*(x)$. The perturbations $\Delta\psi$ and $\Delta\bar{\psi}$ obey the linearized equation

$$\frac{\partial\Delta\boldsymbol{\Psi}}{\partial t}=\boldsymbol{\mathcal{L}}\Delta\boldsymbol{\Psi},\tag{38}$$

where

$$\Delta\boldsymbol{\Psi}=\begin{bmatrix}\Delta\psi\\ \Delta\bar{\psi}\end{bmatrix}\tag{39}$$

and

$$\boldsymbol{\mathcal{L}}=\begin{bmatrix}i\partial^2/\partial x^2+2i|\psi_0|^2-i\alpha-1 & i\psi_0^2\\ -i\psi_0^{*2} & -i\partial^2/\partial x^2-2i|\psi_0|^2+i\alpha-1\end{bmatrix}.\tag{40}$$

We convert Eq. (38) into an eigenvalue equation, $(\boldsymbol{\mathcal{L}}-\lambda\boldsymbol{\mathcal{I}})\Delta\boldsymbol{\Psi}=0$, where $\boldsymbol{\mathcal{I}}$ is the identity operator, and we discretize this equation. We then proceed to computationally find the set of all eigenvalues $\{\lambda_j\}$ of this equation. There is always one eigenvalue located at zero, which is due to the translational invariance of Eq. (6) and is immovable. Other than that, all eigenvalues of a stable cnoidal wave solution satisfy $\mathrm{Re}(\lambda_j)<0$, so that any perturbation except a translation will decay exponentially. All the eigenvalues are real or come in complex conjugate pairs. As we allow F or α to vary, we eventually encounter a stability boundary at which one of three things happen: (1) a single real eigenvalue becomes equal to zero, and the cnoidal wave

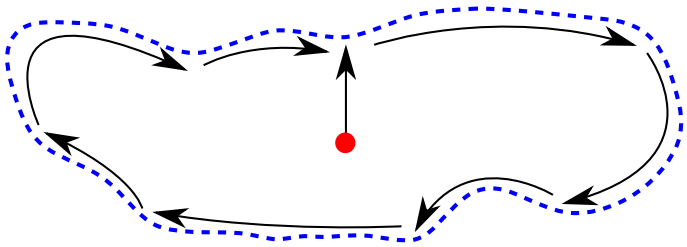

Figure 13: A schematic illustration of the boundary-tracking algorithm. The blue-dashed line indicates the boundary of the stable region. The red circle is the starting point. We obtain the complete stability boundary numerically by moving along the boundary, while tracking its location, as shown with the blue arrows.

solution ceases to exist; (2) one or more real eigenvalues pass through zero, and an unstable cnoidal wave solution continues to exist; or (3) the real parts of a complex conjugate pair of eigenvalues become equal to zero, and an unstable cnoidal wave continues to exist. Once a stability boundary is encountered, we track its location, as described in detail by Wang et al. [63] and as shown schematically in Fig. 13. As we track the boundary, we find that transitions occur among these three cases.

The ultimate fate of the system when the parameters pass through a stability boundary must be determined by solving the evolution equations using evolutionary methods. We have found that case (1) leads to a transition from a cnoidal wave solution to a continuous wave solution, case (2) leads to a transition to another cnoidal wave solution, and case (3) leads to a transition to a breather or chaos. These three cases are referred to in the mathematics literature as saddle-node, transcritical, and Hopf bifurcations, respectively [74, 75]. In the mathematics literature, the set of eigenvalues $\{\lambda_j\}$ are referred to as the "spectrum" of the operator $\boldsymbol{\mathcal{L}}$ [76, 77]. Here, we refer to the $\{\lambda_j\}$ as the "dynamical spectrum" in order to avoid confusion with the frequency spectrum. The dynamical spectrum of the LLE has a large amount of symmetry. It is symmetric about the real λ-axis, since if λ_j is an eigenvalue, then so is λ_j^*. Additionally, it is symmetric about the axis $\mathrm{Re}(\lambda) = -1$. We discuss some features of the dynamical spectrum in Sec. 3.3. While interesting, the details of this structure

are of little importance for this study since almost all the eigenvalues correspond to perturbations that rapidly damp out. Our focus is almost exclusively on the eigenvalues whose real parts become equal to zero as the microresonator parameters change.

Once the stable region of a cnoidal wave with a given periodicity has been found, its properties can be rapidly found throughout the region by solving Eq. (36) as α and F vary. We have used this technique to find the fraction of the pump power that goes into the cnoidal wave frequency comb, as well as the comb bandwidth. By solving the evolution equations, we have verified that any solution within the stability boundary can be experimentally accessed from any other solution within the boundary by changing the pump power and the detuning.

The dynamical methods that we are using have significant advantages over just using evolutionary methods to identify stable operating regions in the parameter space and paths through the parameter space to access them. First, directly solving the evolution equations for given initial conditions and system parameters can miss stable solutions that exist for those parameters. As shown schematically in Fig. 14, a stable waveform has a basin of attraction in the phase space of all possible waveforms. If the initial conditions are within this basin, then the evolution will eventually converge to this waveform, but, if it does not, then the evolution will not converge to this solution, and it is possible to miss it completely. This issue is particularly important for the cnoidal wave solutions where several different periodicities can be stable at the same point in the parameter space. Second, evolutionary methods yield ambiguous results near a stability boundary since the time for a perturbation to either decay or grow tends toward infinity. Examples of this ambiguity appear in Sec. 3.3. Third, the dynamical methods are computationally rapid, making it possible to determine the stability boundaries for all the cnoidal wave solutions within a broad parameter range. We have typically found that this approach is 3–5 orders of magnitude faster

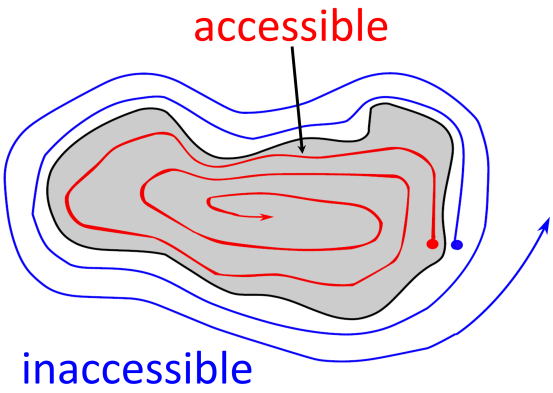

Figure 14: A schematic illustration of a basin of attraction in the phase space that consists of all possible waveforms. If the initial condition, shown as a red dot, starts inside the basin of attraction of a stationary waveform, shown in gray, then the solution will converge to the stationary solution. If the initial condition starts outside the basin, shown as a blue dot, then the solution evolves to another stationary solution or never becomes stationary.

than evolutionary methods, depending on how well one wants to resolve the stability boundary.

These same issues arise in any driven-damped system system in which stationary solutions such as single solitons, molecules, and periodic trains of solitons appear. Akhmediev et al. [78], for example, have discussed these issues in the context of the complex Ginzburg-Landau equation. This equation approximately describes a variety of optical and non-optical systems [38].

In most computational studies of the dynamics in microresonators, the instabilities are seeded by random numerical noise due to roundoff. This seeding implies a random noise amplitude on the order of 10^{-15} in modern-day 64-bit computers. This noise amplitude is many orders of magnitude lower than what is expected in an experimental system, which is largely set by environmental or "technical" noise [79, 80]. By contrast, the randomly varying amplitude due to quantum noise is in the range of 10^{-5}–10^{-4} for typical parameters. The growth of the amplitude of an unstable eigenmode is given by $A(t) = A_0 \exp(\lambda_R t)$. As long as λ_R^{-1} is small compared to the

time scale of the simulation by factors larger than about $\ln 10^{-15} \simeq -35$, then the small level of seeding from roundoff noise does not matter. When making a transition out of a region in the parameter range that is chaotic or where continuous waves are stable into a region where cnoidal waves are stable, the growth of the cnoidal waves is sufficiently rapid that it is not unreasonable to seed the growth from roundoff noise. We will see however that the time scale for instabilities to manifest themselves when making transitions from one cnoidal wave to another can be a sizable fraction of a second in real time, and these instabilities are computationally challenging to simulate. For that reason, we use a quantum noise seed. While the quantum noise power is lower than the technical noise power in microresonators by one to three orders of magnitude [80], it is large enough for instabilities to manifest themselves on physically realistic time scales.

3.3 Stability, Accessibility, and Optimization of Cnoidal Waves

In Fig. 15, we show the regions in the α-F (detuning vs. pump amplitude) plane, where the cnoidal waves are stable for different periodicities N_{per} in the range $-2 < \alpha < 6$ and for the normalized mode circumference $L = 10$, 25, and 50. For clarity, we only show some of the stable regions. However, we have found all the stable regions in the parameter range that we show. When $L \to \infty$, we find that N_{per}/L tends to a constant for a fixed value of α and F, as we show in Fig. 16. The value in the limit $L \to \infty$ is calculated using an approach like that of Godey et al. [18]. As a consequence, the three-dimensional parameter space in which all solutions of the LLE exist effectively reduces to a two-dimensional parameter space when $L \geq 50$.

In Fig. 15, we see that the region where cnoidal waves are stable form a U-shaped belt, shown as the red-dashed curves, in the α-F plane. Below this belt, only continuous waves (flat solutions) are stable and are always obtained. Above this belt, there are no stationary solutions; only breathers or chaotic solutions are obtained,

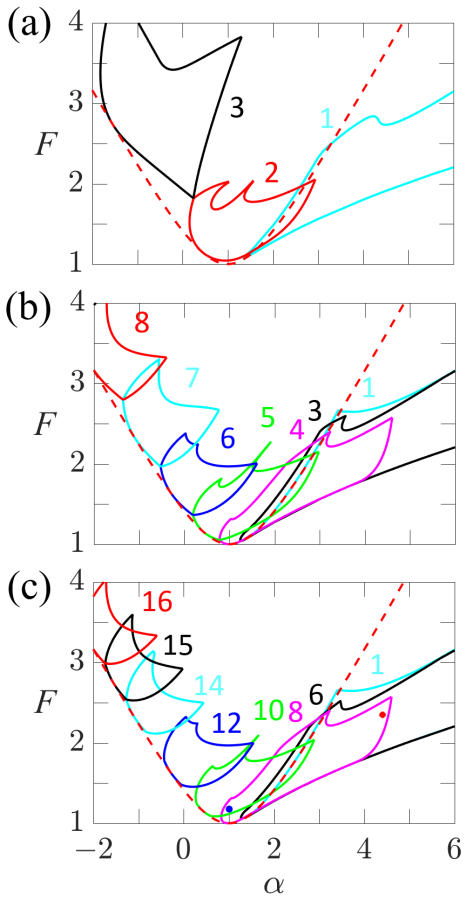

Figure 15: Stable regions of the cnoidal waves for (a) $L = 10$, (b) $L = 25$, and (c) $L = 50$. We show a selection of the stable regions, labeled with N_{per}. The red-dashed curves show the limit below which continuous waves are stable.

depending on the parameters. An analytical expression for this curve is derived in [18] and is given by

$$F = \sqrt{1 + (\alpha - 1)^2}. \tag{41}$$

An important transition occurs at $\alpha = 41/30$. Below this value of α, stable continuous waves and cnoidal waves do not both exist at the same parameter values. Hence, cnoidal waves can be easily accessed by simply raising the pump power. Above this value of α, stable cnoidal waves and continuous waves can both exist at the same parameter values. In particular, continuous waves are stable whenever single solitons

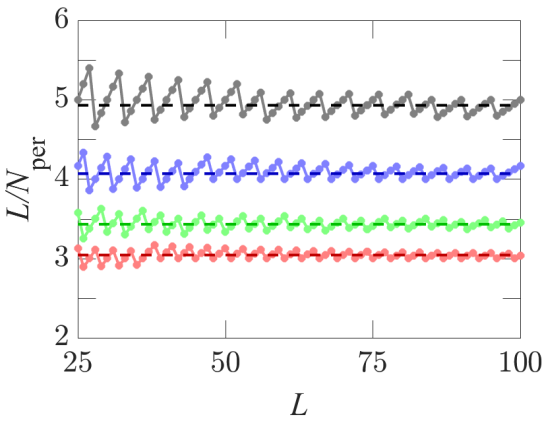

Figure 16: L/N_{per} vs. L for three values of (α, F): $\alpha = -2$, $F = 3.5$ (red); $\alpha = -1$, $F = 2.6$ (green); $\alpha = 0$, $F = 1.7$ (blue); $\alpha = 1$, $F = 1.2$ (black). Dashed lines show the asymptotic values in the limit $L \to \infty$. We obtained the stationary solution by using an evolutionary approach with a small random initial seed.

are stable. Hence, single solitons cannot be accessed by simply raising the pump power. Additionally, the stable region for single solitons overlaps almost completely the stable region for several higher-periodicity cnoidal waves when $L \geq 25$. The overlap of the stable region for single solitons with other stationary solutions explains in part why they are difficult to access.

In Fig. 17, we show the optical waveform, its frequency spectrum, and its dynamical spectrum for the $N_{\mathrm{per}} = 8$ solution with $L = 50$, $\alpha = 4.4$, and $F = 2.3$, corresponding to the red dot in Fig. 15(c). Figure 17(a) shows the stationary waveform's intensity, $|\psi(x)|^2$. Figure 17(b) shows P_n, defined as $P_n = |\tilde{\psi}_n|^2/|\tilde{\psi}_0|^2$, where $\tilde{\psi}_n = (1/L)\int_{-L/2}^{L/2} \psi(x) \exp(-i2\pi n N_{\mathrm{per}} x/L)\, dx$. Each comb line is spaced eight times the FSR apart. This $N_{\mathrm{per}} = 8$ cnoidal wave is effectively a set of eight periodically-spaced solitons—a periodic train of solitons or a soliton crystal—that is stablized by sitting on a small pedestal. The power P_n of the comb lines falls off exponentially from the central line. This clean, exponential falloff is characteristic of all cnoidal waves and distinguishes them from a random assortment of solitons or other pulses.

In Fig. 17(c), we show the dynamical spectrum of the waveform, and in Fig. 17(d),

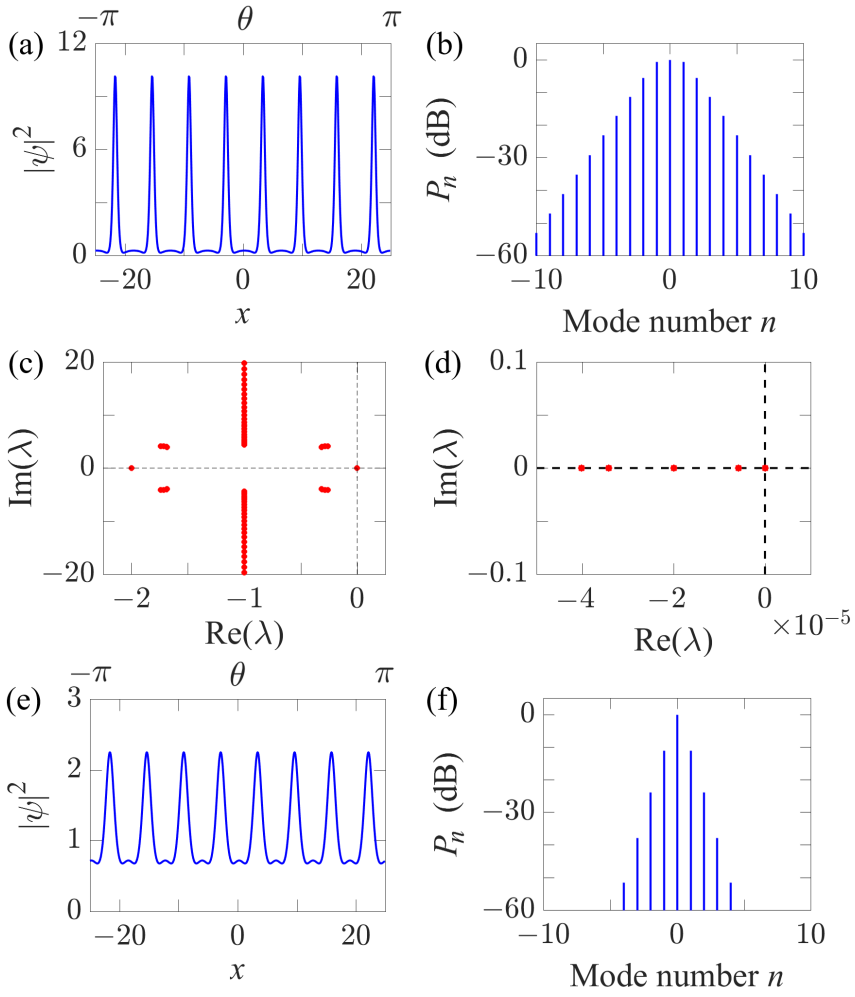

Figure 17: (a) Waveform, (b) frequency spectrum, and (c) dynamical spectrum with $N_{\rm per} = 8$, $L = 50$, $\alpha = 4.4$, and $F = 2.3$. (d) Expanded view of the dashed rectangular region near $\lambda = (0, 0)$ in (c). (e) Waveform and (f) frequency spectrum with $\alpha = 1$ and $F = 1.15$. Figs. 5(b) and (c) are modified from Fig. 2 of [81].

we show an expanded view of a small region near $\lambda = (0, 0)$. The dynamical spectrum has a fourfold symmetry about the real axis and the axis $\mathrm{Re}(\lambda) = -1$. There is always an eigenvalue at $\lambda = (0, 0)$, corresponding to azimuthal invariance of the solution and hence there is an eigenvalue at $\lambda = (-2, 0)$. Except for these two points, we have found that all the eigenvalues on the real axis are degenerate. We see that a group of real eigenvalues cluster near zero. These eigenvalues correspond roughly to modes that shift the amplitudes and phases of the pulses or solitons that make up the cnoidal

wave, while eigenvalues along the axis $\mathrm{Re}(\lambda) = -1$ correspond roughly to modes that perturb the pedestal. However, most of these features are of little relevance for this study. Our focus is almost entirely on eigenvalues that reach the imaginary axis as α and F change, implying that the stationary solution either becomes unstable or disappears.

In addition to higher periodicity cnoidal waves, imperfect soliton crystals in which a soliton is shifted or missing altogether have been observed in conjunction with avoided crossing [56]. These can also interfere with single soliton formation.

In Figs. 17(e) and 17(f), we show the optical waveform and its frequency spectrum for $\alpha = 1$ and $F = 1.15$, corresponding to the blue dot in Fig. 15(c). In this case, the $N_{\mathrm{per}} = 8$ cnoidal wave appears to be a modulated continuous wave, rather than a periodic train of solitons. Starting with this F and α and continuously varying the parameters to $\alpha = 4.4$ and $F = 2.3$ makes it possible to lock in place the periodic soliton train in Fig. 17(a).

In Fig. 18, we show examples of the transitions that occur when a stability boundary is crossed, starting in the region where the $N_{\mathrm{per}} = 8$ solutions are stable. In Fig. 18(a), we show the stable regions for $N_{\mathrm{per}} = 8$ and $N_{\mathrm{per}} = 9$, as well as four trajectories in the parameter space. We show the transitions in the dynamical spectrum for all four trajectories, focusing on the eigenvalues that hit or cross the imaginary axis. For clarity, we have omitted other eigenvalues. We show the initial eigenvalues as red dots and the final eigenvalues as blue circles. We also show the stationary solution as a function of the variable that we are varying, α or F. In Figs. 18(b) and 18(c), we show the dynamical spectrum and the stationary pulse intensities for trajectory A, for which we start at $\alpha = 2$, $F = 1.29$ and decrease F to 1.27. Slightly below $F = 1.28$, a saddle-node bifurcation occurs, at which point the cnoidal wave solution and hence its dynamical spectrum cease to exist. In this case, the final point in the dynamical spectrum is at $\lambda = (0, 0)$. The solution evolves from a cnoidal wave

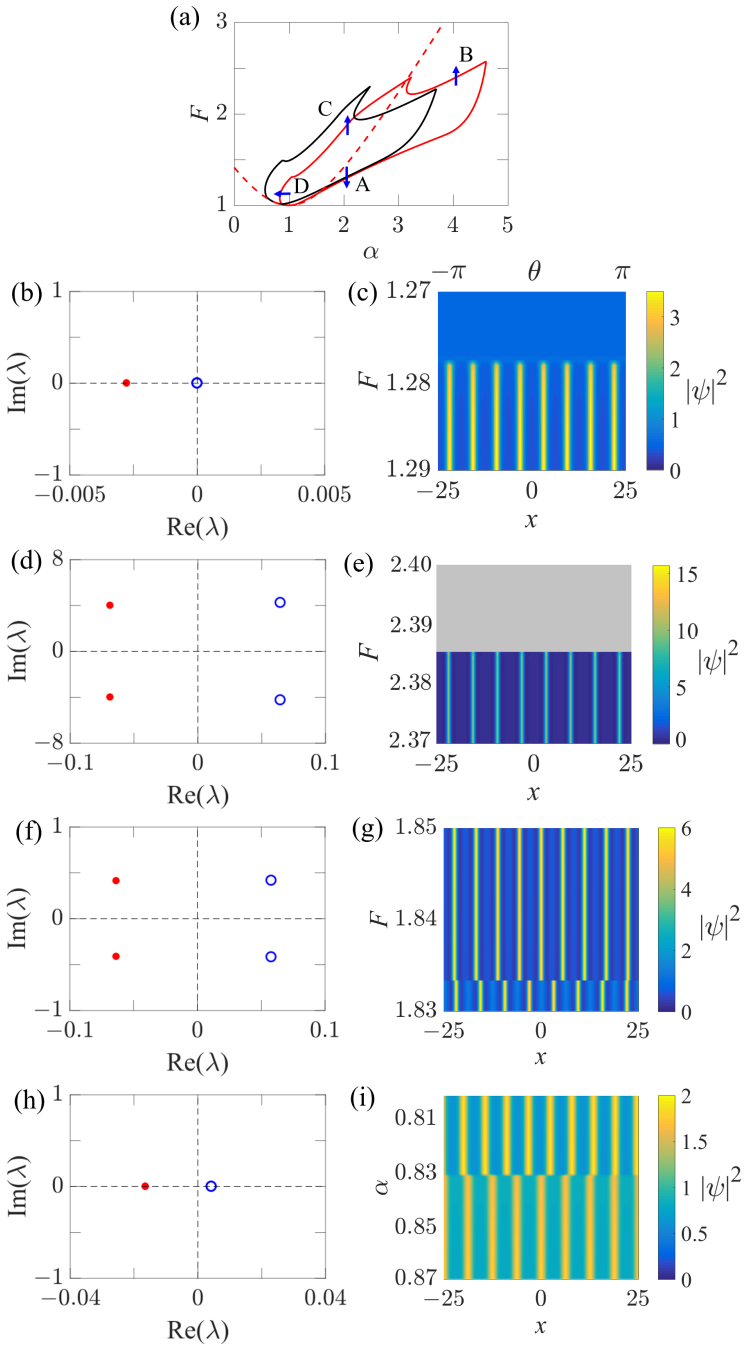

Figure 18: (a) Stable regions for the $N_{\text{per}} = 8$ (black curve) and $N_{\text{per}} = 9$ (red curve) cnoidal waves. The red-dashed curve plots the limit below which continuous waves are stable. A, B, C, and D indicate the four trajectories through the parameter space that we consider. Dynamical spectra and pulse intensities for: (b) and (c) trajectory A, (d) and (e) trajectory B, (f) and (g) trajectory C, and (h) and (i) trajectory D.

into a continuous wave. In Figs. 18(d) and 18(e), we show the dynamical spectrum and stationary pulse intensities for trajectory B, for which we start at $\alpha = 4$, $F = 2.3$, and we increase F. A Hopf bifurcation occurs; the cnoidal wave continues to exist, but it is unstable. It evolves into a breather solution, also referred to a secondary comb. In the Fig. 18(e), we show the region beyond the Hopf bifurcation in gray since no stationary solution exists. In Figs. 18(f) and 18(g), we show the dynamical spectrum and pulse intensities for trajectory C, for which we start at $\alpha = 2$, $F = 1.83$, and increase F. A Hopf bifurcation occurs, and the $N_{\text{per}} = 8$ cnoidal wave evolves into a stable $N_{\text{per}} = 9$ cnoidal wave. Finally, in Figs. 18(h) and 18(i), we show the dynamical spectrum and pulse intensities for trajectory D, for which we start at $\alpha = 0.85$, $F = 1.12$, and decrease α. A transcritical bifurcation occurs, and the stable $N_{\text{per}} = 8$ cnoidal wave evolves into a stable $N_{\text{per}} = 9$ cnoidal wave. However, the time scale on which this evolution occurs is noticeably longer than is the case for trajectories A, B, and C. That is a common feature of transcritical bifurcations and underscores the importance of using a realistic background noise level and sufficiently long integration times when using evolutionary methods.

Comparing Figs. 18(d) and 18(f) to Fig. 18(h), we see that λ_R, the maximum real value that appears in the dynamical spectrum, is about 25 times smaller for a transcritical bifurcation than it is after a Hopf bifurcation for a comparable excursion in the parameter space. As a consequence, the time scale for the instability to manifest itself is considerably longer for a transcritical bifurcation. In Fig. 19, we show the evolution as a function of normalized time and for physical time, using the parameters of Wang et al. [14], starting from the unstable stationary cnoidal wave solutions at the final points of Figs. 18(d), 18(f), and 18(h). As expected the time scale in Fig. 19(c), corresponding to Fig. 18(h) is about 25 times larger than the time scale in Figs. 19(a) and 19(b), corresponding to Figs. 18(d) and 18(f). The dynamical spectrum is particularly useful when studying transcritical bifurcations since without

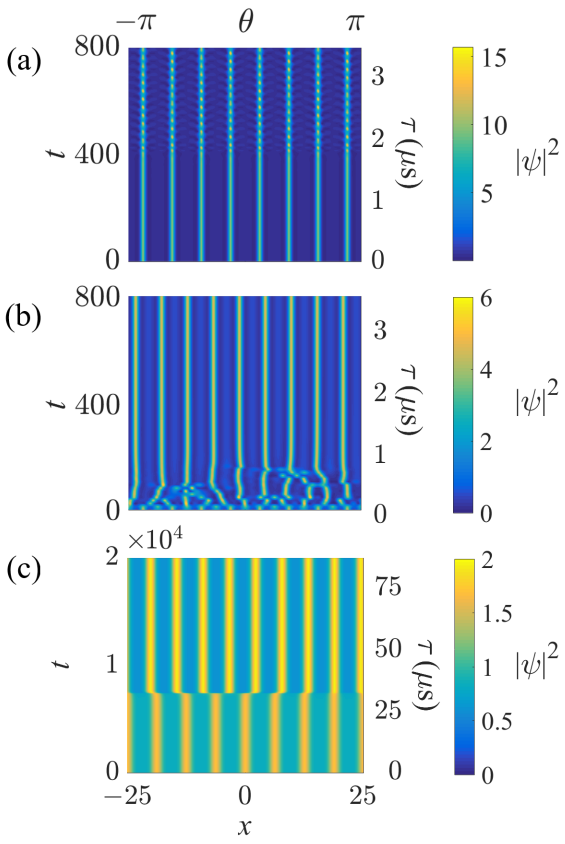

Figure 19: Evolution of pulse intensity corresponding to the final points in trajectories (a) B, (b) C, and (c) D in Fig. 18.

its guidance, one can easily integrate for too short a time to accurately assess the stability of the solution.

In Fig. 20, we compare the stability regions for $L = 50$ with evolutionary simulations for $L \simeq 46$. In Fig. 20(b), we show the number of peaks in the final solution after jumping from an initial cnoidal wave at $\alpha = 0$ and $F = 6.3$ to another point in the parameter space and remaining at that point for $\tau = 1.8$ μs [19]. While the results correspond roughly to the stability curves, differences should be noted. The dwell time is not always sufficient to determine the stability, and the location of the stability boundaries is ambiguous. Additionally, the passage time through the parameter space affects the final state. We will discuss this issue in more detail in Sec. 3.4. By moving along the trajectory in the phase space shown as the solid black curves

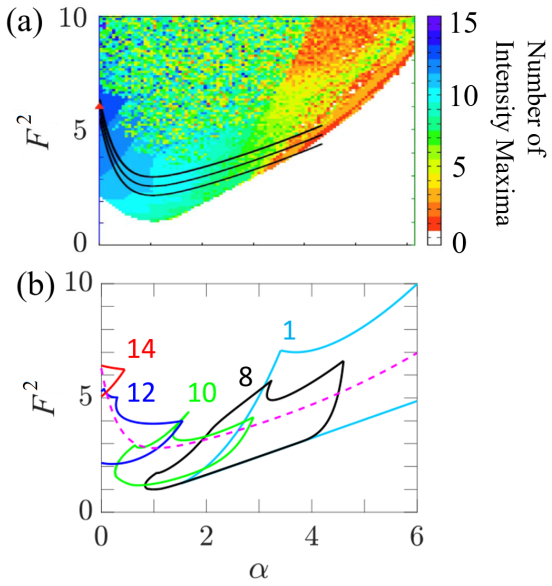

Figure 20: Comparison of the stability map for $L = 50$ with evolutionary simulations from which the stable regions can be inferred. Fig. 20(a) is modified from Fig. 14(a) in [19]. The color bar shows the number of intensity maxima in the plot. The solid curves in (a) and the red-dashed curve in (b) show trajectories through the parameter space that never pass through the chaotic region. This figure is modified from Fig. 1 in [81].

in Fig. 20(a) or the red-dashed curve in Fig. 20(b), it is possible to stay within the region in the parameter space where the cnoidal waves are stable and deterministically control, with occasional back-tracking, the periodicity of the cnoidal wave that is asymptotically obtained.

In Fig. 21, we show an optimization study for the $N_{\rm per} = 8$ cnoidal wave when $L = 50$. The point at $\alpha = 4.4$, $F = 2.3$, shown as a red dot in Figs. 15 and 21, corresponds to the frequency spectrum that we show in Fig. 17(b). The point at $F = 1.15$ and $\alpha = 1$ corresponds to the blue dot. The frequency spectrum always decreases exponentially away from the central peak. In Fig. 21(a), we show a contour plot of the rate of exponential decrease, P_n/P_{n+1} (dB) for $n \geq 3$. In Fig. 21(b), we show a contour plot for the ratio ρ of the power in the comb lines to the input pump power, $\rho = (1/F^2)\int_{-L/2}^{L/2} |\psi|^2 (dx/L)$. The corresponding change in the physical ratio

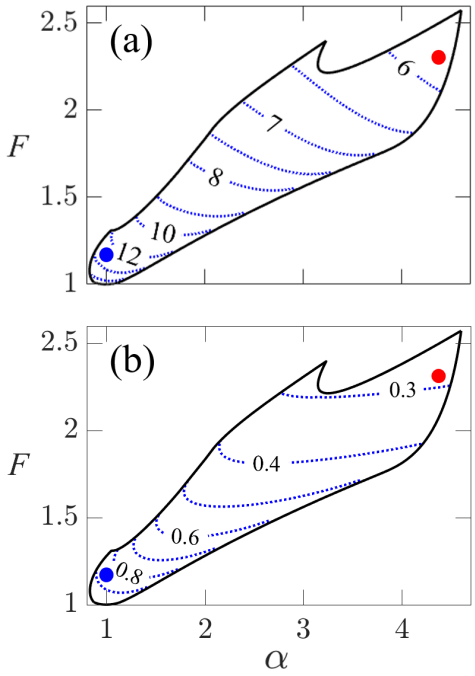

Figure 21: Contour plots of (a) the exponential decrease in the frequency spectrum P_n/P_{n+1} (db), $n > 3$, and (b) the ratio of the total power in the comb lines to the input pump power ρ for $N_{\rm per} = 8$. Fig. 21(a) is modified from Fig. 2(a) in [81].

of the power in the comb to the power in the pump is given by $\rho_{\rm phys} = (4/l^2)\,\rho$, which for the parameters of [14] and a single soliton is given by $\rho_{\rm phys} = 73.6\%$, which is close to the measured value at the drop port. There is a tradeoff between the efficiency with which the pump is used and the bandwidth of the frequency spectrum. At the point in the parameter space shown as a red dot, we find that $P_{n+1}/P_n(n > 3) < 6$ dB, while $\rho \simeq 0.3$. The comb lines in the frequency spectrum are separated by eight times the free spectral range (FSR). The lines at $n = \pm 6$ are down by 30 dB from the central line. For an FSR of 230 GHz, corresponding to the experiments in [14], the corresponding bandwidth is 21 THz, which is a large fraction of the operating frequency of 200 THz. This bandwidth is consistent with the bandwidth of single solitons in microresonators, whose bandwidth has not been enhanced through the use of dispersive radiation. It should be possible to apply techniques that have been

used to enhance the bandwidth of single solitons [50, 51] to cnoidal waves with larger periodicity. While the comb line spacing (1 THz) is large, it is consistent with the line spacing of the single soliton comb with large line spacing in the dual-microcomb experiment of [52].

To characterize the increase in efficiency of pump utilization as $N_{\rm per}$ increases, we computed ρ for periodicities $N_{\rm per} = 1$–8 with $\alpha = 4.4$ and $F = 2.3$. We found that ρ increases almost linearly, so that $\rho = 0.038$ when $N_{\rm per} = 1$ and $\rho = 0.287$ when $N_{\rm per} = 8$. This linear increase is not surprising since at these values of α and F, the cnoidal wave is effectively a periodic train of $N_{\rm per}$ solitons. Since the total power is nearly proportional to $N_{\rm per}$ and the comb lines are spaced $N_{\rm per}\times$ FSR apart, the power in each comb line is nearly proportional to $N_{\rm per}^2$. That can be important for applications where the power in a single comb line must be made large.

3.4 The Single Soliton Limit

Single solitons are a special limit of cnoidal waves for which $N_{\rm per} = 1$. They share many of the properties of cnoidal waves for which $N_{\rm per} > 1$. In particular, their frequency spectrum falls off exponentially away from the central peak. Single solitons are also a special limit of another class of nonlinear stationary waveforms, referred to as multi-bound solitons or soliton molecules [20, 68]. Except in special limits where they are single solitons or higher-periodicity cnoidal waves, soliton molecules are characterized by a complicated frequency spectrum.

Single solitons in microresonators are not easy to access and a large experimental effort has been aimed at finding ways to do that [5, 14, 16, 17, 45–47, 49–56]. Here, we focus on understanding the issues with accessing them from a dynamical perspective and we discuss the reasons that there is often a random element in their generation [55, 56]. We extend an earlier discussion that proposed a deterministic path through the parameter space to obtain single solitons [19], and we describe the critical role that

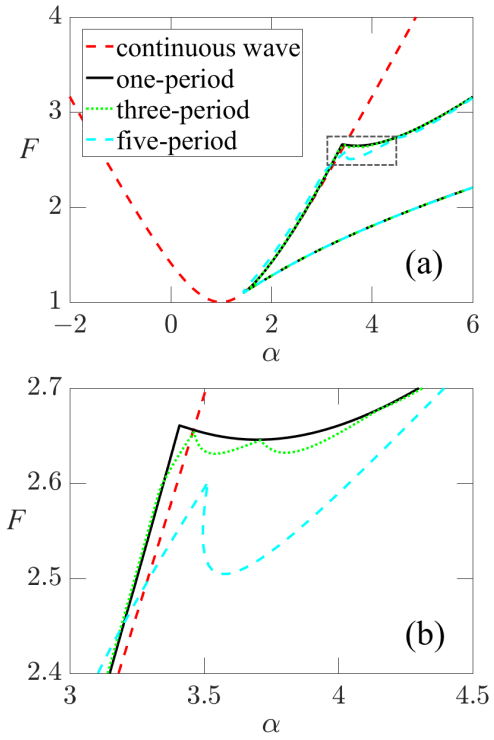

Figure 22: Stable regions for the $N_{\text{per}} = 1$ (black), $N_{\text{per}} = 3$ (green), and $N_{\text{per}} = 5$ (cyan) cnoidal waves. The $N_{\text{per}} = 1$ cnoidal wave is a single bright soliton. Continuous waves are stable below the red-dashed curve. The curves for $N_{\text{per}} = 1, 3$, and 5 almost completely overlap except in the black dashed rectangular region, of which an expanded view is shown in (b).

is played by the time scale on which one moves through that path.

In Fig. 22, we show the stable regions for the $N_{\text{per}} = 1$, 3, and 5 cnoidal waves when $L = 50$. For clarity, we do not show the regions of stability for $N_{\text{per}} = 2$, 4, or 6. While the stable region for single solitons ($N_{\text{per}} = 1$ cnoidal waves) is large, it almost entirely overlaps the regions of stability for several higher periodicity cnoidal waves in the parameter range that we show, as well as with continuous waves. Hence, it is not surprising that multiple solitons are often obtained in experiments rather than single solitons. However, the multiple solitons are usually randomly spaced, leading to a complicated frequency spectrum, which is usually undesirable in applications. While these states are unlikely to be stationary states, simulations indicate that they

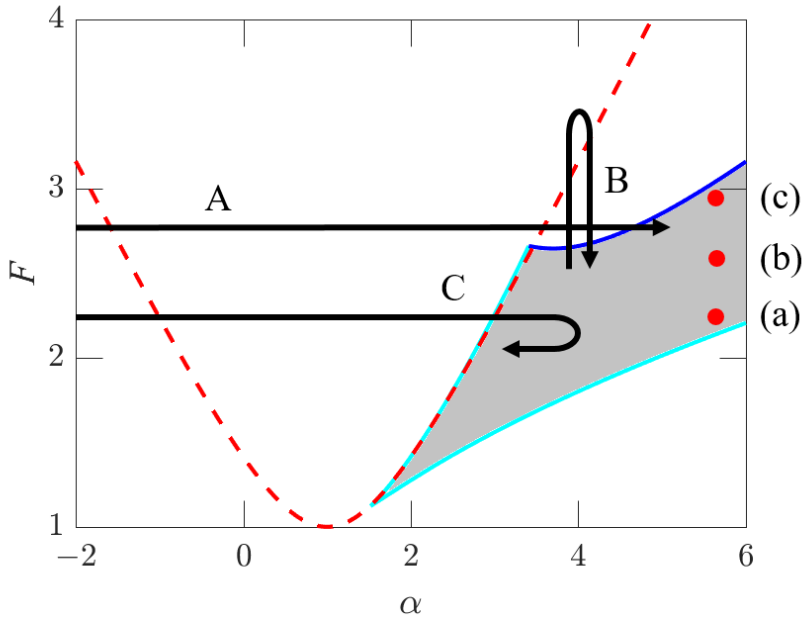

Figure 23: Schematic illustration of three trajectories through the parameter space to obtain single solitons. The gray region indicates where single solitons are stable, and continuous waves are stable below the red-dashed line.

can be long-lived, with lifetimes that far exceed standard simulation runs.

We can obtain insight into this behavior by examining how single solitons are generated. The most common path to obtain single solitons is to start in the blue-detuned region where either continuous waves or high-periodicity cnoidal waves are stable, at the left side of the U-shaped region shown in Fig. 15 [5, 14, 16, 45–47]. Solitons are then obtained by red detuning the pump laser through the chaotic region above the U-shaped region where cnoidal waves are stable into the region where single solitons, other low-periodicity cnoidal waves that are effectively a periodic train of solitons, and continuous waves are stable. This path is labeled A in Fig. 23. An alternative path, labeled B in Fig. 23, is to raise the pump power above the line where continuous waves are stable and then to lower the power until single or multiple solitons are stable [46, 49, 54]. A third alternative, labeled C in Fig. 23, is to tune backward after entering the region where single solitons are stable [55]. Since the

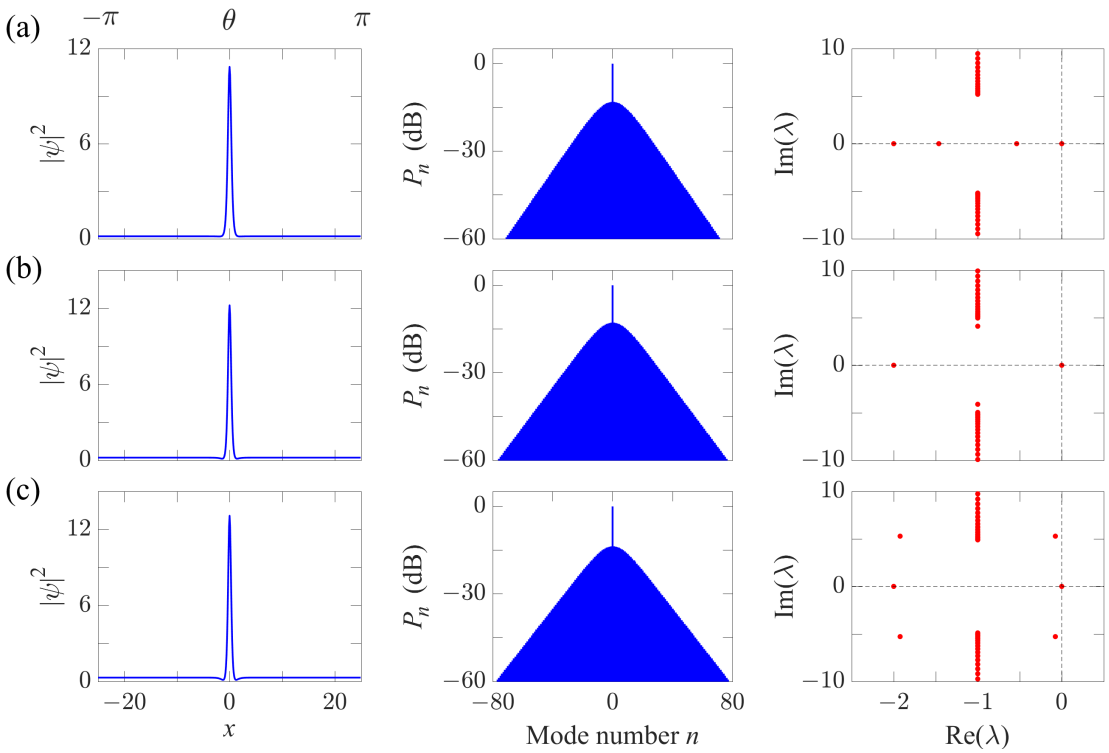

Figure 24: Waveforms (left), frequency spectra (middle), and the corresponding dynamical spectra (right) of single solitons for $\alpha = 5.5$ and (a) $F = 2.11$, (b) $F = 2.45$, and (c) $F = 2.9$ at $L = 50$.

soliton duration is inversely proportional to the detuning, backward tuning enhances the interaction between randomly created multiple solitons and thus hastens their collapse into a single soliton, a continuous wave, or another stationary state. In all these paths, the region where single solitons are stable is entered from the chaotic region, in which both temporal and spatial power fluctuations are comparable to the average power and are several orders of magnitude larger than the underlying noise level in the device [79]. As a consequence, the spacing of the solitons when they form will be random and both their number and spacing will vary from shot to shot. Their ultimate evolution will depend on the details of their formation. Since continuous waves and a number of higher-periodicity cnoidal waves are also stable, nothing in principle prevents their formation.

The stable region for single solitons that we show in Fig. 23 is bounded by curves

at which either a saddle-node bifurcation occurs (cyan curves) or a Hopf bifurcation occurs (blue curve). In Fig. 24, we show the dynamical spectra for the stable soliton for $L = 50$, $\alpha = 5.5$, and $F = 2.11$, 2.45, and 2.90, shown as the red dots in Fig. 23. We also show the corresponding waveforms and frequency spectra. It is evident that the dynamical spectra differ significantly from the dynamical spectrum that appears in soliton perturbation theory [82] or the Haus modelocking equation [65]. In that case, the only discrete eigenvalues correspond to amplitude, frequency, time, and phase shifts. There are also continuous eigenvalues that correspond to background radiation. In this case, near the value at which the Hopf bifurcation occurs ($F = 2.9$), the least-damped eigenvalues correspond to damped-periodic oscillations of the single soliton. Near the value at which the saddle-node bifurcation occurs ($F = 2.11$), the least-damped eigenvalue corresponds to a damped amplitude and phase modulation. The cluster of eigenvalues near $\lambda = (0, 0)$ that was visible in the case of the $N_{\mathrm{per}} = 8$, shown in Fig. 17, and which correspond to damped interactions between the solitons that make up the cnoidal wave, are not present.

As a consequence, we might expect single solitons to be more robust in the presence of large noise or environmental fluctuations. We have verified, doing a long simulation run for which $t = 10^8$, that the $N_{\mathrm{per}} = 8$ cnoidal wave illustrated in Fig. 17 remains stable. These simulations are computationally taxing, requiring many hours on a standard desktop computer. However, this normalized time t only corresponds to about 1 s of physical time for a resonator quality factor $Q = 1.67 \times 10^6$, corresponding to the parameters of [19]. Determining their nonlinear stability in the presence of noise fluctuations over the lifetime of an experiment remains to be done.

A promising approach to deterministically obtain low-periodicity, large-bandwidth cnoidal waves, including single solitons, is to avoid the chaotic region [19]. Rather than just changing the detuning or the power, it is advantageous to change both together so that the system moves along one of the paths shown as the black curves in

Fig. 20(a) or the red-dashed curve in Fig. 20(b). In this case, transcritical bifurcations occur along the trajectory through the parameter space when cnoidal waves become unstable. The time scale of these instabilities, which is typically milliseconds, is long compared to most simulations, although short compared to most experiments. It is possible to take advantage of this long time scale to deterministically create single solitons [19].

In Fig. 25, we show the the evolution when the system parameters are shifted from $\alpha = 0$ to $\alpha = 6$ along the red-dashed curve in Fig. 20(b) at different speeds and the system is then allowed to evolve to a stationary final state. We set $L = 50$ and use $Q = 2.7 \times 10^6$ to convert from normalized time to physical time, $t_{\rm phys}$. The expresssion for the red-dashed curve is Eq. (41). In Fig. 25(a), we show the evolution when the initial evolution from $\alpha = 0$ to $\alpha = 6$ occurs rapidly, analogous to the case considered in [19]. In this case, the parameters are initially fixed at $\alpha = 0$, $F = 6$ and remain there until $t = 100$ ($\tau = 0.46$ μs). By that time, a stable $N_{\rm per} = 13$ cnoidal wave has emerged. The detuning is then increased linearly up to $\alpha = 6$, arriving at $t = 250$ ($\tau = 1.15$ μs). Finally, we wait until $t = 600$ ($\tau = 2.76$ μs). The original $N_{\rm per} = 13$ cnoidal wave that forms at $\alpha = 0$ does not have time to evolve into anything else before the system arrives at $\alpha = 6$. Subsequently, the unstable waveform evolves into a single soliton. This behavior consistently occurs with different noise realizations. In Figs. 25(b) and 25(c), we show the evolution when the transition between $\alpha = 0$ and $\alpha = 6$ occurs between $t = 100$ and $t = 1.201 \times 10^5$ ($\tau = 0.55$ ms). We then allow the solution to evolve up to $t = 2 \times 10^6$ ($\tau = 9.2$ ms). In this case, the evolution is sufficiently slow for several transcritical bifurcations to take place as α increases. The $N_{\rm per} = 8$ cnoidal wave that appears at the end of the initial evolution is only weakly unstable, i.e., $\max(\lambda_R) \simeq 6.7 \times 10^{-5}$. The solution that we show ultimately collapses to a continuous wave at around 8 ms, as shown in Fig. 25(c). We have run this simulation with four other noise realizations. In all

cases, the solution collapses to continuous waves. The computational integration time is quite long in this case, although the physical time is less than a second. Again, the use of the dynamical approach to point to the presence of an instability was critical in integrating sufficiently long to detect it.

We find that the final state of the system depends on how quickly the system moves through the parameter space, as well as the trajectory.

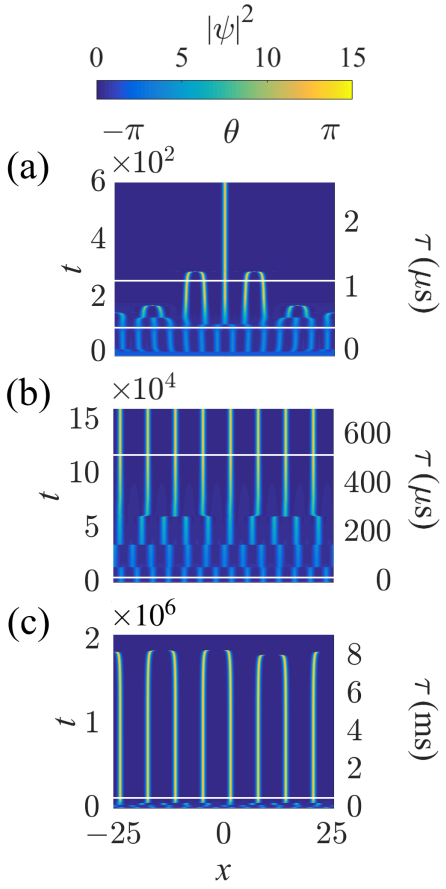

Figure 25: Evolution of the waveform when the system parameters move along the red-dashed curve in Fig. 20(a). (a) The lower white line corresponds to $t = 100$ and the upper white line corresponds to $t = 250$, inside of which the detuning shifts from $\alpha = 0$ to $\alpha = 6$. At the end of the evolution, a single soliton appears. (b) The lower white line corresponds to $t = 100$ and the upper white line corresponds to $t = 1.201 \times 10^5$, inside of which the detuning again shifts from $\alpha = 0$ to $\alpha = 6$. (c) The lower white line corresponds to $t = 1.201 \times 10^5$. At the end of the time, the solution has collapsed to a continuous wave.

3.5 Conclusion

Single solitons are a special case ($N_{\mathrm{per}} = 1$) of cnoidal waves. We have determined the parameter ranges within which different periodicities are stable by solving the Lugiato-Lefever equation for parameters that are relevant for microresonators. We have also described methods for accessing these different periodicities. We have demonstrated that cnoidal waves with $N_{\mathrm{per}} > 1$ can have a broad bandwidth, comparable to single solitons, while at the same time they are easier to access and use the pump more efficiently. In this limit, they are effectively a periodic train of solitons or a soliton crystal.

In order to determine the ranges of stable operation in the parameter space and to optimize the cnoidal wave parameters, we used a set of software algorithms that are based on dynamical systems theory. While the basic ideas are old, we are the only research group in optical sciences of which we are aware that has implemented them in software in a form that makes it possible to rapidly and accurately determine where in the experimentally-adjustable parameter space stable waveforms exist. As part of these algorithms, we calculate the dynamical spectrum, which is the set of eigenvalues for the linearized operator about a stationary waveform. In addition to its utility in determining the stability of the stationary waveform, the dynamical spectrum also allows us to calculate the time scale on which an instability will manifest itself.

We focus in particular on the $N_{\mathrm{per}} = 8$ cnoidal waves for a normalized mode circumference $L = 50$, which corresponds approximately to the experimental parameters of [19]. We describe the mechanisms by which the cnoidal wave can become unstable or cease to exist.

The cnoidal waves for a fixed device length occupy an approximately U-shaped band in the pump power-detuning parameter space. Below this band, only continuous waves are stable. Above this band, only breathers or chaotic solutions exist. For a normalized detuning $\alpha < 41/30$, cnoidal waves are easily accessed by simply raising

the pump power. That is the case for the $N_{\mathrm{per}} = 8$ cnoidal wave. Once a cnoidal wave has been accessed, its parameters can be changed by moving inside its stable region in the parameter space. Typically cnoidal waves with several different periodicities can exist for the same system parameters. We have found that they all have comparable bandwidths. In particular, that is the case for cnoidal waves that exist for the same set of parameters as single solitons.

The most common way to obtain single solitons is to start with negative detunings, where continuous waves or high-periodicity cnoidal waves exist. The system is then red-detuned through the high-periodicity cnoidal wave region into the chaotic region. After further red detuning, the system moves into the region where low-periodicity cnoidal waves, including single solitons, exist. This path through the chaotic region makes it possible for multiple solitons to appear, whose number and spacing vary randomly from shot to shot. Since the region where single solitons are stable nearly overlaps with the regions where continuous-waves and several other low-periodicity cnoidal waves exist, it is hard to deterministically ensure that only a single soliton will appear.

We have investigated an alternative approach in which the system moves through a U-shaped trajectory in the parameter space where cnoidal waves are stable. We showed that the stationary cnoidal wave that is obtained depends on the time scale at which the system moves along a trajectory through this space, as well as the trajectory itself.

All the theoretical work presented here is based on the Lugiato-Lefever equation. We have not discussed noise issues in any detail, and we have not discussed higher-order dispersion or thermal effects. It is reasonable to suppose that techniques that use dispersive waves to increase the bandwidth of single solitons would be useful for cnoidal waves, and could perhaps stabilize them against the effects of noise, in combination with acoustic effects, as is the case in some fiber lasers with multiple

pulses in the cavity [44].

It is already known that thermal effects have a profound effect on the region in the parameter space where single solitons are stable [50, 55, 83, 84]. Thermal effects can differ significantly depending on the material system, geometry, and operating temperature. For silicon-nitride microresonators operating at or near room temperature, thermal effects distort the U-shaped region where stable cnoidal waves exist, but do not change the basic results. Recently, Moille et al. [85] have studied microresonators at cryogenic temperatures where thermal effects can be almost eliminated, and our theoretical results apply directly. Regardless of the material system, geometry, and operating temperature, our results are a necessary starting point for further study.

4 Deterministic Access of Broadband Frequency Combs including Thermal Effects

4.1 Introduction

Broadband optical frequency combs in which all the frequency modes are coherently locked make it possible to measure frequency with great accuracy and have enabled a wide range of applications [86]. These include applications to basic science, astrophysics, environmental and chemical sensing, medicine, and military technology [87, 88]. However, frequency combs are usually produced using passively mode-locked lasers, which are often bulky and expensive. It was discovered in 2007 that it is possible to produce broadband frequency combs in microresonators [3, 89], which are μm-size or mm-size optical rings. This discovery opened up the prospect of compact, relatively inexpensive frequency combs and led to a worldwide effort to obtain an octave of bandwidth and lock the frequency combs [90]. Microresonator frequency combs are produced by a microresonator to which an optical waveguide carrying continuous-wave light is coupled. The light from this waveguide pumps a single resonant frequency mode inside the microresonator. This mode then parametrically pumps other microresonator modes [91, 92], ultimately creating a broadband comb [93, 94]. However, this comb is typically incoherent and corresponds to a randomly fluctuating optical amplitude inside the microresonator. The most common approach to generate a coherent comb is to either tune the pump frequency [5, 14, 16, 45–47] or the pump power [46, 49, 54] to generate a single (bright) soliton that circulates in the cavity, corresponding to a coherent comb. However, this process is not deterministic. Most of the time it does not produce a single soliton, and the process must be repeated multiple times until a single soliton is randomly obtained.

This approach has achieved notable successes in recent years. These have included the demonstration that an octave of bandwidth can be obtained [50], the demonstra-

tion of an on-chip optical frequency synthesizer [52], demonstration of microwave purification [95] and microwave synthesis [96], and applications to dual-comb spectroscopy [97] and lidar [98, 99]. However, this approach has significant drawbacks. As noted, the single soliton generation process is random. Indeed, recent work has demonstrated that when thermal effects can be neglected there is no path through the parameter space that can deterministically generate single solitons because continuous waves and multiple soliton solutions that are soliton crystals co-exist in the parameter space [72].

Another drawback of single solitons is that they use the pump inefficiently. Less than 1% of the pump power typically goes into the frequency comb [14]. Associated with this drawback is another; single solitons are thermally unstable unless the device temperature is carefully managed. When a single soliton is generated, the device cools, and the soliton can become unstable. To avoid this instability, a feedback control system is required, which adds to the system complexity [53]. There have been several recent proposals for the deterministic generation of solitons. In one approach, multiple pump frequencies are used to modulate the input pump amplitude [22, 100–102] or phase [58]. This approach has been demonstrated experimentally [60,103,104]. Another approach is to add an additional ring [62, 105, 106] or an additional mode interaction in the same ring [56]. All these approaches require significant additional hardware and seriously complicate the design of the frequency comb generator. In all of these approaches, careful management of the thermal instability is required.

Here, we describe a method for deterministic generation of a broadband frequency comb that overcomes the disadvantages of the current approaches to single soliton generation without requiring a significant increase in the hardware complexity. In general, our method creates a broadband frequency comb by generating a periodic array of solitons or a perfect soliton crystal rather than a single soliton. Soliton crystals have been the subject of increasing study in the past three years [13, 17,

72, 107–113] and have advantages over single solitons. First, soliton crystals use the pump N times more efficiently than a single soliton, where N is the number of solitons in the crystal, and the power in the frequency comb increases by a factor N. Second, the number of frequency comb lines is reduced by a factor N, so that the power in each comb line is multiplied by a factor N^2 [72]. By adiabatically following an appropriate path through the parameter space that consists of (frequency detuning)$\times$(pump amplitude), it is possible to first generate a narrowband cnoidal wave that corresponds to periodically-spaced peaks on top of a high pedestal. As the system parameters continue to change along the access path, the narrowband cnoidal wave continuously transforms into a broadband cnoidal wave that is effectively a stable, periodic array of solitons, i.e., a soliton crystal [72].

We previously described a deterministic approach for generating broadband cnoidal waves when thermal effects can be neglected. However, in practical systems, thermal effects are almost never negligible, although there are exceptions [85]. We will show that this approach must be modified when we take into account thermal effects, and the path through the parameter space becomes slightly more complicated. However, the basic approach remains the same.

This method for generating broadband frequency combs is thermally stable. Since the generation of the soliton crystal or single soliton is deterministic, we need merely move adiabatically along the deterministic path in the parameter space, i.e., move at a speed that is sufficiently slow to ensure that the system is in thermal equilibrium at each point in the parameter space.

The work that is presented in this chapter has been published in Ref. [114].

4.2 Basic Equations and System Parameters

The equation that describes the evolution of the light envelope in the microresonator is the modified Lugiato-Lefever equation (LLE) that may be written [55]

$$\begin{aligned} T_R\frac{\partial\Psi}{\partial\tau} &= -i\frac{\beta_2}{2}\frac{\partial^2\Psi}{\partial\theta^2} + i\gamma|\Psi|^2\Psi + \left\{-i\left[\omega_r\left(T\right)-\omega_0\right]T_R - \frac{l}{2}\right\}\Psi + i\sqrt{P_{\text{in}}}, \\ \frac{\partial\Delta T}{\partial\tau} &= \frac{\lambda}{2\pi}\int_{-\pi}^{\pi}|\Psi\left(\theta\right)|^2 d\theta - \kappa\Delta T, \end{aligned} \tag{42}$$

where Eq. (2) has been modified to take into account thermal effects. We have that σ in Eq. (2) is given by $\sigma = \left[\omega_r\left(T\right)-\omega_0\right]T_R$, where T is the temperature, ω_0 is the angular frequency of pump, $\omega_r\left(T\right)$ is the angular frequency of the resonator mode at the cavity temperature T, $\Delta T = T - T_0$ is temperature difference between the cavity temperature T and the ambient temperature T_0, λ is the thermal absorption coefficient, and κ is the thermal relaxation coefficient.

Equation (42) is valid for microresonators that are made using silicon nitride or other ceramic materials. Microresonators that are made using crystalline materials like CaF have a more complicated thermal behavior [115].

Thermal effects are often neglected in theoretical studies of microresonators. While they do not impact the existence of stable cnoidal waves solutions, they do significantly affect the location of the stable regions in the (frequency detuning)×(pump amplitude) parameter space. In particular, they cause the stable region for single solitons to become separate from the stable regions for soliton crystals [114].

After normalization, Eq. (42) becomes

$$\begin{aligned} \frac{\partial\psi}{\partial t} &= i\frac{\partial^2\psi}{\partial x^2} + i|\psi|^2\psi - \left[1 + i\left(\alpha+\Phi\right)\right]\psi + F, \\ \frac{\partial\Phi}{\partial t} &= AP - B\Phi, \end{aligned} \tag{43}$$

where $\psi = \left(2\gamma/l\right)^{1/2}\Psi$ is the normalized slowly varying envelope of the optical am-

plitude, $t = [l/(2T_R)]\,\tau$ is the normalized time, $x = (l/|\beta_2|)^{1/2}\,\theta$ is the normalized azimuthal coordinate. We have $-L/2 < x < L/2$, where $L = 2\pi\,(l/|\beta_2|)^{1/2}$ is the longitudinal mode circumference, normalized to the dispersive scale length [72]. The quantity $\alpha = 2\,[\omega_r\,(T_0) - \omega_0]\,T_R/l$ is the normalized angular frequency detuning between the cavity resonance and the pump laser. The physical frequency detuning $f_{\rm det}$ is given by $f_{\rm det} = [\omega_r\,(T_0) - \omega_0]\,/\,(2\pi) = [l/(4\pi T_R)]\,\alpha$. The normalized thermal detuning is given by $\Phi = 2\,[\omega_r\,(T) - \omega_r\,(T_0)]\,T_R/l = M\Delta T$, where $M = 2\omega_r\,(T_0)\,T_R\,(\partial n/\partial T)\,/\,(nl)$ and $n(T)$ is the refractive index. We are assuming that the temperature change is small so that a Taylor expansion of $n(T)$ is valid. The normalized pump amplitude is given by $F = i\,(8\gamma P_{\rm in}/l^3)^{1/2}$, and $P = (1/L)\int_{-L/2}^{L/2}|\psi\,(x)\,|^2 dx$ is the normalized average intracavity power in the frequency comb. The normalized thermal coefficients $A = \lambda T_R M/\gamma$ and $B = 2T_R\kappa/l$ give the shift of the detuning in response to the intracavity power and the thermal relaxation rate, respectively. It is useful to define the ratio $C = -A/B$. For the stationary solutions of Eq. (43), we have $\Phi = -CP$. Hence, the stationary solution with a fixed value of $\alpha - CP$ and a fixed value of F is the same for any value of the thermal ratio C. The parameter B governs the rate at which a thermal perturbation relaxes, and hence it is necessary to move through the parameter space at a rate that is small compared to B in order for the evolution to be adiabatic. In physical units for the parameters of [83], we find that the relaxation rate is $[0.1\ \mu{\rm s}]^{-1}$ as shown in Table 2. So, the evolution through the parameter space must be slow compared to 0.1 μs. For the other example systems in Table 2, we find for the parameters in [85] that the evolution should be slow compared to 3.4 μs, while for the parameters in [46] the evolution should be slow compared to 1 ms.

In [72], we describe in detail the computational methods that we used to solve Eq. (43). We use boundary-tracking algorithms based on dynamical methods to find the stable regions. We use efficient split-step methods, combined with quantum noise,

Table 2: **Parameters for three experimentally demonstrated silicon-nitride microresonators or silica microresonators with relatively small [85], intermediate [83], and large [46] mode circumferences and hence three different values of the free spectral range (FSR).**

Parameter	[85]	[83]	[46]
Material	Si_3N_4	Si_3N_4	SiO_2
R [μm]	23	100	1500
FSR [GHz]	1004	240	22
T_R [ps]	1.00	4.16	45.4
β_2	-3.19×10^{-4}	-8.74×10^{-5}	-4.85×10^{-6}
γ [W^{-1}]	1.31×10^{-4}	8.80×10^{-4}	1.59×10^{-5}
l	3.22×10^{-3}	3.70×10^{-3}	5.52×10^{-4}
λ [K/J]	8.70×10^{3}	7.22×10^{5}	0.25
κ [MHz]	0.29	10	1×10^{-3}
A	-6.13×10^{-4}	-0.12	-9.38×10^{-4}
B	1.79×10^{-4}	0.022	1.65×10^{-4}
C	3.42	5.12	5.7
L	20.0	40.9	67.0
P_{in}/F^2 [mW]	15.8	3.89	4.78
f_{det}/α [MHz]	257	70.8	0.97

to find the time evolution.

In Table 2, we show parameters for three experimentally demonstrated silicon-nitride microresonators or silica microresonators with relatively small [85], medium [83], and large [46] mode circumferences and hence three different values of the free spectral range (FSR). We assume that all devices are operating at room temperature and are pumped at 1.5 μm.

4.3 Results

In Fig. 26, we show the stable regions when $L = 50$ for different cnoidal wave periodicities N, both with and without thermal effects. We recall that a cnoidal wave is a periodic waveform whose azimuthal period equals $2\pi/N$, where the periodicity N can be any positive integer [72]. When $N = 1$, the cnoidal wave corresponds to a single soliton. For $N \lesssim L/(2\pi)$, we found that cnoidal waves correspond approximately to

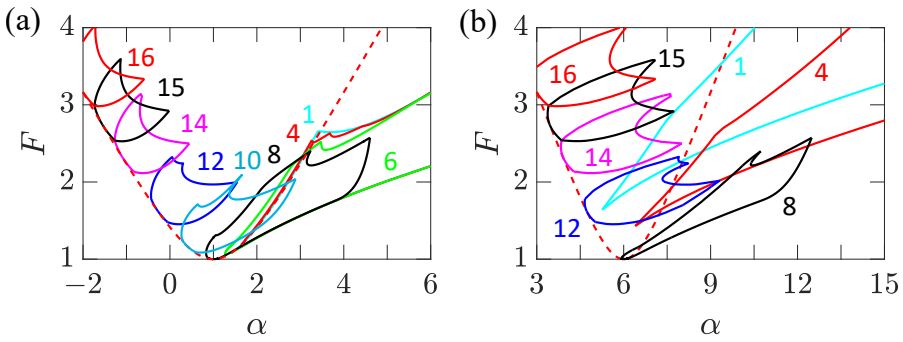

Figure 26: Stable regions of cnoidal waves (a) without ($C = 0$) and (b) with thermal effects ($C = 5$) at $L = 50$. For clarity, only a selection of the stable regions is plotted. Numbers label the periodicity N of the cnoidal waves. The dashed red curves show a limit below which continuous waves are stable. The scale for α is both shifted to larger values and scaled by a factor 1.5 in (b) relative to (a).

a periodic string of solitons, while when $N \gtrsim L/(2\pi)$, the cnoidal waves correspond to Turing rolls in which the periodically varying amplitude sits atop a pedestal of comparable magnitude. The choice $L = 50$ in Fig. 26 corresponds approximately to the experiments of Wang et al. [14]. The periodicities of the stable regions scale linearly with L [72] so that the regions in (α, F) that are stable for periodicity N_1 with $L = L_1$ are approximately the same as the regions that are stable for periodicity $N_2 = cN_1$ when $L = L_2 = cL_1$. The observed scaling with L is physically reasonable since an increase in L corresponds to an increase in the mode circumference, so that the physical length of the cnoidal wave period remains approximately constant as both L and periodicity N increase. Figure 26(a) shows the stable regions with no thermal effect ($C = 0$), while Fig. 26(b) shows the stable regions with $C = 5$, which corresponds to the coefficient for silicon nitride at room temperature [83]. Comparing Figs. 26(a) and 26(b), we see that thermal effects shift all the stable regions to larger detuning frequencies (larger α and lower pump frequencies). The regions are also stretched and skewed. When thermal effects are not included, the stable regions for low periodicities ($N \leq 5$ with $L = 50$) almost completely overlap. That is no

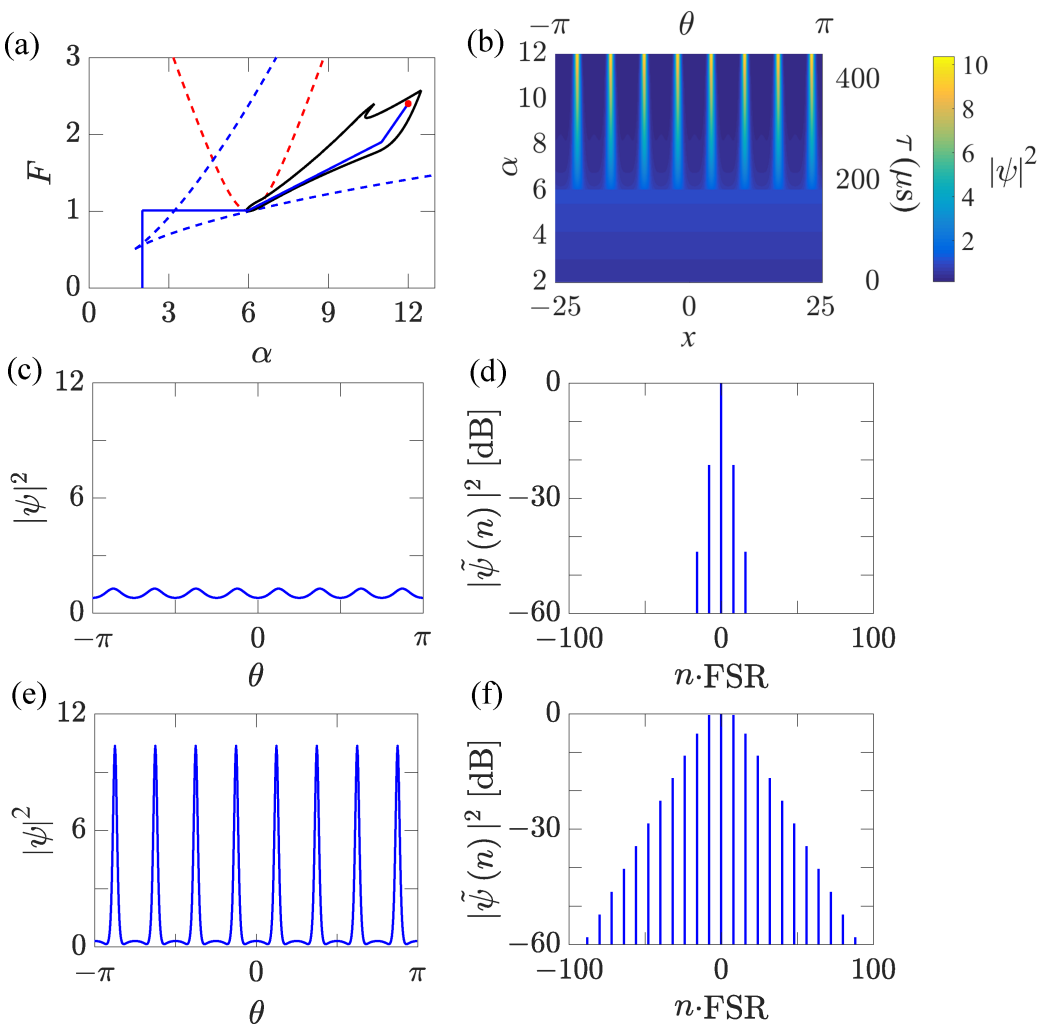

Figure 27: (a) Stable region of periodicity-8 cnoidal waves including thermal effects with $L = 50$ and $C = 5$ (black curve). The red-dashed curve shows a limit below which continuous waves are stable. The blue-dashed curves show the limits inside of which three continuous wave solutions exist that can be stable or unstable. Inside the triangular-shaped region surrounded by the blue dashed lines on two sides and the red-dashed curve on the right is a region where two stable continuous wave solutions exist with different amplitudes. (b) Evolution of the waveform when deterministically accessing the periodicity-8 cnoidal wave along the solid blue path, shown in (a). (c) Waveform of the periodicity-8 cnoidal wave and (d) its corresponding spectrum at $\alpha = 6$ and $F = 1.01$. (e) Waveform of the periodicity-8 cnoidal wave and (f) its corresponding spectrum at $\alpha = 12$ and $F = 2.4$ [red dot in (a)].

longer true when thermal effects are included. Cnoidal waves with a low periodicity correspond to a periodic stream of solitons, i.e., a soliton crystal [13,17,72,107–113], so that the stable regions are expected to overlap when thermal effects are not included. However, the intracavity power is approximately proportional to the periodicity, so that when thermal effects are included the detuning of the stable regions decreases as the periodicity decreases. We observe that there is a parameter regime in which stable single solitons exist, but stable soliton crystals do not. This result explains in part the usefulness of backward detuning to obtain single solitons [55] and underlines the crucial role that thermal effects play.

When thermal effects can be neglected, as in the experiments of Moille et al. [85], we previously showed that a broad bandwidth frequency comb can be obtained deterministically by appropriately moving through the $\alpha \times F$ [(frequency detuning)$\times$(pump amplitude)] parameter space. First, one raises the pump power. Below the red-dashed curve, a continuous wave is generated that increases in amplitude as the pump amplitude increases. When the red-dashed curve is crossed, the continuous wave becomes unstable, and a cnoidal wave is generated. When $L = 50$, this cnoidal wave has periodicity 8, corresponding to the solid black curve labeled 8 in Fig. 26(a). When it appears, this cnoidal wave corresponds to a narrowband frequency comb so that in the azimuthal domain there is a periodic array of eight peaks that sits atop a pedestal, as shown in Fig. 27(c). Next, one increases the detuning while simultaneously raising the pump power so that the system remains within the stable region for the cnoidal wave that was created. As the detuning and pump power are increased, the pedestal decreases and the peaks sharpen, so that the cnoidal wave transforms into a periodic train of solitons that is a soliton crystal, as shown in Fig. 27(e) [13, 17, 72, 107–113].

When thermal effects are taken into account, this deterministic path must be somewhat modified. In Fig. 27(a), there is a triangular-shaped region surrounded by blue dashes on two sides and the red-dashed curve on the right. Inside this region,

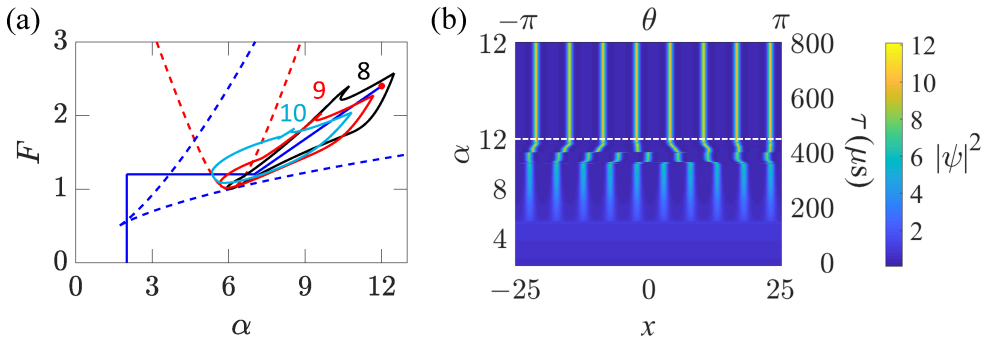

Figure 28: (a) Stable regions of periodicity-8 (black), -9 (red) and -10 (cyan) cnoidal waves including thermal effects with $L = 50$ and $C = 5$. (b) The evolution to access periodicity-8 cnoidal waves along the solid blue path in (a). Once the path reaches $\alpha = 12$, we continue the evolution without changing α.

two stable continuous wave solutions exist with different amplitudes. If this region is reached by passing through the lower blue-dashed curve, only the lower amplitude solution is observed. In that case, if one enters the region where the cnoidal waves are stable, which is surrounded by the solid black curve in Fig. 27(a), the continuous wave remains stable, and a cnoidal wave is not observed [116]. Instead, one must enter the triangular region through the upper blue-dashed curve. In that case, a higher-amplitude continuous wave is observed, which goes unstable when the region where

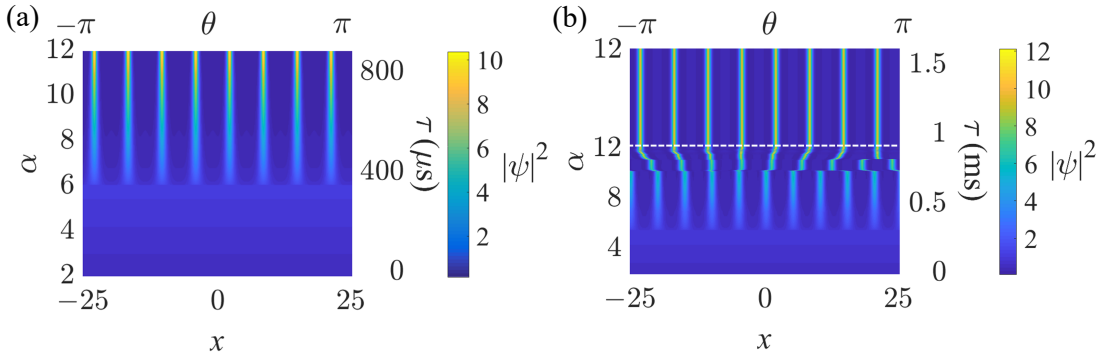

Figure 29: Simulations at half the rate and twice the duration as in (a) Fig. 27(b) and (b) Fig. 28(b). As was the case in Fig. 28(b), we continue the evolution in Fig. 29(b) without changing α beyond the time indicated by the white-dashed line.

cnoidal waves exist is entered, so that the periodicity-8 cnoidal wave is obtained, corresponding to a narrowband frequency comb [116]. Continuing to increase α and F along the solid blue path shown in Fig. 27(a), the peaks become more narrow and the pedestal between the peaks decreases, so that the waveform gradually transforms into a soliton crystal, corresponding to a broadband frequency comb. The solid blue path shown in Fig. 27(a) has a bend. The purpose of this bend is for the path to remain within the stable region for the periodicity-8 cnoidal wave. It is possible to reach this point by moving along the solid blue curve in Fig. 28(a). In this case, a cnoidal wave with periodicity 10 first appears. As the system evolves along the solid blue curve, the periodicity-10 cnoidal wave first goes unstable, yielding a periodicity-9 cnoidal wave, which goes unstable in turn, yielding a periodicity-8 cnoidal wave. We show the evolution of the waveform in Fig. 28(b). At the time indicated by the white dashed line, we no longer change α and F, but continue the evolution to ensure that we have reached a stable solution. Other paths through the parameter space that end at the same (α, F) also yield the same broadband cnoidal wave. The key requirements are to enter the triangular region in Figs. 27(a) and 28(a) through the upper dashed curve and to move adiabatically through the parameter space so that the microresonator is always close to thermal equilibrium.

The simulations that we carried out to access the broadband cnoidal wave that we show in Figs. 27(b) and 28(b) were carried out adiabatically. To verify that the rate at which we changed the system parameters is slow enough to be adiabatic, we carried out simulations in which we move through the parameter space at half the rate in physical time that we used in Figs. 27(b) and 28(b). Hence, the simulation was twice as long in physical time. We show the results in Fig. 29. While details of the transient evolution change, particularly along the path that we show in Fig. 28(a), the end result does not change except for an azimuthal shift.

We also compare the stability maps for different values of the thermal parameter C

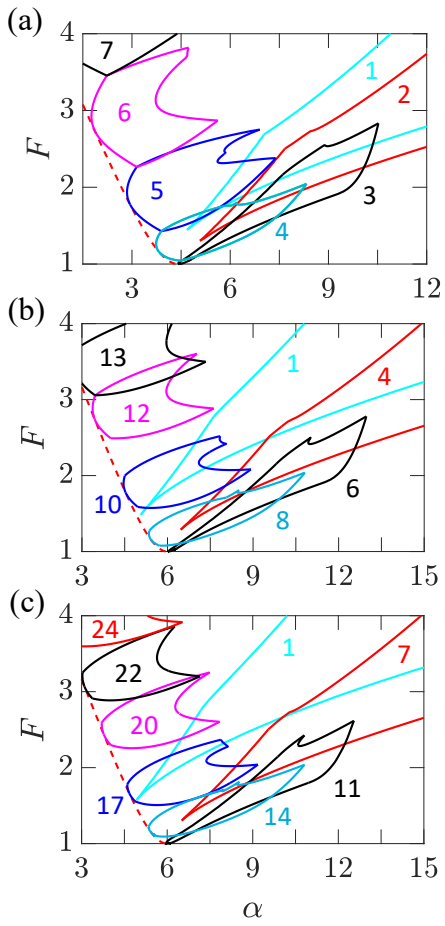

Figure 30: Stable regions for cnoidal waves with different values of the thermal parameter C and longitudinal mode circumference L: (a) $C = 3.42$ and $L = 20$, (b) $C = 5$ and $L = 40$, (c) $C = 5$ and $L = 70$. In (b) and (c), we only show a selection of the stable regions for clarity. Numbers label the periodicity N.

and longitudinal mode circumference L. Figure 30 shows the stable regions for cnoidal waves for (a) $C = 3.42$ and $L = 20$, (b) $C = 5$ and $L = 40$, and (c) $C = 5$ and $L = 70$, which correspond to the experimental parameters in [85], [83], and [46], respectively. Comparing Figs. 30(b) and 30(c), the expected linear scaling of the periodicity of the stable regions is clearly visible. This approximate scaling is somewhat less visible when comparing Fig. 30(a) with the others, both because the scaling becomes less exact when L decreases and because we used a different value of C in Fig. 30(a) in order to better match the experiments in [85].

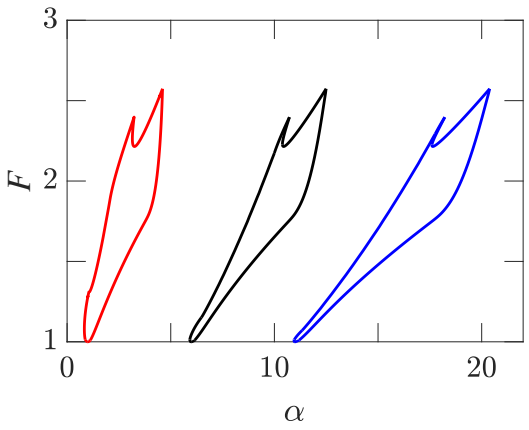

Figure 31: Stable regions for periodicity-8 cnoidal waves with different values of the thermal parameter C and with $L = 50$. The numbers label the thermal parameter C.

Figure 31 shows the stable regions for three different values of C for periodicity-8 cnoidal waves when $L = 50$. As C increases, stable regions move to larger α. They are also skewed to larger α as F becomes larger, which is expected since a larger F corresponds to a larger intracavity power P and hence a larger change in α.

4.4 Conclusion

We have described a method to deterministically access broad bandwidth frequency combs in microresonators by moving adiabatically through the $\alpha \times F$ [(frequency detuning)×(pump amplitude)] parameter space. This method produces frequency combs that consist of cnoidal waves with periodicity greater than 1. In the broad bandwidth limit, the frequency comb corresponds to a periodic train of solitons that is a soliton crystal.

Thermal effects play a critical role in microresonators and must be taken into account. When thermal effects can be ignored, it is possible to deterministically access broadband combs by first raising the pump power to enter the stable region for cnoidal waves and then simultaneously increasing the detuning and pump power in an appropriate ratio. When thermal effects are taken into account, it is necessary to raise

the pump power and then increase the detuning along a path in the parameter space that produces a high-amplitude continuous wave. From that point in the parameter space, it is possible to access broad bandwidth cnoidal waves that are soliton crystals by simultaneously increasing the detuning and pump power along an appropriate path in the parameter space.

While our examples have mostly focused on $L = 50$, there is a scaling relation that makes it possible to extend our results to a large range of L values, and our results indicate that it is possible to deterministically obtain broad bandwidth frequency combs in any microresonator by moving adiabatically through an appropriate path in the $\alpha \times F$ parameter space.

When thermal effects can be neglected, it was previously shown that the stable regions for cnoidal waves in the $\alpha \times F$ parameter space almost completely overlap for small periodicities. In this limit, which corresponds to broadband frequency combs, the cnoidal waves are single solitons or soliton crystals. When thermal effects are important, the stable regions for soliton crystals with different periodicities separate. This result suggests that it may be possible to deterministically obtain single solitons by backwards-detuning from a soliton crystal. This suggestion is compatible with the experimental results of Guo et al. [55] that show that single solitons can be obtained by backwards-detuning from a random array of solitons and by Karpov et al. [111] that show that it is possible to deterministically move in the $\alpha \times F$ parameter space from one soliton crystal to another. We have found that it is indeed possible to deterministically obtain single solitons in some cases with small L, but we have not carried out a systematic study.

5 Deterministic Access of Frequency Combs with avoided crossings

5.1 Introduction

In the LLE, Eq. (2), it is assumed that only a single transverse mode family is important. However, the presence of different transverse mode families in a microresonator can lead to avoided crossings that strongly perturb the linear dispersion relation and require modification of the LLE [6, 7, 16, 56, 62]. In this chapter, we first focus on explaining the experimental results of Bao et al. [56], and we then move on to a more global study of the conditions that are required to deterministically access solitons and soliton crystals.

The effect of avoided crossings appears when longitudinal modes from two different transverse mode families transverse mode families spatially overlap and have nearly equal frequencies. Without the spatial overlap, the dispersion curve (frequency vs. wave number) for the two mode families will cross each other. If the frequencies of the longitudinal modes at the mode number nearest the crossing point are close, then the transverse mode profiles change significantly and become superpositions of the profiles of the two transverse modes at that mode number. The frequencies of both mode number are strongly modified and pushed apart. This effect is similar to the phenomenon of energy level splitting in atomic and molecular systems due to the Zeeman effect [117].

Bao et al. [56] compared two microresonators that operated in the anomalous dispersion regime. One of them had a strong avoided crossing and the other did not. Otherwise, the microresonators were nearly identical. They found that they could obtain a soliton deterministically in the microresonator with a strong avoided crossing, while a soliton could only be obtained randomly in the microresonator with a weak avoided crossing. In both cases, Bao et al. carried out 40 laser scans in

which the frequency was red-detuned. They observed a soliton step in every scan in the case with a strong avoided crossing and were able to capture the soliton by backward tuning the scan. They only observed a soliton step once in the case with weak detuning.

There has been accelerating interest in the use of avoided crossings to enable soliton formation. The importance of avoided crossings in single soliton formation was noted by Herr et al. [118], where they were a deleterious effect that when too large impeded the soliton formation. An avoided crossing between different polarization modes was noted by Ramelow et al. [7] and again cited as a deleterious effect that could impede single soliton formation. Later work by Bao et al. [56] and Xue et al. [6, 62] showed however that avoided crossing can play a positive role and can be harnessed to produce bright single solitons, dark soliton molecules, and dark soliton crystals. The work of Cole et al. [17] in which the authors demonstrated that avoided crossings play a crucial role in generating and locking soliton crystals. They classified the different types of soliton crystals that can form, and showed how the location of an avoided crossing in the frequency spectrum impacts which type of soliton crystal forms. Later work by Karpov et al. [111] demonstrated that it is possible to move between different soliton crystal states by moving along an appropriate path in the (detuning)×(pump amplitude) [$\alpha \times F$] parameter space. Recent work has shown that it is possible obtain soliton crystals in which the periodicity and hence the mode spacing is controlled by using photorefractive tuning [119] and dual-coupled resonators [113], both of which change the frequency effect of the avoided crossings relation to the resonant frequency. Extensive work summarized by Tan et al. [120] shows that it is possible to use imperfect soliton crystals generated by an avoided crossing to realize many RF-photonic functionalities.

Despite the growing interest in the use of avoided crossings to deterministically access and control cnoidal waves, there has not yet been a systematic study to deter-

mine where in the parameter space stable cnoidal waves exist, and can be obtained deterministically. The parameters can be tuned to some extent. The strengths and offsets of the avoided crossings are fixed in almost all experiments similarly are determined by the microresonator geometry, and even when they can be tuned, the tuning range is limited [113, 119] It is difficult if not impossible to experimentally carry out a systematic study over a broad range of strengths and offsets. Thus, simulation computationally play a critical role in designing systems so that single solitons or other cnoidal waves can be obtained deterministically.

In this chapter, we describe work that is aimed at carrying out a systematic study of avoided crossings. The parameter space is large. In addition to the usual parameters that play a role in the LLE (α, F, and L), there are two parameters that govern the strength and offset of an avoided crossing. In order to restrict the problem, we chose to focus on a limited set of the parameters α, F, and L, and only vary the strength and offset of the avoided crossing. Additionally, we focused almost entirely on single solitons with only a brief look at other cnoidal waves. Even with these limitations, we found a complex behavior from which we could draw few general conclusion. In the case of single solitons, we found that the behavior was roughly periodic with the FSR as the offset increased at a fixed strength. Offsets at which solitons can be found deterministically are interleaved with offsets at which they can not. The soliton pedestal has oscillations that are roughly equal to the soliton duration, but this equality is very rough. As the strength increases, it is generally easier to obtain solitons deterministically at least over the range of offsets that we examined. However, we found that at low offsets, a large strength makes it difficult to obtain solitons deterministically. We also found that at large offsets it is possible to obtain solitons deterministically even at low strengths; and there is a gap in the range of strengths at which solitons can be obtained deterministically. While we found that it is possible to obtain cnoidal waves deterministically with a large

offset, the range of strengths at which they can be obtained is limited at the offset that we examined in detail.

We have clearly only scratched the surface of this subject, but it is our hope that the work presented here will point the way to a more comprehensive study from which design rules can be obtained.

5.2 Avoided crossings in the anomalous dispersion regime

Following Chembo and Menyuk [12], we define the spatial Fourier transform of $\Psi(\theta,\tau)$ as

$$\tilde{\Psi}_m(\tau) = \int_{-\pi}^{\pi} \Psi(\theta,\tau)\exp[i(m-m_0)\theta]\,\frac{d\theta}{2\pi}, \tag{44}$$

where m_0 is the mode number of the frequency that is closest to the pump frequency, so that $\sigma = (\omega_p - \omega_0)T_R$ in Eq. (2), where ω_p is the angular pump frequency and ω_0 is the angular frequency corresponding to to mode number m_0. The angular frequency of mode m, ω_m, in the presence of avoided crossings can now be written as [56, 118]

$$\omega_m = \omega_0 + \omega'(m-m_0) + \frac{1}{2}\omega''(m-m_0)^2 - \frac{A}{2(m-m_0-b)}, \tag{45}$$

where ω' and ω'' are the first- and second-order dispersion contributions to ω_m, while A and b denote the strength and offset of the avoided crossing. It is useful to set $\mu = m - m_0$, so that

$$\omega_\mu = \omega_0 + \omega'\mu + \frac{1}{2}\omega''\mu^2 - \frac{A}{2(\mu-b)}. \tag{46}$$

Neglecting for the moment the loss, Kerr, and pump contributions, and keeping only the dispersive contributions in Eq. (46), we have

$$\left.\frac{d\tilde{\Psi}_\mu}{d\tau}\right|_{\text{disp}} = i\left[\omega_0 - \omega_p + \omega'\mu + \frac{1}{2}\omega''\mu^2 - \frac{A}{2(\mu-b)}\right]. \tag{47}$$

Using the inverse Fourier transform

$$\Psi(\theta,\tau) = \sum_{\mu=-\infty}^{\infty} \tilde{\Psi}_\mu(\tau)\exp(-i\mu\theta), \tag{48}$$

we find

$$\begin{aligned}\left.\frac{\partial\Psi(\theta,\tau)}{\partial\tau}\right|_{\text{disp}} &= -i(\omega_p-\omega_0)\Psi(\theta,\tau) - \omega'\frac{\partial\Psi(\theta,\tau)}{\partial\theta} - \frac{i\omega''}{2}\frac{\partial^2\Psi(\theta,\tau)}{\partial\theta^2} \\ &\quad - i\sum_{\mu=-\infty}^{\infty}\frac{A}{2(\mu-b)}\tilde{\Psi}_\mu(\tau)\exp(-i\mu\theta).\end{aligned} \tag{49}$$

To eliminate the first derivative in θ, which corresponds to the group rotation velocity motion in the microresonator, we make the transformation $\tau' = \tau$ and $\theta' = \theta - \omega'\tau$. After removing the primes and including the loss, Kerr, and pump contributions, we finally obtain

$$T_R\frac{\partial\Psi}{\partial\tau} = -\frac{i\beta_2}{2}\frac{\partial^2\Psi}{\partial\theta^2} + i\gamma|\Psi|^2\Psi + \left(-i\sigma - \frac{l}{2}\Psi\right) + \sqrt{P_{\text{in}}} - i\sum_{\mu=-\infty}^{\infty}\frac{A}{2(\mu-b)}\tilde{\Psi}_\mu\exp(-i\mu\theta), \tag{50}$$

where we note that $\beta_2 = \omega''T_R$. We now use the same normalizations that we used to go from Eq. (2) to Eq. (3), and we find

$$\frac{\partial\psi}{\partial t} = i\frac{\partial^2\psi}{\partial x^2} + i|\psi|^2\psi - (i\alpha+1)\psi + F - i\sum_{\mu=-\infty}^{\infty}\frac{a}{b-\mu}\tilde{\psi}_\mu\exp(-2\pi i\mu x/L), \tag{51}$$

where $\tilde{\psi}_\mu = (2\gamma/l)^{1/2}\tilde{\Psi}$ and $a = A/l$.

In our preliminary study of the stability of cnoidal waves, we first ran evolutionary simulations in which we solved Eq. (51). We used the same parameters as Bao et al. [56] in the case where the mode interaction strength is large, except that we used $\alpha = 9$ instead of $\alpha = 11.89$. We list the complete set of parameters that we used in Table 3. We verified that the single soliton profile remains qualitatively unchanged when we increase α as long as we remain in the region in the $\alpha \times F$ parameter

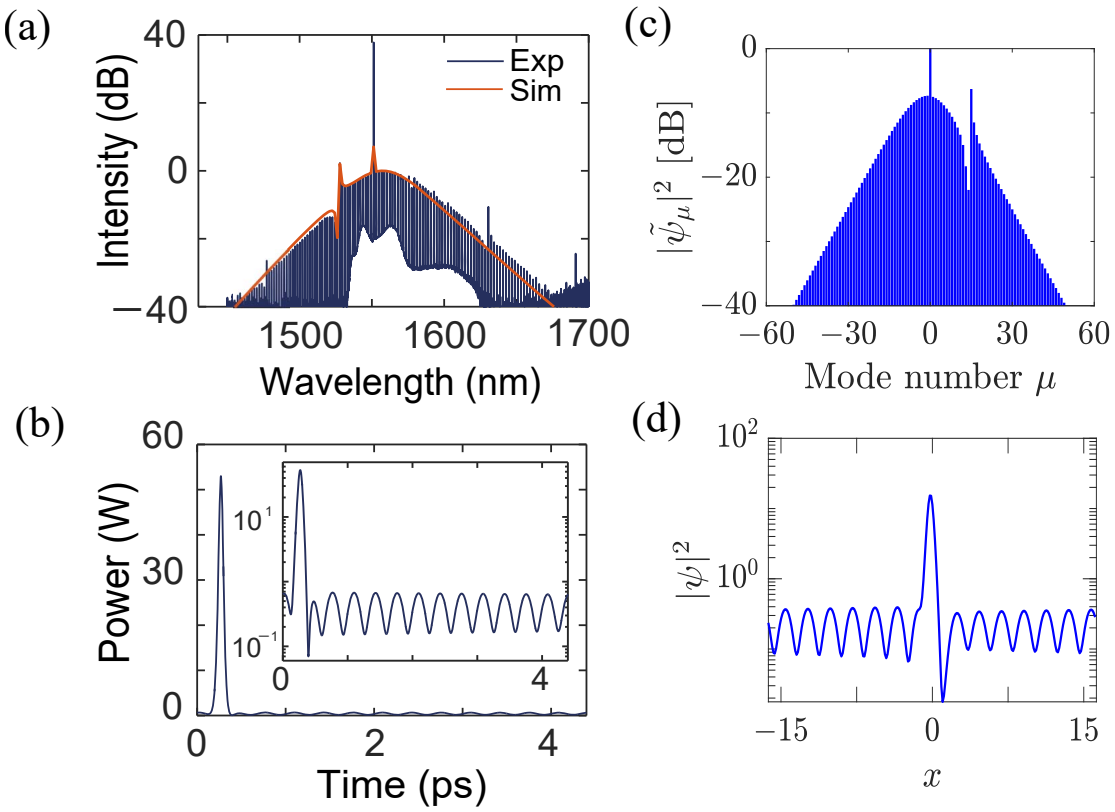

Figure 32: (a) Frequency spectrum and (b) its corresponding soliton in Ref. [56]. (c) Frequency spectrum and (d) its corresponding soliton obtained using normalized parameters from Ref. [56]. Here the normalized pump amplitude $F = 4.18$.

Table 3: **Physical and normalized parameters for silicon-nitride microresonators with avoided crossing employed in [56].**

Parameter	[56]
T_R [ps]	4.4
P_{in} [W]	0.22
γ [$\text{W}^{-1}\text{m}^{-1}$]	0.9
β_{ph} [$\text{ps}^2\text{km}^{-1}$]	-81
A [rad-ns^{-1}]	7.6
b	13.8
L	32.5
F	4.18

space where single solitons are stable. In Fig. 32, we compare the result of our evolutionary simulation to the simulation results of Bao et al. [56, Fig. 3]. We see that the results are qualitatively similar. In particular, the avoided crossing leads to

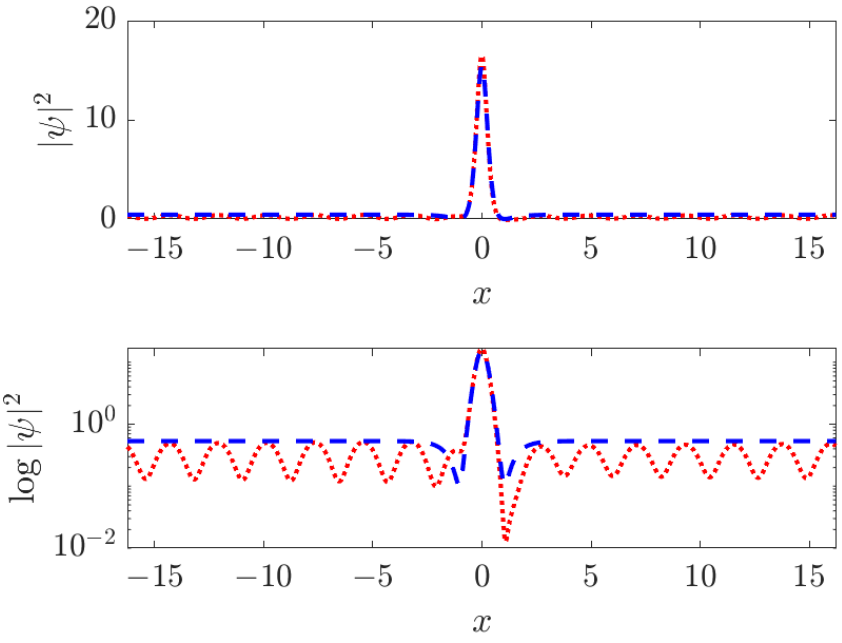

Figure 33: Soliton power using linear (top) and logarithmic (bottom) scales at $a = 12$ and $b = 13.8$. The red-dotted and blue-dashed curves show respectively the soliton power with and without avoided crossings.

a large oscillatory pedestal. The mode crossing is located at $b = 13.8$, which leads to an oscillation period that is approximately L/b, so that we observe 13 oscillation peaks, not including the single soliton. Bao et al. plotted the spectrum as a function of wavelength, not mode number, while we plotted the spectrum as a function of the mode number. As a result, the relevant avoided crossing appears to the left of the mode spectrum's maximum in the figure of Bao et al. and to the right of the maximum in ours. The avoided crossing leads to an asymmetric frequency spectrum for the soliton and hence a velocity shift with respect to the group rotation velocity at the soliton's central frequency, which we must take into account when finding the stationary solutions.

In order to see the details of the soliton waveform, we plot its power in Fig. 33 using both a linear and a logarithmic scale. The red-dotted and blue-dashed curves

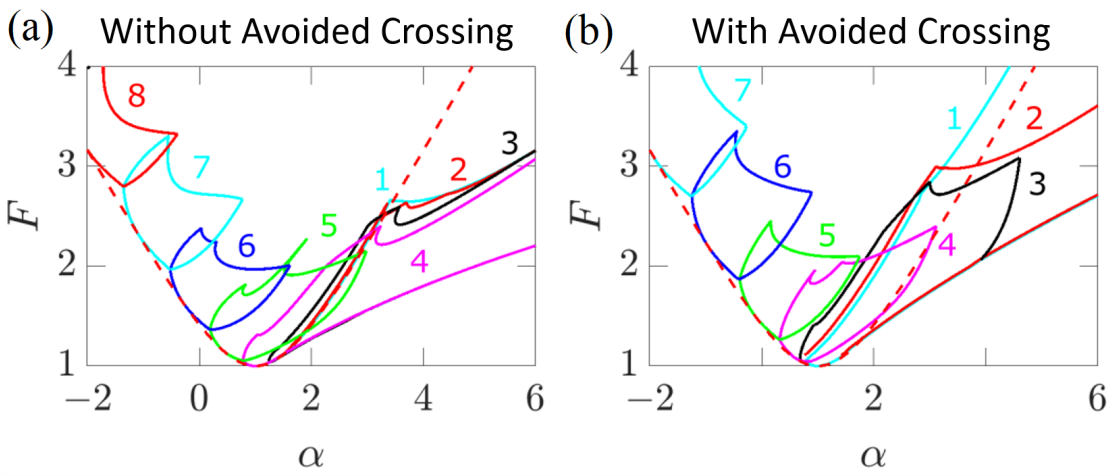

Figure 34: (a) Stability chart in the case without avoided crossings. (b) Stability chart in the case with avoided crossings for the parameters in Ref. [56] and Table 3

show the waveforms with and without an avoided crossing. The avoided crossing leads to oscillations in the pedestal, and the number of oscillations is close to the offset $b = 13.8$. The soliton has a pedestal with 13 complete oscillations and one incomplete oscillation.

In order to determine whether a soliton can be obtained deterministically, we ran 100 evolutionary simulations starting from quantum noise as we scanned from $\alpha = -3$ to $\alpha = 6$. We take steps $\Delta\alpha = 10^{-3}$ and run for a time $\Delta t = 100$. We have verified that this result is insensitive to the choice of $\Delta\alpha$ and Δt. When all 100 simulations produce a soliton, the soliton generation is considered deterministic. The case that we show in Figs. 32 and 33 corresponds to one realization with the parameters of Table 3 and $\alpha = 6$. This case is deterministic.

We next studied the linear stability as α and F vary with $L = 25$. The other parameters are the same as in Figs. 32 and 33. We chose a smaller value of L in order to compare the stability chart with an avoided crossing to the stability chart without an avoided crossing that already appeared in Fig. 15. We compare the stability charts with and without avoided crossings in Fig. 34. We observe that stable region

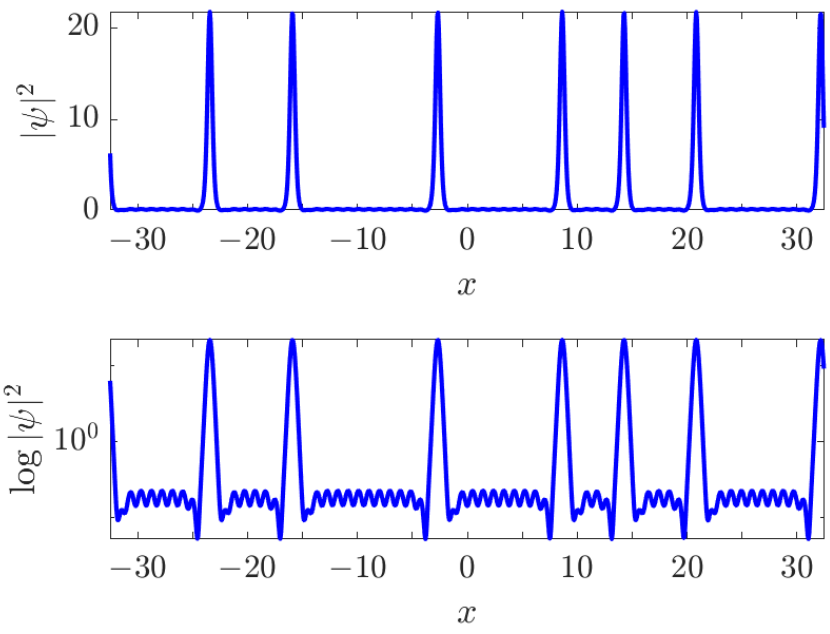

Figure 35: The power of a seven-peak soliton crystal shown using a linear (top) and logarithmic (bottom) scale with $a = 12$ and $b = 49.8$.

for single solitons is greatly enhanced with avoided crossings and no longer overlaps with the stable region for other cnoidal wave solutions. This result suggests that deterministic soliton generation is correlated with a stability region; however, further study is needed to verify this correlation. In order to apply the dynamical method that is described in Sec. 3, we must compensate for the velocity shift so that we can have a stationary pulse, which we do using the procedure described by Wang et al. [63].

We found that it is also possible to generate imperfect soliton crystals deterministically, although It is necessary to change the system parameters. With $F = 3.5$, $L = 65$, $a = 12$, and $b = 49.8$, we found the waveform that we show in Fig. 35 at the end of a scan with $\alpha = 6$. For this set of parameters a soliton crystal with seven solitons appears deterministically, although the locations of the solitons vary from one realization to the next. Once again the number of peaks is close to the offset b,

Table 4: **Percentage of scans in which single solitons are accessed at $b = 13.8$.**

a	percentage
8	0%
10	0%
12	100%
14	100%
16	100%

and the period of the oscillations roughly equals the duration of the soliton pulses.

We next studied the accessibility of single solitons with avoided crossings where we vary a and b over a wide range. We set $F = 3.5$, $L = 32.5$, and as before we scan α from -3 to 6 and ran 100 realizations to determine whether a solution is deterministic.

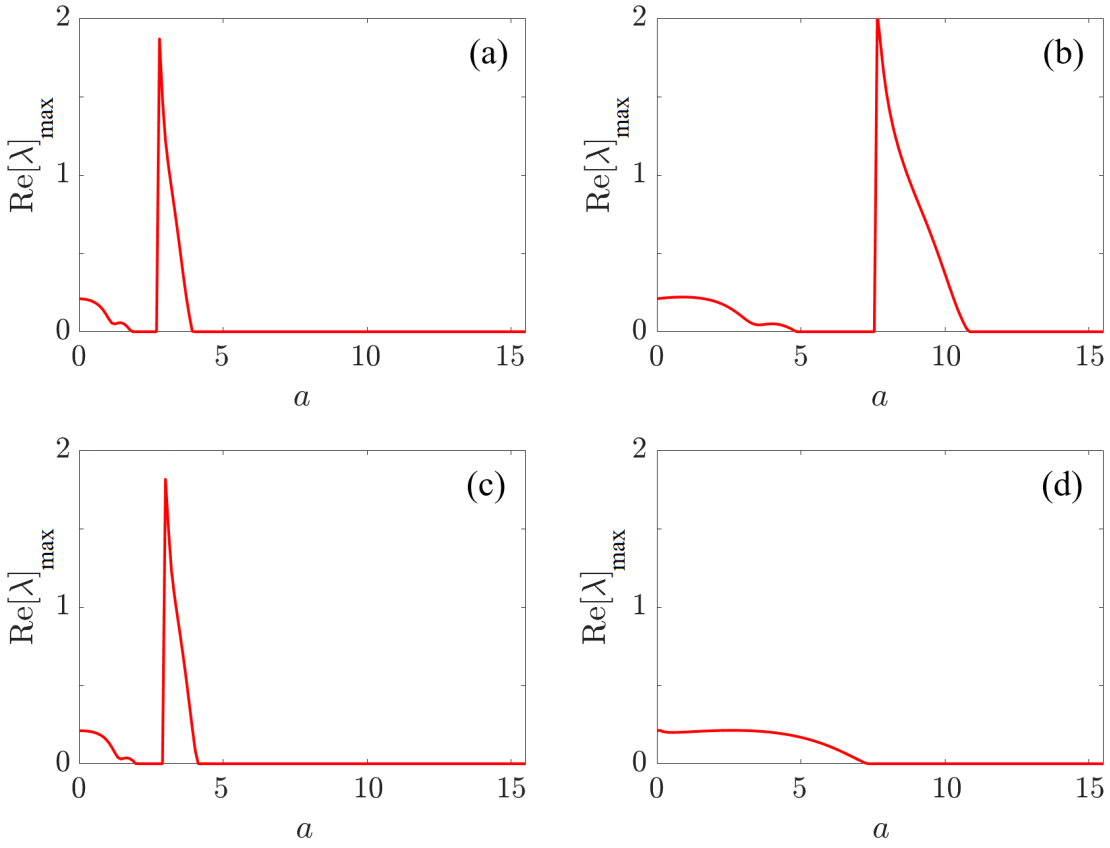

Figure 36: Maximum real parts of the eigenvalues of the dynamical spectra at (a) $b = 12.8$, (b) $b = 13.5$, (c) $b = 13.8$, and (d) $b = 14.0$. Here $\alpha = 6$ and $L = 25$.

Table 5: **Percentage of scans in which single solitons are accessed at $a = 12$.**

b	percentage
13.1	48%
13.3	0%
13.5	100%
13.7	100%
13.9	100%

We first set $b = 13.8$ and varied a from 8 to 16, and we show the results in Table 4. Beginning at $a = 12$, single solitons can be accessed deterministically. Solitons must be stable in order to be accessible, but the converse is not true since other waveforms, including continuous waves, can be present over the same parameter range in which solitons are stable. Figure 36 shows the maxima of the real parts of the dynamical spectra $\mathrm{Re}[\lambda]_{\max}$ for single solitons that are obtained at α for different values of b. The other parameters are $b = 32.5$ and $F = 3.5$. There is always an eigenvalue at 0, and solitons are stable when $\mathrm{Re}[\lambda]_{\max} = 0$. At $b = 12.8$ and 13.8, single solitons are stable beyond $a = 5$. Single solitons are deterministically accessed at $a = 12$, 14, and 16. In these cases, single solitons are stable, and other types of solitons are not stable. However, at $a = 8$ and 10, single solitons are not accessed even though they are stable. Instead, randomly located solitons are obtained.

Next, we studied the accessibility of single solitons in microresonators when the avoided crossing strength is fixed at $a = 12$ and the avoided crossing offset b varies. Single solitons are deterministically accessed in some, but not all cases. We show the results for $b = 13.1$–13.9 in Table 5. Figure 37 shows $\mathrm{Re}[\lambda]_{\max}$ as b varies. Single solitons are deterministically accessed at $b = 13.5$, 13.7, and 13.9 where they are stable, and multiple soliton solutions are not stable. At $b = 13.3$, single solitons do not exist, while at $b = 13.1$, both single solitons and continuous waves are stable.

In Fig. 38, we show the soliton stability over a wide range of b-values with $a = 12$. We let $S(b) = 1$ when single solitons are stable, and we let $S(b) = 0$ when they are

not. Our results indicate that single solitons are stable in non-continuous regions of b, and the pattern of stable and unstable regions is roughly periodic with a period equal to the FSR.

We also attempted to access other types of solitons deterministically. Figure 39 shows $\mathrm{Re}[\lambda]_{\mathrm{max}}$ for single solitons (red solid) and a cnoidal wave with $N_{\mathrm{per}} = 2$ (a two-soliton perfect soliton crystal) (blue dashed) at two different offsets. As shown in Fig. 39(a), there exists a range surrounding $a = 5$ where $N_{\mathrm{per}} = 2$ cnoidal waves are stable while single solitons are unstable. At $a = 5.6$, we found that $N_{\mathrm{per}} = 2$ cnoidal waves can be accessed deterministically.

In Fig. 40, we summarize our study of the accessibility of single solitons in the parameter space (a, b). Different colors show the probability of single soliton solutions that are obtained at the end of each scan. Our results indicate that single solitons are deterministically accessible over a wide range of a and b as we change b in unit increments, starting at $b = 10.8$. We chose unit increments with a fractional part equal to 0.8 since the scan of stable values in Fig. 38 indicates that this fractional part is most likely to produce stable solutions. As b increases, it is generally the case that the threshold to obtain solitons deterministically also increases. However, we

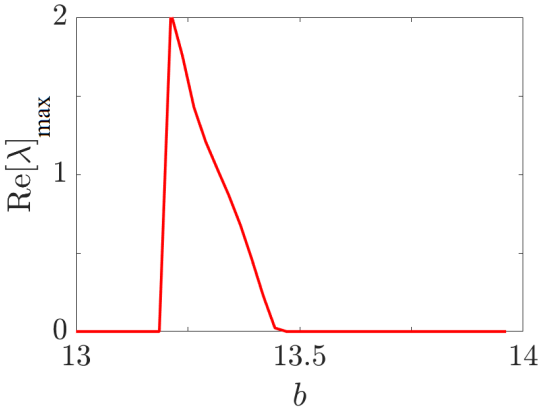

Figure 37: Maximum real parts of the eigenvalues of the dynamical spectra at $a = 12$. Here $\alpha = 6$ and $L = 25$.

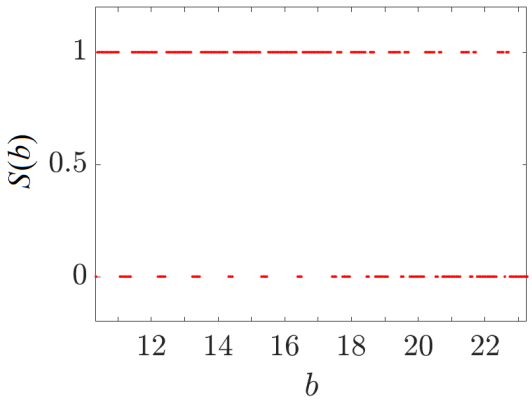

Figure 38: Stability of single solitons at $a = 12$. $S(b) = 1$ corresponds to stable single solitons, while $S(b) = 0$ corresponds to unstable single solitons. The roughly periodic variation of $S(b)$ is visible. Here $\alpha = 6$ and $L = 25$.

also see that a second region where single solitons can be obtained deterministically appears when $a = 5$ and $b \leq 15.8$.

We extended our prior study of the seven-soliton-crystal solutions that we accessed in Fig. 35 by varying the value of a. We show that results in Table 6. This solution could only be obtained deterministically when $a = 40$.

In general, it is possible to deterministically generate either single solitons or

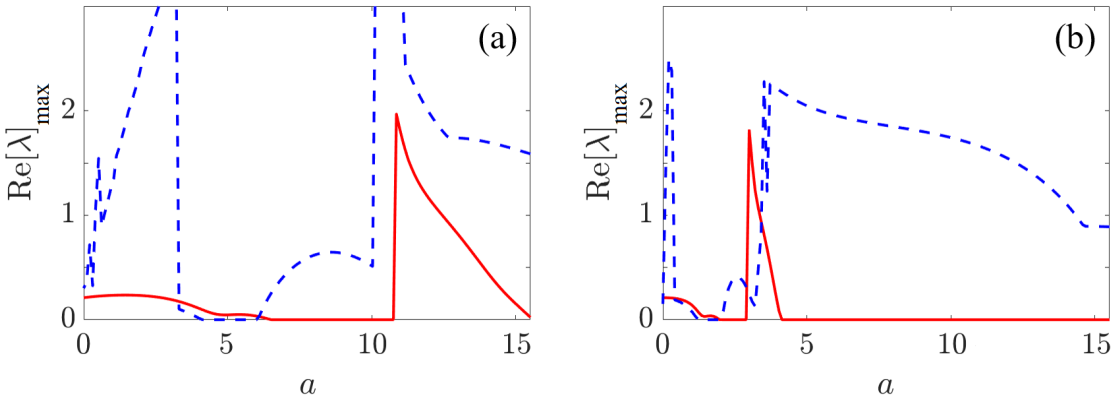

Figure 39: Maximum real parts of the eigenvalues of the dynamical spectra for single solitons (red solid) and double solitons (blue dashed) at (a) $b = 13.3$, (b) $b = 13.8$. Here $\alpha = 6$ and $L = 25$.

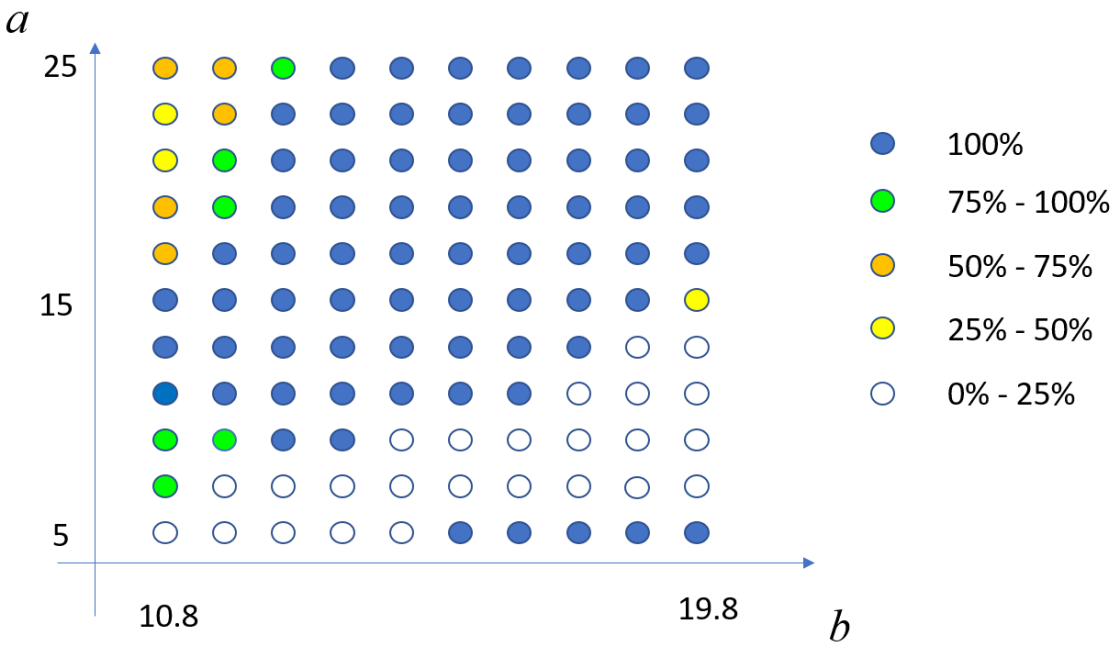

Figure 40: Accessibility of single solitons in the parameter space of (a, b). Different colors show the range of accessible rate.

Table 6: **Percentage of scans in which seven-soliton crystals are accessed at** $b = 49.8$**.**

a	percentage
5	12%
10	19%
15	27%
20	29%
25	35%
30	41%
35	45%
40	100%
45	44%
50	41%
55	41%

solitons crystals by carefully designing the device parameters, but unfortunately our results point to no clear design rules.

5.3 Conclusion

In this section, we studied the stability and the deterministic accessibility of solitons in microresonators with avoided crossings. We derived an appropriately modified Lugiato-Lefever equation (LLE) that takes into account an avoided crossing with a fixed strength and offset relative to the resonant frequency. We found that the avoided crossing induces oscillations in the soliton pedestal, and the number of oscillations approximately equals the avoided crossing offset that has been normalized to the FSR. We found that the duration of a single soliton that can be obtained deterministically roughly equals the oscillation period. We also found a seven-period soliton crystal that can be obtained deterministically, and the oscillation period of its pedestal roughly equals the duration of the single solitons. Setting $L = 25$, we made a stability chart for the single solitons that corresponds to the a and b values at which a single soliton can be obtained deterministically, and we found that the stable region for single solitons is substantially enlarged. We then extended the range of a and b values over which we examined where solitons can be obtained deterministically. In some cases, we also examined the stability of the single soliton solutions. We found that single solitons in many cases cannot be accessed deterministically even when they are stable because the single soliton solutions coexist with other stable solutions. We generally found that as b increases in steps of 1, the minimum value of a at which solitons can be deterministically accessed also increases. However, we also found that a second range of a-values where solitons can be deterministically accessed appeared when b is larger than some threshold value. Finally, we examined the accessibility of the seven-period soliton crystal solutions as a varies, and we found only one value of a at which the soliton crystal can be accessed deterministically. Our results indicate that solitons can be accessed deterministically over a broad range of parameters. However, we did not find design rules that can point to where in the parameter space (a,b) single solitons can be deterministically accessed. We anticipate that our results

are a first step towards achieving that goal.

References

[1] J. D. Jost, T. Herr, C. Lecaplain, V. Brasch, M. H. P. Pfeiffer, and T. J. Kippenberg, "Counting the cycles of light using a self-referenced optical microresonator," Phys. Rev. A **87**, 706–711 (2015).

[2] P. Del'Haye, A. Coillet, T. Fortier, K. Beha, D. C. Cole, K. Y. Yang, H. Lee, K. J. Vahala, S. B. Papp, and S. A. Diddams, "Phase-coherent microwave-to-optical link with a self-referenced microcomb," Nat. Photon. **10**, 516–520 (2016).

[3] P. Del'Haye, A. Schliesser, Olivier Arcizet, Tobias Wilken, Ronald Holzwarth, and Tobias Kippenberg, "Optical frequency comb generation from a monolithic microresonator," Nature **450**, 1214–1217 (2007).

[4] S. Coen, H. G. Randle, T. Sylvestre, and M. Erkintalo, "Modeling of octave-spanning Kerr frequency combs using a generalized mean-field Lugiato-Lefever model," Opt. Lett. **38**, 37–39 (2013).

[5] T. Herr, V. Brasch, J. D. Jost, C. Y. Wang, N. M. Kondratiev, M. L. Gorodetsky, and T. J. Kippenberg, "Temporal solitons in optical microresonators," Nat. Photon. **8**, 145–152 (2014).

[6] X. Xue, Y. Xuan, Y. Liu, P. -H. Wang, S. Chen, J. Wang, D. E. Leaird, M. Qi, and A. M. Weiner, "Mode-locked dark pulse Kerr combs in normal-dispersion microresonators," Nat. Photon. **9**, 594–600 (2014).

[7] S. Ramelow, A. Farsi, S. Clemmen, J. S. Levy, A. R. Johnson, Y. Okawachi, M. R. E. Lamont, M. Lipson, and A. L. Gaeta, "Strong polarization mode coupling in microresonators," Opt. Lett. **39**, 5134–5137 (2014).

[8] M. Ablowitz and P. Clarkson, *Solitons, nonlinear evolution equations and inverse scattering* (Cambridge, 1991).

[9] M. Ablowitz, *Nonlinear dispersive waves* (Cambridge, 2011).

[10] P. F. Byrd and M. D. Friedman, *Handbook of Elliptic Integrals for Engineers and Scientists* (Springer-Verlag, 1971).

[11] A. B. Matsko, A. A. Savchenko, W. Liang, V. S. Ilchenko, D. Seidel, and L. Maleki, "Mode-locked Kerr frequency combs," Opt. Lett. **36**, 2845–2847 (2011).

[12] Y. K. Chembo and C. R. Menyuk, "Spatiotemporal Lugiato-Lefever formalism for Kerr-comb generation in whispering-gallery-mode resonators," Phys. Rev. A **87**, 053852 (2013).

[13] Z. Qi, G. D'Aguanno, and C. R. Menyuk, "Nonlinear frequency combs generated by cnoidal waves in microring resonators," J. Opt. Soc. Am. B **34**, 785–794 (2017).

[14] P.-H. Wang, J. A. Jaramillo-Villegas, Y. Xuan, X. Xue, C. Bao, D. E. Leaird, M. Qi, and A. M. Weiner, "Intracavity Characterization of Micro-Comb Generation in the Single-Soliton Regime," Opt. Express **24**, 10890–10897 (2016).

[15] Y. Okawachi, K. Saha, J. S. Levy, Y. H. Wen, M. Lipson, and A. L. Gaeta, "Octave-spanning frequency comb generation in a silicon nitride chip," Opt. Lett. **36**, 3398–3400 (2011).

[16] A. Coillet, I. Balakireva, R. Henriet, K. Saleh, L. Larger, J. M. Dudley, C. R. Menyuk, and Y. K. Chembo, "Azimuthal Turing patterns, bright and dark solitons in Kerr combs generated with whispering-gallery-mode resonators," IEEE Phot. J. **5**, 6100409 (2013).

[17] D. C. Cole, E. S. Lamb, P. Del'Haye, S. A. Diddams, and S. B. Papp, "Soliton crystals in Kerr resonators," Nat. Phot. **11**, 671–676 (2017).

[18] C. Godey, I. V. Balakireva, A. Coillet, and Y. K. Chembo, "Stability analysis of the spatiotemporal Lugiato-Lefever model for Kerr optical frequency combs in the anomalous and normal dispersion regimes," Phys. Rev. A **89**, 063814 (2014).

[19] J. A. Jaramillo-Villegas, X. Xue, P. -H. Wang, D. E. Leaird, and A. M. Weiner, "Deterministic single soliton generation and compression in microring resonators avoiding the chaotic region," Opt. Express **23**, 9618–9626 (2015).

[20] P. Parra-Rivas, D. Gomila, M. A. Matías, S. Coen, and L. Gelens, "Dynamics of localized and patterned structures in the Lugiato-Lefever equation determine the stability and shape of optical frequency combs," Phys. Rev. A **89**, 043813 (2014).

[21] W. H. Renninger and P. T. Rakich, "Closed-form solutions and scaling laws for Kerr frequency combs," Sci. Rep. **6**, 24742 (2016).

[22] G. DAguanno and C. R. Menyuk, "Nonlinear mode coupling in whispering-gallery-mode resonators," Phys. Rev. A **93**, 043820 (2016).

[23] I. V. Barashenkov and Y. S. Smirnov, "Existence and stability chart for the ac-driven, damped nonlinear Schrödinger solitons," Phys. Rev. E **54**, 5707–5725 (1996).

[24] J. A. Fleck, J. R. Morris, and M. D. Feit, "Time-dependent propagation of high energy laser beams through the atmosphere," Appl. Phys. **10**, 129–160 (1976).

[25] N. Akhmediev, A. Ankiewicz, J. Soto-Crespo, and J. M. Dudley, "Universal triangular spectra in parametrically-driven systems," Phys. Lett. A **375**, 775–779 (2011).

[26] C. -H. Li, A. J. Benedick, P. Fendel, A. G. Glenday, F. X. Kärtner, D. F. Phillips, D. Sasselov, A. Szentgyorgyi, and R. L. Walsworth, "A laser frequency comb that

enables radial velocity measurements with a precision of 1 cm s^{-1}," Nature **452**, 610–612 (2008).

[27] K. J. Vahala, "Optical microcavities," Nature **424**, 839–846 (2003).

[28] J. Roslund, R. M. de Araújo, S. Jiang, C. Fabre, and N. Treps, "Wavelength-multiplexed quantum networks with ultrafast frequency combs," Nat. Photon. **8**, 109–112 (2014).

[29] D. J. Korteweg and G. de Vries, "On the change of form of long waves in a rectangular canal, and on a new type of long stationary waves," Phil. Mag. **5**, 422–4343 (1895).

[30] G. B. Whitham, *Linear and Nonlinear Waves* (Wiley, 1974).

[31] H. Schamel, "Analytical BGK modes and their modulational instability," J. Plasma Phys. **13**, 139–145 (1975).

[32] A. E. Walstead, *A Study of Nonlinear Waves Described by the Cubic Nonlinear Schrödinger Equation* (PhD Thesis), Report UCRL-52920 (March 12, 1980).

[33] A. R. Osbourne, *Nonlinear Ocean Waves and the Inverse Scattering Transform* (Academic, 2010).

[34] T. Kaladze and S. Mahmood, "Ion-acoustic cnoidal waves in plasmas with warm ions and kappa distributed electrons and positrons," Phys. Plasmas **21**, 032306 (2014).

[35] G. P. Agrawal, *Nonlinear Fiber Optics* (Academic, 2001).

[36] S. T. Cundiff, "Soliton dynamics in mode-locked lasers," in *Dissipative Solitons*, N. Akhmediev and A. Ankiewicz, eds. (Springer, 2005).

[37] L. M. Milne-Thomson, "Jacobian elliptic functions and theta functions," in *Handbook of Mathematical Functions*, M. Abramowitz and I. A. Stegun, eds. (National Bureau of Standards, 1972).

[38] N. Akhmediev and A. Ankiewicz, "Dissipative solitons in the complex Ginzburg-Landau and Swift-Hohenberg equations," in *Dissipative Solitons*, N. Akhmediev and A. Ankiewicz, eds. (Springer, 2005).

[39] V. Aleshkevich, Y. Kartashov, and V. Vysloukh, "Cnoidal wave compression by means of multisoliton effect," Opt. Comm. **185**, 305–314 (2000).

[40] Y. V. Kartashov, V. A. Vysloukh, and L. Torner, "Cnoidal wave patterns in quadratic nonlinear media," Phys. Rev. E **67**, 066612 (2003).

[41] D. J. Kedziora, A. Ankiewicz, and N. Akhmediev, "Rogue waves and solitons on a cnoidal background," Eur. Phys. J. Special Topics **223**, 43–62 (2014).

[42] J. P. Gordon, "Interaction forces among optical solitons," Opt. Lett. **8**, 596–598 (1983).

[43] F. Leo, S. Coen, P. Kockaert, S.-P. Gorza, P. Emplit, and M. Haelterman, "Temporal cavity solitons in one-dimensional Kerr media as bits in an all-optical buffer," Nat. Phot. **4**, 471–476 (2010).

[44] M. Pang, X. Jiang, W. He, G. K. L. Wong, G. Onishchukov, N. Y. Joly, G. Ahmed, C. R. Menyuk, and P. St.J. Russell, "Stable subpicosecond soliton fiber laser passively mode-locked by gigahertz acoustic resonance in photonic crystal fiber core," Optica **2**, 339–342 (2015).

[45] M. R. E. Lamont, Y. Okawachi, and A. L. Gaeta, "Route to stabilized ultrabroadband microresonator-based frequency combs," Opt. Lett. **38**, 3478–3481 (2013).

[46] X. Yi, Q.-F. Yang, K. Y. Yang, M.-G. Suh, and K. Vahala, "Soliton frequency comb at microwave rates in a high-Q silica microresonator," Optica **2**, 1078–1085 (2015).

[47] J. Pfeifle, A. Coillet, R. Henriet, K. Saleh, P. Schindler, C. Weimann, W. Freude, I. V. Balakireva, L. Larger, C. Koos, and Y. Chembo, "Optimally coherent Kerr combs generated with crystalline whispering gallery mode resonators for ultrahigh capacity fiber communications," Phys. Rev. Lett. **114**, 093902 (2015).

[48] C. Joshi, A. Klenner, Y. Okawachi, M. Yu, K. Luke, X. Ji, M. Lipson, and A. L. Gaeta, "Counter-rotating cavity solitons in a silicon nitride microresonator," Opt. Lett. **43**, 547–550 (2018).

[49] V. Brasch, M. Geiselmann, T. Herr, G. Lihachev, M. H. P. Pfeiffer, M. L. Gorodetsky, and T. J. Kippenberg, "Photonic chip-based optical frequency comb using soliton Cherenkov radiation," Science **351**, 357–360 (2016).

[50] Q. Li, T. C. Briles, D. A. Westly, T. E. Drake, J. R. Stone, B. R. Ilic, S. A. Diddams, S. B. Papp, and K. Srinivasan, "Stably accessing octave-spanning microresonator frequency combs in the soliton regime," Optica **4**, 193–203 (2017).

[51] V. Brasch, E. Lucas, J. D. Jost, M. Geiselmann, and T. J. Kippenberg, "Self-referenced photonic chip soliton Kerr frequency comb," Light: Sci. Appl. **6**, e16202 (2017).

[52] D. T. Spencer, T. Drake, T. C. Briles, J. Stone, L. C. Sinclair, C. Frederick, Q. Li, D. Westly, B. R. Ilic, A. Bluestone, N. Volet, T. Komljenovic, L. Chang, S. H. Lee, D. Y. Oh, M.-G. Suh, K. Y. Yang, M. H. P. Pfeiffer, T. J. Kippenberg, E. Norberg, L. Theogarajan, K. Vahala, N. R. Newbury, K. Srinivasan, J. E. Bowers, S. A. Diddams, and S. Papp, "An optical-frequency synthesizer using integrated photonics," Nature **557**, 81–85 (2018).

[53] C. Joshi, J. K. Jang, L. Luke, X. Ji, S. A. Miller, A. Klenner, Y. Okawachi, M. Lipson, and A. L. Gaeta, "Thermally controlled comb generation and soliton modelocking in microresonators," Opt. Lett. **41**, 2565–2568 (2016).

[54] X. Yi, Q.-F. Yang, K. Y. Yang, and K. Vahala, "Active capture and stabilization of temporal solitons in microresonators," Opt. Lett. **41**, 2037–2040 (2016).

[55] H. Guo, M. Karpov, E. Lucas, A. Kordts, M. H. P. Pfeiffer, V. Brasch, G. Lihachev, V. E. Lobanov, M. L. Gorodetsky, and T. J. Kippenberg, "Universal dynamics and deterministic switching of dissipative Kerr solitons in optical microresonators," Nat. Phys. **13**, 94–102 (2017).

[56] C. Bao, Y. Xuan, S. Wabnitz, M. Qi, and A. M. Weiner, "Spatial mode-interaction induced single soliton generation in microresonators," Optica **4**, 1011–1015 (2017).

[57] Z. Kang, F. Li, J. Yuan, K. Nakkeeran, J. N. Kutz, Q. Wu, C. Yu, and P. K. A. Wai, "Deterministic generation of single soliton Kerr frequency comb in microresonators by a single shot pulsed trigger," Opt. Express **26**, 18563–18577 (2018).

[58] H. Taheri, A. A. Eftekhar, K. Wiesenfeld, and A. Adibi, "Soliton formation in whispering-gallery-mode resonators via input phase modulation." IEEE Photon. J. **7**, 2200309 (2015).

[59] R. J. Weiblen and I. Vurgaftman, "Bichromatic pumping in mid-infrared microresonator frequency combs with higher-order dispersion," Opt. Express **27**, 4238–4260 (2019).

[60] D. C. Cole, J. R. Stone, M. Erkintalo, K. Y. Yang, X. Yi, K. J. Vahala, and S. B. Papp, "Kerr-microresonator solitons from a chirped background," Optica **5**, 1304–1310 (2018).

[61] S. Zhang, . M. Silver, L. Del Bino, F. Copie, M. T. M. Woodley, G. N. Ghalanos, A. Ø. Svela, N. Moroney, and P. DelHaye, "Sub-milliwatt-level microresonator solitons with extended access range using an auxiliary laser," Optica **6**, 206–212 (2019).

[62] X. Xue, Y. Xuan, P.-H. Wang, Y. Liu, D. E. Leaird, M. Qi, and A. M. Weiner, "Normal-dispersion microcombs enabled by controllable mode interactions," Laser Photonics Rev. **9**, L23–L28 (2015).

[63] S. Wang, A. Docherty, B. S. Marks, and C. R. Menyuk, "Boundary tracking algorithms for determining stability of mode-locked pulses," J. Opt. Soc. Am. B **31**, 2914–2930 (2014).

[64] J. C. Maxwell, *On the Stability of the Motion of Saturn's Rings* (MacMillan, 1859).

[65] H. A. Haus, "Parameter ranges for CW passive modelocking," IEEE J. Quantum Electron. **QE-12**, 169–176 (1976); H. A. Haus, "Mode-locking of lasers," IEEE J. Sel. Topics Quantum Electron. **6**, 1173–1185 (2000).

[66] J. N. Kutz, "Mode-locked soliton lasers," SIAM Rev. **48**, 626–678 (2006).

[67] A. B. Matsko and L. Maleki, "On timing jitter of mode locked Kerr frequency combs," Opt. Exp. **21**, 28862–28876 (2013).

[68] I. V. Barashenkov, Yu. S. Smirnov, and N. V. Alexeeva, "Bifurcation to multisoliton complexes in the ac-driven, damped nonlinear Schrödinger equation," Phys. Rev. E **57**, 2350–2364 (1998).

[69] M. Haelterman, S. Trillo, and S. Wabnitz, "Dissipative modulation instability in a nonlinear dispersive ring cavity," Opt. Comm. **91**, 401–407 (1992).

[70] L. A. Lugiato and R. Lefever, "Spatial dissipative structures in passive optical systems," Phys. Rev. Lett. **58**, 2209–2211 (1987).

[71] A. M. Turing, "The chemical basis of morphogenesis," Phil. Trans. Roy. Soc. Ser. B **237**, 37–72 (1952).

[72] Z. Qi, S. Wang, J. Jaramillo-Villegas, M. Qi, A. M. Weiner, G. D'Aguanno, T. F. Carruthers, and C. R. Menyuk, "Dissipative cnoidal waves (Turing rolls) and the soliton limit in microring resonators," Optica **6**, 1220–1232 (2019).

[73] J. Nocedal and S. Wright, *Numerical Optimization* (Springer, 2006).

[74] S. H. Strogatz, *Nonlinear Dynamics and Chaos: With Applications to Biology, Chemistry, and Engineering* (Westview, 1994).

[75] M. W. Hirsch, S. Smale, and R. L. Devaney, *Dynamical Systems and an Introduction to Chaos* (Academic, 2013).

[76] I. Stakgold, *Boundary Value Problems of Mathematical Physics, Volume 1* (MacMillan, 1967). See Chap. 2.

[77] G. Helmberg, *Introduction to Spectral Theory in Hilbert Space* (Dover, 1997).

[78] N. N. Akhmediev, A. Ankiewicz, and J. M. Soto-Crespo, "Multisoliton Solutions of the Complex Ginzburg-Landau Equation," Phys. Rev. Lett. **79**, 4047–4051 (1997).

[79] A. B. Matsko, A. A. Savchenkov, N. Yu, and L. Maleki, "Whispering-gallery-mode resonators as frequency references. I. Fundamental limitations," J. Opt. Soc. Am. B **24**, 1324–1335 (2007).

[80] W. Liang, D. Eliyahu, V. S. Ilchenko, A. B. Matsko, D. Seidel, and L. Maleki, "High spectral purity Kerr frequency comb radio frequency photonic oscillator," Nat. Comm. **6**, 7957 (2015).

[81] Z. Qi, S. Wang, J. A. Jaramillo-Villegas, M. Qi, A. M. Weiner, G. DAguanno, and C. R. Menyuk, "Stability of cnoidal wave frequency combs in microresonators," in Conference on Lasers and Electro-Optics, (Optical Society of America, 2018), paper SF2A.6.

[82] D. J. Kaup, "Perturbation theory for solitons in optical fibers," Phys. Rev. A **42**, 5689–5694 (1990).

[83] C. Bao, Y. Xuan, J. A. Jaramillo-Villegas, D. E. Leaird, M. Qi, and A. M. Weiner, "Direct soliton generation in microresonators," Opt. Lett. **42**, 2519–2522 (2017).

[84] J. A. Jaramillo-Villegas, C. Wang, P.-H. Wang, C. Bao, Y. Xuan, K. Han, D. E. Leaird, M. Qi, and A. M. Weiner, "Experimental characterization of pump power and detuning in microresonator frequency combs," Latin American Opt. Photon. Conf. (2016), paper LTh3B.2.

[85] G. Moille X. Lu, A. Rao, Q. Li, D. A. Westly, L. Ranzani, S. B. Papp, M. Soltani, and K. Srinivasan, "Kerr-Microresonator Soliton Frequency Combs at Cryogenic Temperatures," Phys. Rev. App. **12**, 034057 (2019).

[86] S. Cundiff, J. Ye, and J. Hall, "Rulers of light," Sci. Am. **298**, 74–81 (April, 2008).

[87] S. A. Diddams, "The evolving optical frequency comb," J. Opt. Soc. Am. B **27**, B51–B62 (2010).

[88] S. A. Diddams, K. Vahala, and T. Udem, "Optical frequency combs: coherently uniting the electromagnetic spectrum," Science **369**, eaay3676 (2020).

[89] T. J. Kippenberg, R. Holzwarth, and S. A. Diddams, "Microresonator-Based Optical Frequency Combs," Science **332**, 555–559 (2011).

[90] A. L. Gaeta, M. Lipson, and T. J. Kippenberg, "Photonic-chip-based frequency combs," Nat. Photon. **13**, 158–169 (2019).

[91] T. Kippenberg, S. Spillane, and K. Vahala, "Kerr-Nonlinearity Optical Parametric Oscillation in an Ultrahigh-Q Toroid Microcavity," Phys. Rev. Lett. **93**, 083904 (2004).

[92] A. Savchenkov, A. Matsko, D. Strekalov, M. Mohageg, V. Ilchenko, and L. Maleki, "Low Threshold Optical Oscillations in a Whispering Gallery Mode CaF_2 Resonator," Phys. Rev. Lett. **93**, 243905 (2004).

[93] Y. K. Chembo, and N. Yu, "Modal expansion approach to optical-frequency-comb generation with monolithic whispering-gallery-mode resonators," Phys. Rev. A **82**, 033801 (2010).

[94] Y. K. Chembo, D. V. Strekalov and N. Yu, "Spectrum and Dynamics of Optical Frequency Combs Generated with Monolithic Whispering Gallery Mode Resonators," Phys. Rev. Lett. **104**, 103902 (2010).

[95] W. Weng, E. Lucas, G. Lihachev, V. E. Lobanov, H. Guo, M. L. Gorodetsky, and T. J. Kippenberg, "Spectral purification of microwave signals with disciplined dissipative Kerr solitons," Phys. Rev. Lett. **122**, 013902 (2019).

[96] E. Lucas, P. Brochard, R. Bouchand, S. Schilt, T. Sudmeyer, and T. J. Kippenberg, "Ultralow-noise photonic microwave synthesis using a soliton microcomb-based transfer oscillator," Nat. Comm. **11**, 374 (2020).

[97] M.-G. Suh, Q.-F. Yang, K. Y. Yang, X. Yi, and K. J. Vahala, "Microresonator soliton dual-comb spectroscopy," Science **354**, 600–603 (2016).

[98] M.-G. Suh and K. J. Vahala, "Soliton microcomb range measurement," Science **359**, 884–887 (2018).

[99] P. Trocha, M. Karpov, D. Ganin, M. H. P. Pfeiffer, A. Kordts, S. Wolf, J. Krockenberger, P. Marin-Palomo, C. Weimann, S. Randel, W. Freude, T. J. Kippenberg, and C. Koos, "Ultrafast optical ranging using microresonator soliton frequency combs," Science **359**, 887–891 (2018).

[100] D. V. Strekalov and N. Yu, "Generation of optical combs in a whispering gallery mode resonator from a bichromatic pump," Phys. Rev. A **79**, 041805(R) (2009).

[101] T. Hansson and S. Wabnitz, "Bichromatically pumped microresonator frequency combs," Phys. Rev. A **90**, 013811 (2014).

[102] G. DAguanno and C. R. Menyuk, "Coupled Lugiato-Lefever equation for nonlinear frequency comb generation at an avoided crossing of a microresonator," Eur. Phys. J. D **71**, 74 (2017).

[103] C. Bao, P. Liao, A. Kordts, L. Zhang, M. Karpov, M. H. P. Pfeiffer, Y. Cao, Y. Yan, A. Almaiman, G. Xie, A. Mohajerin-Ariaei, L. Li, M. Ziyadi, S. R. Wilkinson, M. Tur, T. J. Kippenberg, and A. E. Willner, "Dual-pump generation of high-coherence primary Kerr combs with multiple sub-lines," Opt. Lett. **42**, 595–598 (2017).

[104] E. Obrzud, S Lecomte, and T. Herr, "Temporal solitons in microresonators driven by optical pulses," Nat. Photon. **11**, 600–607 (2017).

[105] S. A. Miller, Y. Okawachi, S. Ramelow, K. Luke, A. Dutt, A. Farsi, A. L. Gaeta, and M. Lipson, "Tunable frequency combs based on dual microring resonators," Opt. Express **23**, 21527–21540 (2015).

[106] B. Y. Kim, Y. Okawachi, J. K. Jang, M. Yu, X. Ji, Y. Zhao, C. Joshi, M. Lipson, and A. L. Gaeta, "Turn-key, high-efficiency Kerr comb source," Opt. Lett. **44**, 4475–4478 (2019).

[107] W. Wang, Z. Lu, W. Zhang, S. T. Chu, B. E. Little, L. Wang, X. Xie, M. Liu, Q. Yang, L. Wang, J. Zhao, G. Wang, Q. Sun, Y. Liu, Y. Wang, and W. Zhao, "Robust soliton crystals in a thermally controlled microresonator," Opt. Lett. **43**, 2002–2005 (2018).

[108] Z. Lu, W. Wang, W. Zhang, M. Liu, L. Wang, S. T. Chu, B. E. Little, J. Zhao, X. Wang, and W. Zhao, "Raman self-frequency-shift of soliton crystal in a high index doped silica micro-ring resonator," Opt. Mater. Express **8**, 2662–2669 (2018).

[109] Y. He, Q.-F. Yang, J. Ling, R. Luo, H. Liang, M. Li, B. Shen, H. Wang, K. Vahala, and Q. Lin, "Self-starting bi-chromatic $LiNbO_3$ soliton microcomb," Optica **6**, 1138–1144 (2019).

[110] A. Coillet, Z. Qi, I. V. Balakireva, G. Lin, C. R. Menyuk, and Y. Chembo, "On the transition to secondary Kerr combs in whispering-gallery mode resonators," Opt. Lett. **44**, 3078–3081 (2019).

[111] M. Karpov, M. H. P. Pfeiffer, H. Guo, W. Weng, J. Liu, and T. J. Kippenberg, "Dynamics of soliton crystals in optical microresonators," Nat. Phys. **15**, 1071–1077 (2019).

[112] Y. He, J. Ling, M. Li, and Q. Lin, "Perfect soliton crystals on demand," Laser Photonics Rev. **14**, 201900339 (2020).

[113] Z. Wu, Y. Gao, J. Dai, T. Zhang and K. Xu, "Switching dynamics of dissipative cnoidal waves in dual-coupled microresonators," Opt. Express **29**, 42369–42383 (2021).

[114] Z. Qi, A. Leshem, J. A. Jaramillo-Villegas, G. D'Aguanno, T. F. Carruthers, O. Gat, A. M. Weiner and C. R. Menyuk, "Deterministic access of broadband frequency combs in microresonators using cnoidal waves in the soliton crystal limit," Opt. Express **28**, 36304 (2020).

[115] S. Diallo, G. Lin, and Y. K. Chembo, "Giant thermo-optical relaxation oscillations in millimeter-size whispering gallery mode disk resonators," Opt. Lett. **40**, 3834–3837 (2015).

[116] A. Leshem, Z. Qi, T. F. Carruthers, C. R. Menyuk, and O. Gat, "Thermal instabilities, frequency comb formation, and temporal oscillations in Kerr microresonators," Phys. Rev. A **103**, 013512 (2021).

[117] R. P. Feynman, R. B. Leighton, and M. Sands, *The Feynman Lectures on Physics* (Addison-Wesley, 1965), Vol. III, Chap. 12.

[118] T. Herr, V. Brasch, J. D. Jost, I. Mirgorodskiy, G. Lihachev, M. L. Gorodetsky, and T. J. Kippenberg, "Mode spectrum and temporal soliton formation in optical microresonators," Phys. Rev. Lett. **113**, 123901 (2014).

[119] Y. Hu, J. Ling, M. Li, and Q. Liu, "Perfect soliton crystals on demand," Laser Phot. Rev. **14**, 1900339 (2020).

[120] M. Tan, X. Xu, J. Wu, R. Morandotti, A. Mitchell, and D. J. Moss, "RF and microwave photonic optical signal processing with Kerr micro-combs," Adv. Phys.: X **6**, 1838946 (2021).